Colloidal CdSe/CdS Nanostructures: Synthesis, Optical Characterization and Applications

by

Igor Coropceanu

B.S. Chemistry, 2011
Georgia Institute of Technology

Submitted to the Department of Chemistry
in Partial Fulfillment of the Requirements for the Degree of

DOCTOR OF PHILOSOPHY IN PHYSICAL CHEMISTRY
at the
MASSACHUSETTS INSTITUTE OF TECHNOLOGY
September 2016

Author..... Signature redacted .....
Department of Chemistry
July 5, 2016

Certified by..... Signature redacted .....
Moungi G. Bawendi
Lester Wolfe Professor of Chemistry
Thesis Supervisor

Accepted by..... Signature redacted .....
Robert W. Field
Chairman, Departmental Committee on Graduate Students

This doctoral thesis has been examined by a Committee of the Department of Chemistry as follows:

Signature redacted

Professor Troy Van Voorhis .. ..
Haslam and Dewey Professor of Chemistry
Chairperson

Professor Moungi G. Bawendi..... Signature redacted
Lester Wolfe Professor of Chemistry
Thesis Supervisor

Signature redacted

Professor Timothy M. Swager ....
John D. MacArthur Professor
Thesis Committee Member

Colloidal CdSe/CdS Nanostructures: Synthesis, Optical Characterization and Applications

by

Igor Coropceanu

Submitted to the Department of Chemistry
in Partial Fulfillment of the Requirements for the Degree of
Doctor of Philosophy in Physical Chemistry

Abstract

The focus of this thesis is the study of CdSe/CdS nanostructures, from their fundamental properties to their integration in practical devices. This material system has proven to be remarkably robust both as a platform for studying physics in confined semiconductors, as well as for enabling various optical and optoelectronic applications. In this thesis, we will discuss our recent efforts to improve the synthesis of CdSe/CdS structures, to better understand their optical properties and to use them to create highly performing luminescent solar concentrators.

In the first part of the thesis we will discuss our efforts to improve the synthesis of CdSe/CdS nanostructures of different dimensionalities. In particular, we discuss the synthesis of CdSe/CdS quantum dots and seeded CdSe/CdS nanorods that have a near unity photoluminescence quantum yield and complete energy transfer from the shell to the core. Next, we discuss the fabrication of luminescent solar concentrators using these materials and the optical characterization of these devices. Finally, in the last section, we use a combination of synthesis, spectroscopy, and modeling to gain better insight into the photoluminescence lineshape of CdSe/CdS quantum dots.

Thesis Supervisor: Moungi G. Bawendi
Title: Lester Wolfe Professor of Chemistry

Acknowledgements

This thesis and all the work it represents would never have been possible if it weren't for the many people in my life who have guided me and helped me along the way. I am indebted to far too many people to do this section justice, but here is a start.

I feel extremely lucky to have had the honor and pleasure of working with Moungi Bawendi as my advisor. There are few people I have ever met who could combine such an incredibly broad base of high level knowledge with a keen critical eye towards even the smallest details. Moreover, I greatly appreciate the careful and collaborative group culture Moungi helped foster. It is hard to imagine a better atmosphere where I could learn how to do interesting and meaningful science and how to become an independent researcher.

As far as my research is concerned, I owe a debt of gratitude to the many colleagues and collaborators that I have worked with along the years. It is hard to overstate how much more I have accomplished and learned thanks to others. In particular, I have to thank Aurelio Rossinelli, Hendrik Utzat, Andrew Beyler, Thomas Bischof, Greg Gutierrez, Jian Cui, Russ Jensen, Jennifer Scherer, Justin Caram and Giovanni Azzellino.

I am also very happy to have had the chance to be part of the spectroscopy subgroup for the past five years. Much of what I have learned at MIT has been through the many, many discussions we have had, including with Thomas, Andrew, Jian, Russ, Mark, Hendrik, Sophie, Katie, Justin, Lea, and others. Finally, I would like to thank all the other members of Bawendi Lab with whom I crossed paths over the past few years. I had a great time talking to all of you and hearing about your fascinating work spanning topics as varied as chemistry, physics and biology.

I could not have made it through the ups and downs of grad school if it weren't for the wonderful colleagues and friends that I had the joy of meeting at

MIT. For all the great memories, both at work and outside of lab, thank you: Chia-Hao, Whitney, Andrew, Jessica, Mike, Kurt, Wankyu, Jenny, Thomas, Matt, Paul, Steph, Jess, and many others. I wish you all the best and hope to see you again in the future.

Looking further back, I am very grateful for the many wonderful people at Georgia Tech who have helped me start my career as a chemist. I feel very fortunate to have had the chance of working in the lab of Seth Marder, where I got my first taste of what chemistry and real research were like. I greatly appreciate the mentorship I received along the way from Seth and the people I have worked with, especially Carlos Zuniga, Susan Odom, and Ali Hayek.

Finally, I would be more than remiss if I failed to acknowledge the great debt I owe my parents. Their support, encouragement, and guidance are what made me the person I am today, both personally and professionally. Once again, thank you very much to you all!

Table of Contents

Table of Figures

CHAPTER 1
Introduction

1.1 Introduction to Quantum Confined Semiconductor Nanocrystals

Quantum confined nanocrystals are a class of semiconducting structures which are defined by the property that their physical shape and size strongly modulate their electronic structure. Typically, at least one or more dimensions of these structures lie on the scale of 1-100nm as implied by their name. The broader family of nanocrystals includes spherical (quasi 0-dimensional) structures called quantum dots, elongated (quasi 1-deminsional) structures called nanorods or nanowires and pancake-like (quasi 2-dimensional) structures called nanoplatelets. Due to their strong quantum confinement, nanocrystals offer a broad range of tools through which their electronic, optical, and chemical properties can be tuned. Through a judicious choice of the semiconducting material(s), the architecture of structure, as well as its size and shape, the spectral region in which the structure is optically active can be tuned from the near-ultraviolet (near-UV) to the mid infrared (MWIR). This high degree of flexibility, coupled with the possibility of narrow emission bands and near unity quantum yields have made quantum dots an appealing system for a variety of applications, ranging from optoelectronics to biological imaging.[1-4]

1.1.1 The Electronic Properties of Quantum Confined Semiconductor Nanocrystals

The general behavior of the electronic properties of quantum dots and related nanostructures is succinctly summarized by their definition as "spatially confined semiconductors". As this wording suggests, two key aspects dominate the electronic property of these structures: 1) their material composition and 2) their specific size and shape. The first of these factors is well understood within the framework of solid state semiconductor physics. Beginning with the discrete orbitals of atoms, one can then build up larger and larger structures, going from molecules, to small clusters, until one reaches the bulk limit, as summarized in Fig. 1-1. At the bulk level the electronic structure is best understood by transitioning from a discrete picture of energy levels, to a quasi-continuum picture of energy bands with an associated density of states. A key property of optically active semiconductors is the presence of energy separation between the highest occupied band (the valence band) and the lowest unoccupied band (the conduction band) called the bandgap.

This bulk picture can conveniently be taken as the starting point for evaluating the electronic structure of spatially confined semiconductors. A powerful theoretical tool to study the transition from the bulk limit to the confined case is the effective mass approximation (EMA).[5] The result of this mathematical treatment is to combine the periodic Bloch functions of the bulk crystal with an additional function called the envelope. The envelope captures the effect of the shape and size of the nanostructure in shaping the new set of wavefunctions describing the system. [5-7]

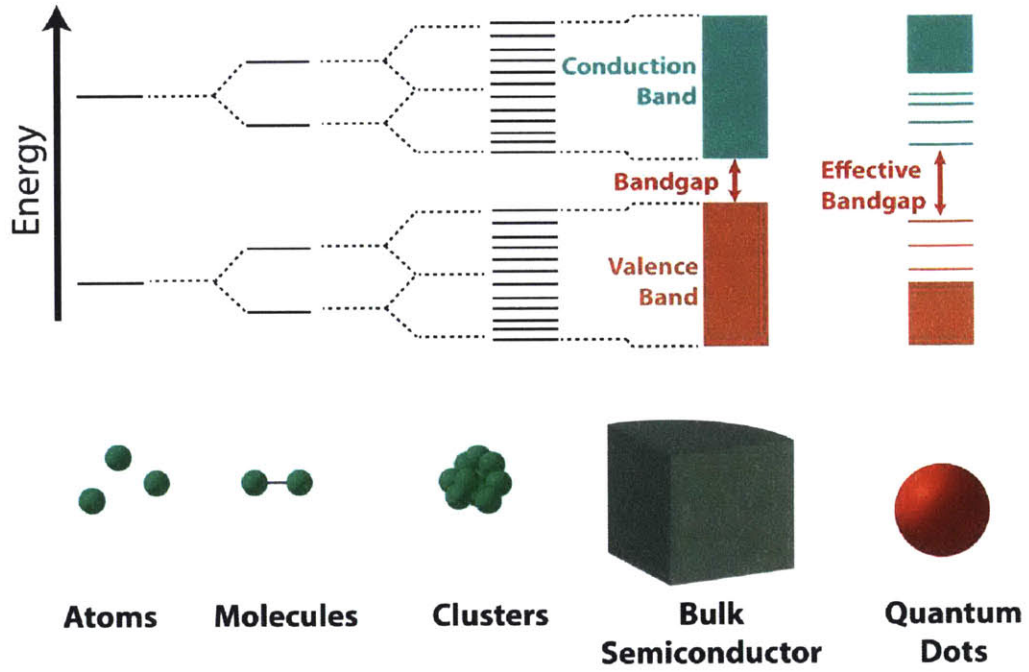

Figure 1-1: The evolution of the electronic properties of an optically active material from atoms to bulk semicondcutors and modulated by quantum confinement in nanostructures

The optical properties of quantum confined nanocrystals is most commonly mediated by bound electron-hole pairs, called excitons. In bulk crystals and within the effective mass approximation the exciton can be described as a hydrogen-like system where the electron is electrostatically bound to the hole. Similar to the case of the hydrogen atom, we can define a quantity called the Bohr radius of the exciton (R_B) as defined in equation 1-1 below

$$R_B = \varepsilon_r \left(\frac{m_e}{\mu^*}\right) a_0 \tag{1-1}$$

where ε_r is the dielectric constant of the semiconductor, m_e is the free electron mass, μ^* is the reduced effective mass of the exciton, and a_0 is the Bohr radius of a hydrogen atom.

The Bohr radius can be taken as a natural reference point to study the degree of quantum confinement in such a system (see Fig. 1-2). In bulk semiconductors and large micro-crystallites the size of the crystal (r_{QD}) is much larger than the excitonic Bohr radius (R_B). In these systems the Wannier basis provides a natural description of the electronic structure of excitons, with the physical confinement of the nanostructure acting at most as a perturbation. On the other hand, as the particle of nanocrystal decrease, its spatial confinement will add a repulsive energy term called the confinement energy ($E_{confinement}$), which for a spherical particle varies inversely with the square of its radius:

$$E_{confinement} = \frac{\hbar^2 \pi^2}{2\mu^* r^2} \tag{1-2}$$

For a semiconducting particle subjected to strong confinement of its charge carriers, it is often convenient to separate the energy of the exciton according the various contributing sources. Following the EMA formalism introduced above, the energy of the exciton can be expressed as the sum of three terms: 1) the bandgap of the bulk material, the confinement energy of the exciton as defined above, and finally the Coulomb attraction between the two charge carriers (Eq. 1.1).

$$E_{exciton} = E_{bandgap} + E_{confinement} + E_{coulomb} \tag{1-3}$$

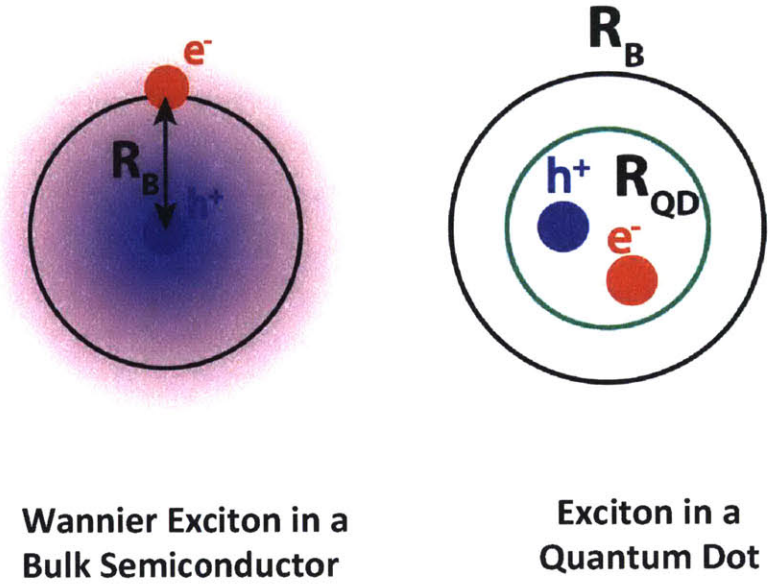

Figure 1-2: The difference between excitons in bulk semiconductors (Wannier Excitons) and Confined Excitons in Quantum Dots

1.2 Colloidal Nanocrystals

Nanocrystals of different dimensionalities can be grown using a variety of techniques, including gas-phase, liquid-phase, and solid-phase approaches. In this work, the focus will be on nanocrystals grown through self-assembly in solution. These growth conditions generally allow the particles to form stable colloidal suspensions in a compatible solvent, giving rise to the term "colloidal nanocrystal." Because of their growth conditions, colloidal nanocrystals consist of both an inorganic part and an organic exterior.

Figure 1-3 below shows the architecture of a typical colloidal nanostructure: a core/shell quantum dot. In this structure, an inorganic core is surrounded by an additional inorganic layer called the shell. The shell in turn is surrounded by a layer of organic ligands, which ensure the colloidal stability of the structure. In practice, the details of the inorganic part of the nanocrystal can vary drastically, including the possibility of a single inorganic layer, complicated multilayer structures, or graded alloyed structures. Likewise, the ligand shell can

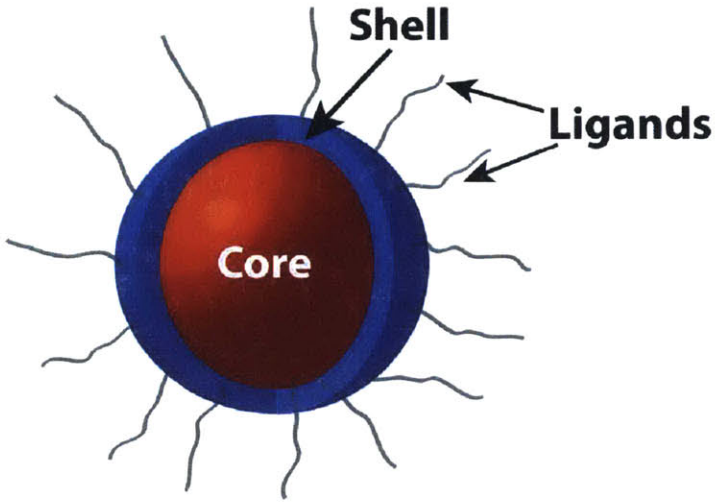

Figure 1-3: General Structure of a Colloidal Core/Shell Quantum Dot

range from simple short chain organic moieties (e.g. carboxylic acids, amines, thiols) to more complex scaffolds such as multifunctional block copolymers. It is important to emphasize that while a primary role of the ligand shell is to render the nanocrystal soluble in a solvent of choice, it can also play an important functional role, including by directly affecting the electronic properties of nanostructure as a whole.

1.3 The Synthesis of Colloidal Nanostructures

Since the first reports of the successful solution based synthesis of colloidal quantum dots, dramatic progress has been made in improving the synthetic quality and expanding the complexity of such structures.[8] The most widely used method to create monodisperse batches of quantum dots remains the hot-injection technique. In this method, the precursors of the quantum dot material are allowed to quickly react together in a well-defined nucleation step, followed by a secondary growth step. As a result of the tendency of small particles to grow more quickly than larger particles, it is possible for the growth step to occur in a regime called "size focusing," where the size distribution of the quantum dots can narrow.[9] As a result, for many classes of materials it is possible to reproducibly obtain batches of nanorods with very low polydispersity (often less than 5%).[2]

While early studies of quantum dots focused on single-material systems, the field was rapidly expanded by the development of multilayer structures.[10] The simplest example of such heterostructures are core/shell quantum dots, such as the one shown in Fig. 1-3 above. It soon became apparent that core/shell quantum dots could offer key advantages over core only dots, especially for luminescent applications. Key among these benefits were a high quantum yield, low emission intermittency (blinking), and improved photostability.[2, 11] Other possibilities included changing the shape of the particle by embedding the spherical core in a shell that was elongated as in seeded nanorods or which had an even more exotic structure as in tetrapods for example.[12, 13]

1.4 The Fluorescence Lineshape of Colloidal Quantum Dots

One of the most important properties that characterize a semiconducting nanocrystal is the structure of the fluorescence lineshape. Controlling the lineshape is crucial for enabling the use of such nanostructures as fluorophores in applications ranging from light emitting diodes to multiplexed imaging. Moreover, from a fundamental perspective the lineshape, including its breadth and structure, provides critical information on the electronic structure of the nanocrystal and the key physical processes that modulate its dynamics.

One of the most attractive features of quantum dots and related nanostructures is that they exhibit a narrow and tunable emission band. However, the word "narrow" merits a more careful look in this context. High quality nanostructures based on a spherical CdSe core generally have a PL lineshape with a full width at full max (FWHM) on the order of 60-80meV (~20nm at an emission maximum of 630nm).[2, 14, 15] From an application standpoint, this lineshape very often compares very favorably to alternative chromophores. For example, for light emitting applications, the narrow lineshape of CdSe based quantum dots is substantially narrower than the corresponding emission bands of typical organic phosphors used in the display industry. As a result, new displays incorporating quantum dots are capable of producing a higher color purity than that found in older generation LCD displays.[16]

Nevertheless, while the lineshape of quantum dots can be considered to be narrow for many practical applications, from a physical perspective it appears to be unexpectedly broad at first sight. As a starting point, we can calculate the "natural" lineshape of the quantum dots (δE_{nat}) if the only broadening mechanism was due to its finite radiative lifetime (τ_{rad}), which can be expressed as in Eq. 1-3 below:

$$\delta E_{nat} = \frac{h}{2\pi\tau_{rad}} \tag{1-4}$$

Taking into account the fact that the radiative lifetime of CdSe quantum dots is typically on the order of ~10 ns, we obtain a natural linewidth on the order of 100 neV.

Clearly this number is smaller by many orders of magnitude when compared to the lineshape observed at room temperature. The question then becomes what mechanism dominates the broadening. At the individual dot level, possibilities include 1) spectral dynamics induced by the fluctuating environment of the dots, 2) the presence of multiple emissive states, and finally, 3) the presence of exciton-phonon coupling.[14, 17, 18] These three factors together define the average single-particle lineshape. In addition to these mechanisms, the polydispersity of the quantum dot sample will also add a contribution to the lineshape measured at the ensemble level, which we will call the inhomogenous broadening. All the four mechanisms described above are shown pictorially in Fig. 1-4.

A key question is what mechanism dominates the broadening that results in the room temperature spectrum? The first part of the answer as it relates to CdSe/CdS quantum dots is that size inhomogeneity is not the answer. A variety of techniques ranging from single particle fluorescence to solution – photon correlation Fourier spectroscopy (s-PCFS) indicate that for high quality batches of CdSe/CdS dots the average single particle spectrum is alost identical to the ensemble spectrum.[2, 15] As a result, the broad ensemble lineshape simply reflects the fact that each individual quantum dot has a spectrum that is broad.

Next, we can consider the relative importance of the mechanisms that shape the lineshape of quantum dots at the single particle level. From previous

studies we know that the net effect of spectral diffusion is to induce broadening on the order of less than 1meV, particularly for thicker core/shell particles.[18] This fact is consistent with our observations that the room temperature spectrum of these particles is effectively constant when monitored on timescale accessible on a camera (10s of ms). Next we can turn to the effect of the exciton fine structure. In CdSe/CdS dots, the only states that have a non-zero oscillator strength and can be thermally populated (at room temperature) have an energy difference of 10-20meV.[14] While this fine structure can clearly have an important impact on the overall lineshape, it cannot by itself account for the 60-100meV linewdiths observed in practice.

The last key mechanism that remains to be explored is exciton-phonon coupling. In previous studies, coupling to phonons has been invoked as the key mecnaism dominating the broadening of the lineshape.[14, 19] While this conclusion is reasonable from the available data, the key limitation of the available studies is that they could only rely on indirect evidence to attribute the broadening to exciton-phonon coupling. In Ch. 4 we will discuss a more direct approach to quantifying this coupling by measuring the fluorescence spectra of CdSe/CdS quantum dots at the single particle level from cryogenic temperatures (4K) all the way to room temperature.

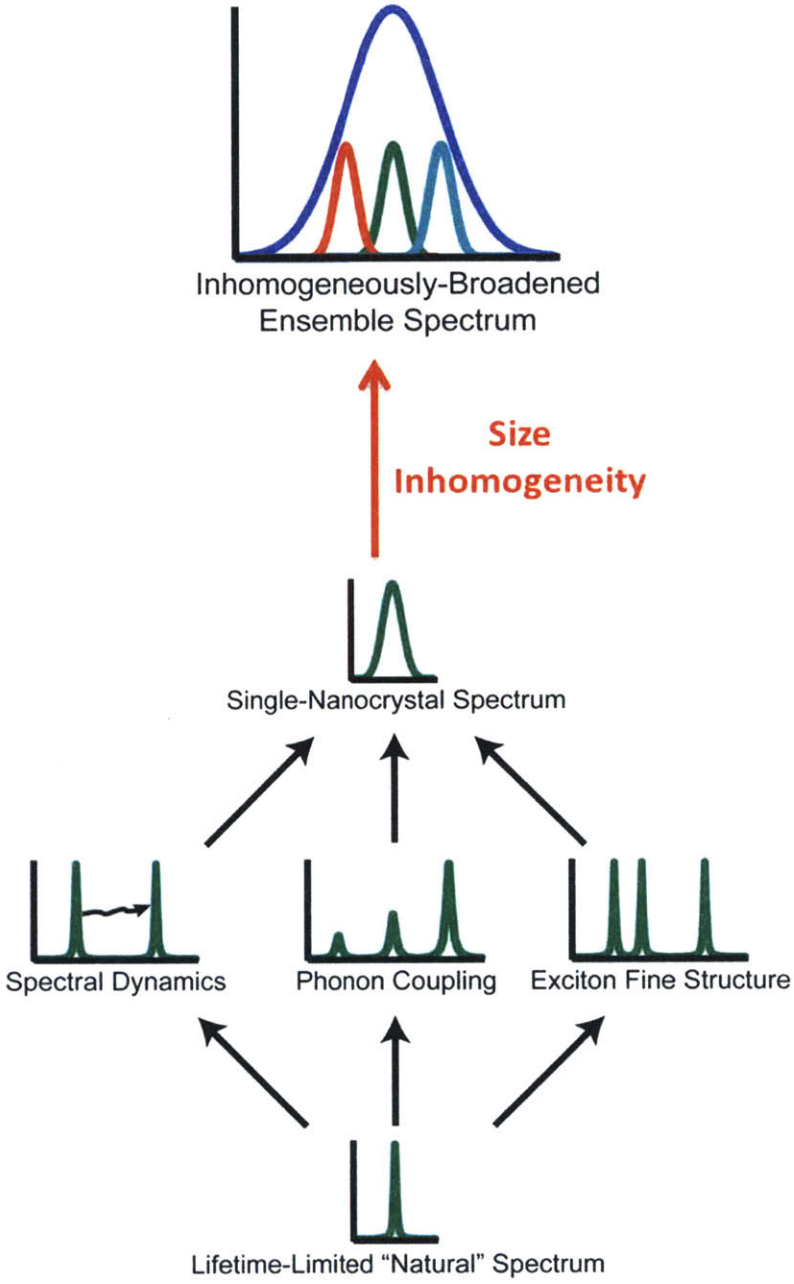

Figure 1-4: Lineshape broadening mechanisms in semiconductging nanocrystals (adapted with permission from Ref. 14)

1.5 Luminescent Solar Concentrators

1.5.1 Introduction

Luminescent solar concentrators (LSCs) have emerged in recent years as a promising avenue towards economically viable solar energy harvesting.[20-23] As in all other types of solar concentrators, the key operating principle of an LSC is the collection of light over a large surface area and its concentration to a target with a smaller surface area. In contrast to conventional (active) solar concentrators, which rely on direct focusing of the light (e.g. using parabolic mirrors or troughs), LSCs are a passive system that does not require active tracking of the Sun.[24] In an LSC concentration is achieved by relying on a chromophore embedded in a dielectric slab to first absorb the incoming solar radiation and then to re-emit the light. The slab then acts as a waveguide, which traps part of the emitted flux through refractive index contrast and guides it to the edges (see Fig 1-6). The ratio of the surface area of the face of the device to the surface area of the edges then defines the geometric concentration factor called the concentration gain, similar to a conventional concentrator. A solar cell can then be placed at the edges to carry out the final conversion of the light to electricity.

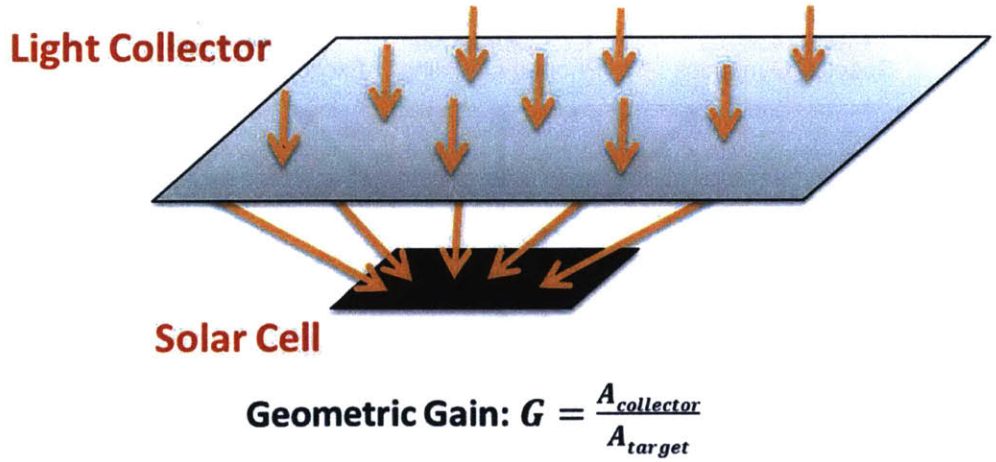

Figure 1-5: The general scheme of a solar concentrator

Their passive mode of operation allows LSCs to not only avoid expensive solar tracking controllers, but also offers the benefit of collecting both direct and diffuse sunlight. As a result, LSCs offer the possibility of creating a more cost-effective and efficient platform for solar energy harvesting, which can be coupled to existing PV systems. Nevertheless, for the practical implementation of such devices, further improvements are required, most notably in increasing the proportion of the incident photon flux successfully collected and guided to the edges. Their high photoluminescence quantum yield, strong and broad absorption, and versatile tunability have made nanocrystalline structures such as quantum dots and nanorods promising candidates to serve as the active material in LSCs. One advantage of nanorods is the possibility of creating core-shell structures, which allows a spectral separation of the absorption and emission, thus diminishing reabsorption. Furthermore, because of their anisotropic shape, nanorods can preferentially emit light in a plane perpendicular to their long axis[25], a property which can lead to a reduction in top escape losses if the nanorods are aligned perpendicular to the plane of the concentrator.[26]

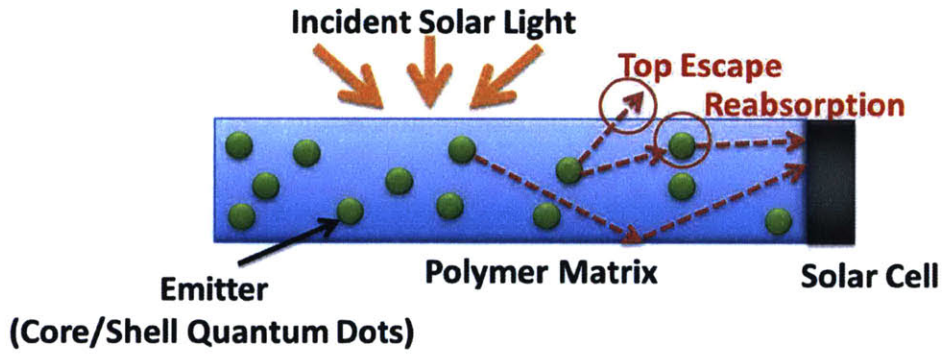

Figure 1-6: Basic optical processes in a luminescent solar concentrator and optical losses (shown in red)

1.5.2 General Considerations for the Active Material of a Luminescent Solar Concentrator

A key figure of merit describing the performance of luminescent solar concentrators is the optical efficiency η, defined as the ratio of the photon flux guided to the edges of the LSC divided by the incident flux. This quantity scales approximately as:

$$\eta(\lambda) \sim A(\eta_{Pl}\eta_{tr})^{n+1} \tag{1-5}$$

In the equation above, A is the fraction of photons absorbed, η_{Pl} and η_{tr} are the photoluminescence efficiency and trapping efficiency (the fraction of photons re-emitted in the LSC trapped via total internal reflection) respectively, and n is the number of reabsorption events.[27] A key consequence of the above relationship is that unless the two internal efficiencies reach unity, a situation extremely difficult to realize in practice, the optical efficiency will rapidly decrease with the number of reabsorption events. This latter issue is particularly problematic since for LSCs to have practical applications, a large geometric gain, G (the ratio of the area of the face of the LSC to the surface area of the edges), is needed.

The requirement for a large geometric gain arises from the dependence of the ability of an LSC to concentrate light on this parameter. Specifically, the amount of light concentrated can be quantified by F, the so-called flux gain, defined as the ratio of the photon flux guided to the edges divided by the solar energy flux that would be incident on the surface area of the edges, which can be expressed as $F = \eta \times G$. From this relationship, it is immediately clear that an LSC cannot significantly concentrate light unless it has a large geometric gain. However, as the geometric gain increases, so necessarily does the average optical path of the light through the device, thus increasing the probability for

reabsorption and diminishing the efficiency, such that at a certain value of G the flux gain will stop rising.

For the above-mentioned reasons, reducing the reabsorption has always been the key problem in LSC development and numerous solutions to this problem have been explored. Most of the strategies pursued to this end can generally be divided into two classes 1) changes in intrinsic material parameters to reduce the spectral overlap between the absorption and emission and 2) dilution of the emissive species.[24] The most notable approach belonging to the first category is the energetic separation of the positions of the absorption and emission maxima corresponding to the same electronic transition, e.g. due to vibronic coupling. For organic dyes this value is usually equal to the Stokes shift, the energy difference between the global absorption and emission maxima. However, in spite of extensive efforts to screen possible candidate materials exhibiting a sufficiently large Stokes shift for LSC applications, even the best materials display significant reabsorption relying on this factor alone.

A related strategy, called solid state solvation (SSS), is based on the preferential stabilization of the excited state in a polar solid matrix, resulting in a further reduction in reabsorbance. It was on a combination of a large Stokes shift organic dye and exploitation of SSS that a state-of-the-art LSC developed by Baldo and coworkers was based.[20] An additional approach in this category is reliance on emission via an electronic transition with a low absorption oscillator strength, such as emission from phosphorescent complexes or f-f transitions in rare earth complexes.[20, 28] However, while such materials have indeed been proven to yield greatly diminished reabsorption, their applicability to LSCs has generally been limited either by a low quantum yield or insufficient absorption across the solar spectrum.

The second category can be thought of as a host-guest system where most reabsorption takes place by the host and the energy is transferred to the guest, the latter finally re-emitting the light. The host-guest system can either consist of

a blend of separate components or a single material containing two separate subunits. In terms of the former, various systems composed of an organic host and a fluorescent or phosphorescent guest have been reported.[20, 29] One approach falling into the latter category is based on the use of core-shell inorganic nanorods. In such systems, emission occurs exclusively from the core, while the majority of the absorption takes place in the shell. The key to minimizing reabsorption in such systems then is essentially to minimize the volume ratio of the core to the shell. In Ch. 4 we will discuss the realization of this approach using CdSe/CdS quantum dots and nanorods to create an active material with minimal reabsorption and near unity fluorescence quantum yields.

1.6 Overview of the Thesis

The thesis focuses on the synthesis, characterization, and application of semiconducting nanocrystals. In particular, the material system studied consisted of core/shell structures of CdSe/CdS having either a spherical CdS shell (quantum dots) or an elongated shell (nanorods).

Chapter 2 discusses the development of new methods to synthesize CdSe/CdS core/shell quantum dots and nanorods. The characterization of the materials using a suite of optical tools ranging from spectrophotometry to single particle fluorescence is discussed. In particular, we emphasize the key factors needed obtain particles with a quantum yield approaching 100% and complete energy transfer from the shell to the core.

Chapter 3 deals with the study of the active materials used in luminescent solar concentrators. Inorganic heterostructures are shown to be ideally suited to reduce reabsorption due to their ability to act as a host/guest system where one part of the structure is responsible for the absorption and another part is responsible for the emission. The fabrication, optical characterization, and modeling of prototype devices fabricated using CdSe/CdS quantum dots is discussed in detail.

Chapter 4 discusses the optical and electronic properties of CdSe/CdS quantum dots. The role of electron delocalization into CdS is discussed as the central mechanism directing the evolution of the optical spectra as a function of the shell thickness. A unified model is presented to describe the fluorescence lineshape in these particles and its dependence on exciton-phonon coupling in the quantum dots.

Ch. 1 References

1. Mashford, B. S.; Stevenson, M.; Popovic, Z.; Hamilton, C.; Zhou, Z.; Breen, C.; Steckel, J.; Bulovic, V.; Bawendi, M.; Coe-Sullivan, S.; Kazlas, P. T. High-Efficiency Quantum-Dot Light-Emitting Devices with Enhanced Charge Injection. Nat Photon 2013, 7, 407-412.

2. Chen, O.; Zhao, J.; Chauhan, V. P.; Cui, J.; Wong, C.; Harris, D. K.; Wei, H.; Han, H. S.; Fukumura, D.; Jain, R. K.; Bawendi, M. G. Compact High-Quality Cdse-Cds Core-Shell Nanocrystals with Narrow Emission Linewidths and Suppressed Blinking. Nat. Mater. 2013, 12, 445-451.

3. Castelli, A.; Meinardi, F.; Pasini, M.; Galeotti, F.; Pinchetti, V.; Lorenzon, M.; Manna, L.; Moreels, I.; Giovanella, U.; Brovelli, S. High-Efficiency All-Solution-Processed Light-Emitting Diodes Based on Anisotropic Colloidal Heterostructures with Polar Polymer Injecting Layers. Nano Lett. 2015, 15, 5455-5464.

4. Han, H.-S.; Niemeyer, E.; Huang, Y.; Kamoun, W. S.; Martin, J. D.; Bhaumik, J.; Chen, Y.; Roberge, S.; Cui, J.; Martin, M. R.; Fukumura, D.; Jain, R. K.; Bawendi, M. G.; Duda, D. G. Quantum Dot/Antibody Conjugates for in Vivo Cytometric Imaging in Mice. Proceedings of the National Academy of Sciences 2015, 112, 1350-1355.

5. Efros, A. L.; Rosen, M. The Electronic Structure of Semiconductor Nanocrystals. Annual Review of Materials Science 2000, 30, 475-521.

6. Efros, A.; Rodina, A. Band-Edge Absorption and Luminescence of Nonspherical Nanometer-Size Crystals. Physical Review B 1993, 47, 10005-10007.

7. Efros, A. L.; Rosen, M.; Kuno, M.; Nirmal, M.; Norris, D. J.; Bawendi, M. Band-Edge Exciton in Quantum Dots of Semiconductors with a Degenerate

Valence Band: Dark and Bright Exciton States. Physical Review B 1996, 54, 4843-4856.

8. Murray, C. B.; Norris, D. J.; Bawendi, M. G. Synthesis and Characterization of Nearly Monodisperse Cde (E = Sulfur, Selenium, Tellurium) Semiconductor Nanocrystallites. J. Am. Chem. Soc. 1993, 115, 8706-8715.

9. Thanh, N. T. K.; Maclean, N.; Mahiddine, S. Mechanisms of Nucleation and Growth of Nanoparticles in Solution. Chem. Rev. (Washington, DC, U. S.) 2014, 114, 7610-7630.

10. Carbone, L.; Cozzoli, P. D. Colloidal Heterostructured Nanocrystals: Synthesis and Growth Mechanisms. Nano Today 2010, 5, 449-493.

11. Ghosh, Y.; Mangum, B. D.; Casson, J. L.; Williams, D. J.; Htoon, H.; Hollingsworth, J. A. New Insights into the Complexities of Shell Growth and the Strong Influence of Particle Volume in Nonblinking "Giant" Core/Shell Nanocrystal Quantum Dots. J. Am. Chem. Soc. 2012, 134, 9634-9643.

12. Carbone, L.; Nobile, C.; De Giorgi, M.; Sala, F. D.; Morello, G.; Pompa, P.; Hytch, M.; Snoeck, E.; Fiore, A.; Franchini, I. R.; Nadasan, M.; Silvestre, A. F.; Chiodo, L.; Kudera, S.; Cingolani, R.; Krahne, R.; Manna, L. Synthesis and Micrometer-Scale Assembly of Colloidal Cdse/Cds Nanorods Prepared by a Seeded Growth Approach. Nano Lett. 2007, 7, 2942-2950.

13. Talapin, D. V.; Nelson, J. H.; Shevchenko, E. V.; Aloni, S.; Sadtler, B.; Alivisatos, A. P. Seeded Growth of Highly Luminescent Cdse/Cds Nanoheterostructures with Rod and Tetrapod Morphologies. Nano Lett. 2007, 7, 2951-2959.

14. Cui, J.; Beyler, A. P.; Coropceanu, I.; Cleary, L.; Avila, T. R.; Chen, Y.; Cordero, J. M.; Heathcote, S. L.; Harris, D. K.; Chen, O. Evolution of the Single-Nanocrystal Photoluminescence Linewidth with Size and Shell: Implications for

Exciton–Phonon Coupling and the Optimization of Spectral Linewidths. Nano Lett. 2015, 16, 289-296.

15. Cui, J.; Beyler, A. P.; Marshall, L. F.; Chen, O.; Harris, D. K.; Wanger, D. D.; Brokmann, X.; Bawendi, M. G. Direct Probe of Spectral Inhomogeneity Reveals Synthetic Tunability of Single-Nanocrystal Spectral Linewidths. Nature Chem. 2013, 5, 602-606.

16. Chen, O.; Wei, H.; Maurice, A.; Bawendi, M.; Reiss, P. Pure Colors from Core–Shell Quantum Dots. MRS Bulletin 2013, 38, 696-702.

17. Empedocles, S. A. Quantum-Confined Stark Effect in Single Cdse Nanocrystallite Quantum Dots. Science 1997, 278, 2114-2117.

18. Beyler, A. P.; Marshall, L. F.; Cui, J.; Brokmann, X.; Bawendi, M. G. Direct Observation of Rapid Discrete Spectral Dynamics in Single Colloidal Cdse-Cds Core-Shell Quantum Dots. Phys. Rev. Lett. 2013, 111, 177401.

19. Salvador, M. R.; Graham, M. W.; Scholes, G. D. Exciton-Phonon Coupling and Disorder in the Excited States of Cdse Colloidal Quantum Dots. The Journal of Chemical Physics 2006, 125, 184709.

20. Currie, M. J.; Mapel, J. K.; Heidel, T. D.; Goffri, S.; Baldo, M. A. High-Efficiency Organic Solar Concentrators for Photovoltaics. Science 2008, 321, 226-228.

21. Bronstein, N. D.; Li, L.; Xu, L.; Yao, Y.; Ferry, V. E.; Alivisatos, A. P.; Nuzzo, R. G. Luminescent Solar Concentration with Semiconductor Nanorods and Transfer-Printed Micro-Silicon Solar Cells. ACS Nano 2013, 8, 44-53.

22. Brovelli, S.; Schaller, R. D.; Crooker, S. A.; García-Santamaría, F.; Chen, Y.; Viswanatha, R.; Hollingsworth, J. A.; Htoon, H.; Klimov, V. I. Nano-Engineered Electron–Hole Exchange Interaction Controls Exciton Dynamics in Core–Shell Semiconductor Nanocrystals. Nat. Commun. 2011, 2, 280.

23. Coropceanu, I.; Bawendi, M. G. Core/Shell Quantum Dot Based Luminescent Solar Concentrators with Reduced Reabsorption and Enhanced Efficiency. Nano Lett. 2014, 14, 4097-4101.

24. Debije, M. G.; Verbunt, P. P. C. Thirty Years of Luminescent Solar Concentrator Research: Solar Energy for the Built Environment. Adv. Energy Mater. 2012, 2, 12-35.

25. Hu, J. Linearly Polarized Emission from Colloidal Semiconductor Quantum Rods. Science 2001, 292, 2060-2063.

26. McDowall, S.; Johnson, B. L.; Patrick, D. L. Simulations of Luminescent Solar Concentrators: Effects of Polarization and Fluorophore Alignment. J. Appl. Phys. 2010, 108, 053508.

27. Mulder, C. L.; Reusswig, P. D.; Velazquez, A. M.; Kim, H.; Rotschild, C.; Baldo, M. A. Dye Alignment in Luminescent Solar Concentrators: I. Vertical Alignment for Improved Waveguide Coupling. Opt. Express 2010, 18, A79-A90.

28. Wang, T.; Zhang, J.; Ma, W.; Luo, Y.; Wang, L.; Hu, Z.; Wu, W.; Wang, X.; Zou, G.; Zhang, Q. Luminescent Solar Concentrator Employing Rare Earth Complex with Zero Self-Absorption Loss. Solar Energy 2011, 85, 2571-2579.

29. Botta, C.; Betti, P.; Pasini, M. Organic Nanostructured Host-Guest Materials for Luminescent Solar Concentrators. Journal of Materials Chemistry A 2013, 1, 510-514.

CHAPTER 2

The Synthesis and Characterization of CdSe/CdS Quantum Dots and Nanorods

From the very beginning of the field of colloidal quantum dots, the material CdSe has played a central role in the field. Fundamental studies of CdSe nanocrystals were critical in unraveling the complex behavior of quantum dots, from their general electronic structure to the dynamics of single particles.[1, 2] Likewise, it was CdSe that opened the gates to a variety of practical applications of quantum dots in areas such as biological imaging and electroluminescent devices.[3] This entire body of work was made possible by a series of synthetic advances which produced particles which were: 1) uniform at the batch level, 2) tunable in size and shape, and 3) exhibited a high fluorescence quantum yield and 4) exhibited long-term photostability.[1, 4, 5]

Early in the development of colloidal quantum dots, it became apparent that the optical quality of the structures could be improved by surrounding the original dot (now called the core) with a second inorganic layer (called the shell).[6] For luminescent applications the most important role of the shell is to help confine the exciton in and around the core and to protect it from defects and perturbations on the surface. The requirement to confine the exciton close to the core dictates that as a prerequisite the shell must have a higher band gap than the core. In addition, the band-alignment at the interface should be such

that both the conduction and valence bands of the shell material lie higher in energy than the corresponding bands in the core material.

This situation is shown diagrammatically in Fig 2-1 below. The strongest confinement occurs when a high band offset exists for both the conduction and valence bands, called a type-I heterojunction. For example, in the case of CdSe, such an arrangement can be achieved when overcoating the core with a material such as ZnS.[7] In contrast, if one of the bands of the shell lies close in energy to the corresponding band in the core, one can achieve what is called a quasi – type-II band alignment. For example, in the case of CdSe, such an arrangement is found when CdS is used as the shell material. In this case, the low barrier between the conduction bands allows for significant electron delocalization into the shell.[7, 8] The implication of this delocalization for the electronic and optical properties of CdSe/CdS nanostructures is discussed in detail in Ch. 4.

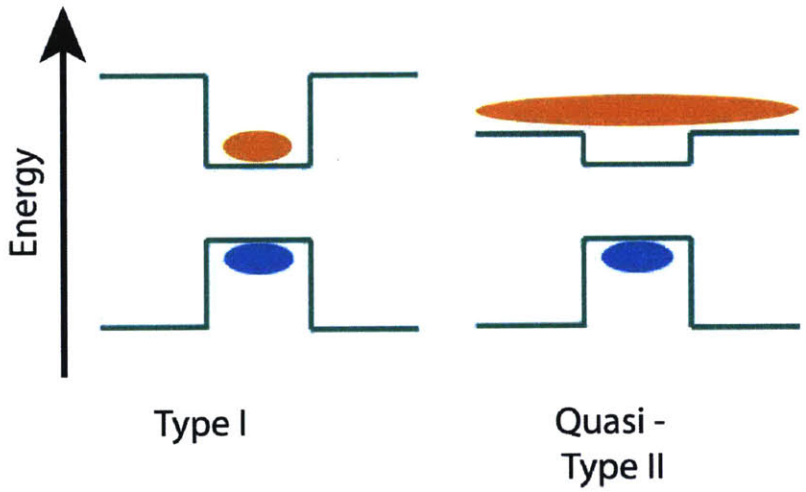

Figure 2-1: Type I and Quasi - Type II Core/Shell Heterojunctions; the spread of the electron wavefunction is shown in organge and the spread of the hole wavefunction is shown in blue

2.1 Thick-Shell CdSe/CdS Quantum Dots

Of all the shell materials used to overcoat CdSe quantum dots, CdS has been remarkable successful in creating heterostructures with superlative optical properties. The CdSe/CdS system has produced particles with unity fluorescence quantum yields, high biexciton quantum yields, minimal inhomogeneous broadening, and highly suppressed blinking.[4, 9-13] Due to these properties, CdSe/CdS quantum dots have been integrated into a wide variety of applications, ranging from light emitting devices, biological imaging, and other optical and optoelectronic applications.[14, 15]

The versatility of CdSe based quantum dots has been dramatically expanded recent synthetic advances in the growth of a thick CdS shell. Such thick-shell CdSe/CdS dots can now be grown while retaining a high degree of

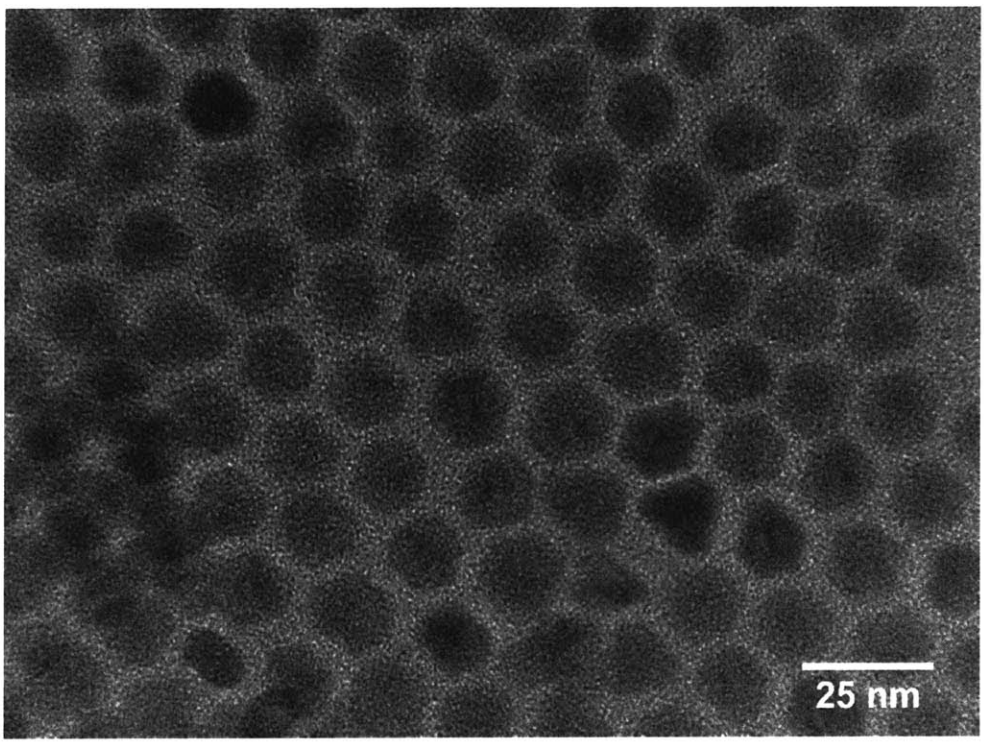

Figure 2-2: TEM micrograph of thick-shell Cdse/CdS quantum dots

monodispersity at the batch level, near unity quantum yields, and narrow fluorescence lineshapes. These thick-shelled particles have proven especially attractive for applications that require minimal reabsorption, such as luminescent solar concentrators and to a lesser degree in displays.[10, 16] The reduction in reabsorption is made possible by effectively decoupling the absorption and emission of these particles. While high energy light will mostly be absorbed into the shell, the exciton created in this process will rapidly relax in energy and localize in the core, where it can finally recombine radiatively. This idea will be discussed in more detail in the next chapter.

While numerous methods exist to grow the CdS shell on these particles, the best results have been obtained using a slow-injection high temperature growth that has previously been reported[4] and which we adapted for thick-shell CdSe/CdS dots. Two of the biggest advantages of this method is that it yields particles with a high degree of uniformity at the batch scale (e.g. see Fig. 3-3) and near unity quantum yields. These advantages appear to follow from the high degree of crystallinity of the shell which reduces the number of non-radiative channels that otherwise can reduce the quantum yield. The benefit of this passivation scheme is especially striking for particles with very thick shells (15+ monolayers of CdS). In these particles, electron delocalization into the shell results in a dramatic lengthening of the radiative lifetime (from ~20 ns to hundreds of ns). Nevertheless, because the non-radiative decay channels are so efficiently suppressed, the radiative pathways can still dominate, allowing from fluorescence quantum yields up to 100%.

2.1.1 The Evolution of the Biexciton Quantum Yield in CdSe/CdS Quantum Dots as a Function of the Shell Thickness

As another illustration of the benefit of the shell in CdSe/CdS heterostructures, we have looked at the evolution of the biexciton quantum yield. In core only CdSe or related system, the biexciton quantum yield is generally no higher than ~3%.[11] This low quantum yield is generally attributed to Auger-mediated non-radiative relaxation of the biexciton to the exciton.[17, 18] Because the Auger process depends on the wavefunction overlap of the core and electron wavefunction, its rate can be inhibited by increasing the separation between the two charge carriers.[11, 17, 19] Indeed, when looking at a series of CdSe/CdS quantum dots one observes a monotonic increase in the biexciton quantum yield as seen in Fig 2-3. In fact, by using an extension of this approach combined with partial alloying, more recent studies have demonstrated that that the biexciton quantum yield can even be made to reach unity.[13]

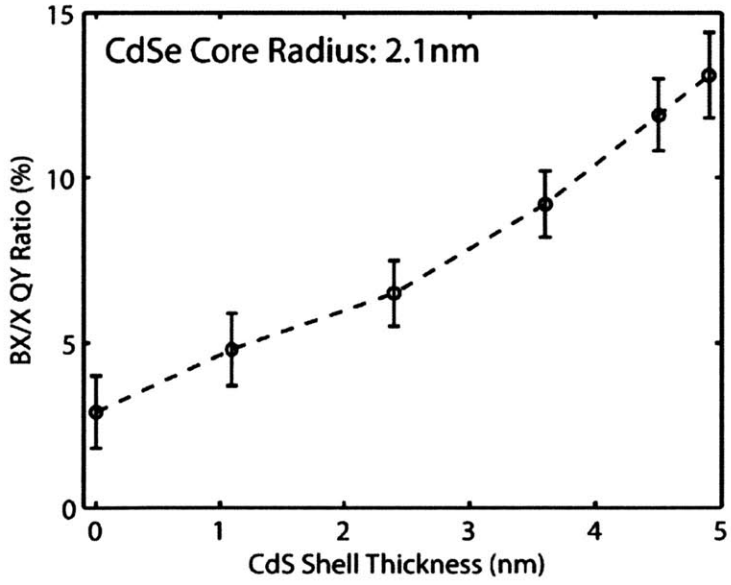

Figure 2-3: The change in the biexciton quantum yield vs. CdS shell thickness

2.2 CdSe/CdS Nanorods

The versatility of inorganic nanocrystals is greatly expanded by the possibility of modifying their electronic properties by changing not only their size, but also their dimensionality. In particular, elongated structures such as nanorods exhibit an attractive set of emergent properties that set them apart from spherical quantum dots, such as a large degree of fluorescence anisotropy[20, 21] and enhanced transport through various types of biological tissue[22]. Among visible-light emitting materials, seeded CdSe/CdS nanorods (structures consisting of a spherical CdSe core surrounded by an elongated CdS shell) have emerged as a robust material system combining a high degree of monodispersity with bright and spectrally narrow photoluminescence. However, while rapid initial progress in the development of CdSe/CdS nanorods resulted in the achievement of fluorescence quantum yields of up to 75%[20, 23], further improvement of the quantum yield proved elusive using conventional fast-injection based preparations. Moreover, as with CdSe/CdS quantum dots, the quantum yield was rapidly observed to decrease with increasing shell volume, an effect which was attributed to the long radiative lifetimes caused by delocalization of the electron into the shell.[20] This reduction in the efficiency has been a significant barrier to these materials for a variety of optical and optoelectronic applications, such as luminescent solar concentrators (LSCs) and light emitting diodes (LEDs).[10, 24-27]

In this work, we have employed a two-step process to synthesize the shell by first using a hot injection reaction to grow a thin CdS layer, followed by a slow second growth. The first step is needed to maintain kinetic control over the initial growth of the shell in order to obtain a monodisperse batch of nanorods with a well-defined elongated geometry, as previously reported[6]. The second slow growth in turn was motivated by our previous work on spherical CdSe/CdS quantum dots, where a slow high temperature growth was seen to improve both the synthetic and optical quality of the nanoparticles. In our study we show that the second growth step not only improved the crystallinity of the nanorods but

had a major impact on the optical properties, increasing the fluorescence quantum yield up to unity, highly suppressing residual defect emission, and allowing for complete energy transfer from the shell to the core. Our approach highlights the benefits of decoupling the growth of anisotropic heterostructures into two steps: 1) a fast step needed to direct the shape and size of the nanostructures and 2) a slow annealing step to reduce the defects introduced by the fast growth to highly suppress the non-radiative channels that reduce the fluorescence quantum yield.

2.2.1 Synthesis

The general synthetic scheme for the shell growth is illustrated in Fig. 2-4. Spherical CdSe cores were first overcoated using an established fast injection-based recipe[20] to yield thin-shelled CdSe/CdS nanorods with a high degree of monodispersity. These nanorods were then isolated and in a second reaction the shell was grown further using a high-temperature, slow-injection reaction. The second growth provided two key advantages: 1) an increase in the fluorescence

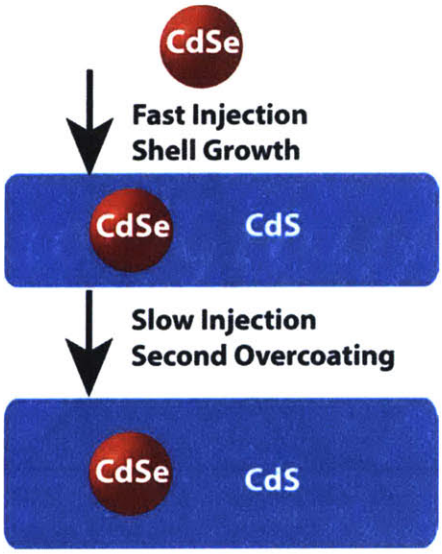

Figure 2-4: The general synthetic scheme for the synthesis of the seeded nanorods

quantum yield and a suppression of the trap emission and 2) independent control of the shell thickness. This synthetic protocol resulted in nanorods that remained very monodisperse at the batch level even as the shell thickness was continuously increased. In order to study the effective monodisperisty of the sample as it relates to the optical properties of the system, the ensemble and average single nanorod spectral correlations were measured using solution-Photon Correlation Fourier Spectroscopy (s-PCFS, see Fig. 2-5)[9]. From the small difference between the two spectral correlations, one can readily conclude that the inhomogeneous broadening of the sample only results in a minor contribution to the overall spectral width. In addition, the particles were highly uniform and crystalline at the individual nanorod level as can be seen from the high resolution TEM in Fig 2-6a and 2-6b. The uniformity achieved after the second growth step appears to be a significant improvement from the initial nanorods, where the fast injection frequently results in the appearance of visible kinks as well as other crystallographic defects such as edge dislocations (see Fig. S3).

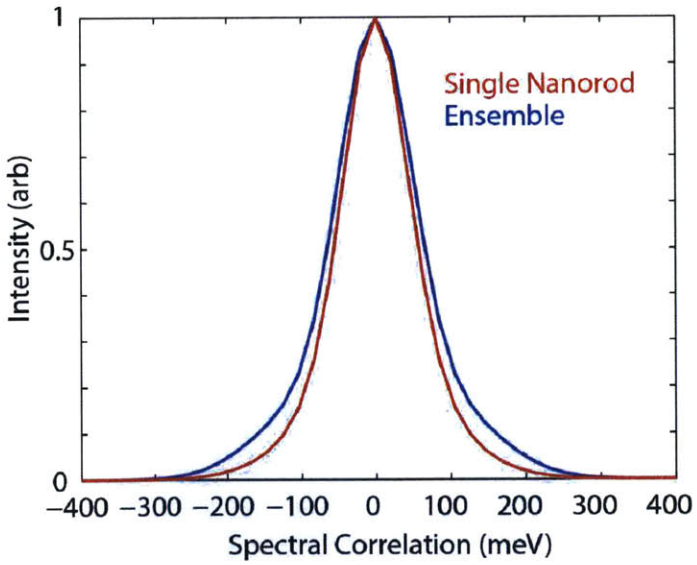

Figure 2-5: s-PCFS traces showing the ensemble and average single nanorod spectral correlation of sample

Table 1: Dimensions and Fluorescence Quantum Efficiency of Nanorod Samples

Sample	Length (nm)	Width (nm)	Fluorescence Lifetime (ns)	Quantum Yield (%)
F1	44±4	5.5±0.2	14	59 ± 1
S1	45±3	6.3±0.2	23	95 ± 1
S2	42±3	7.0±0.2	29	98 ± 2
S3	40±3	9.5±0.2	61	85 ± 1

In order to systematically study the evolution of the electronic and optical properties of the new nanorods, a size series was prepared by first creating a batch of nanorods using the conventional fast-injection based growth (denoted F1)[20], which was then subjected to an additional slow growth steps to create two new samples, which we denoted in the order of increasing thickness as S1, S2. Finally in order to even more drastically increase the shell thickness, sample S1 was subjected to one additional slow growth, yielding the sample denoted S3. As can be seen from table 1, while the length of all the four samples is almost unchanged (ranging from 40nm to 45nm) as additional growth along the axial direction was balanced by the general tendency of the particles to become more spherical after prolonged reaction times. In contrast, the thickness increased continuously from 5.5nm for F1 to 6.3, 7.0, and 9.5 in S1, S2, and S3 respectively. By taking into account the initial size of the core (d=4.9nm) and the thickness of each individual CdS layer, we can estimate the change in the number of CdS monolayers (estimated assuming each layer of CdS had a

thickness of 0.35nm) to be from 1 in F1 to 2, 3, and 7 respectively in S1, S2, and S3.

One key advantage of dividing the shell growth in two steps is to allow for an independent control of the length and thickness of the nanorods, allowing for the synthesis of uniform particles with a wide range of aspect ratios for any particular length. While conventional fast growth techniques yield highly uniform particles with a tunable length, changing the thickness has proven to be much more challenging since varying most synthetic parameters such as the amount of precursors injected and the reaction time predominantly affects the length while leaving the thickness largely unchanged.[20, 21] While some progress has been reported for preparing thicker shelled nanorods by using a higher injection temperature, this approach nevertheless still resulted in coupled growth of the nanorods along both their long and short axes.[28] In contrast, using our method, the first step results predominantly in growth along the long axis, while the second step occurs under conditions that promote symmetric growth in all directions[4, 6] Therefore, by carefully selecting the reaction conditions our method allows for core/shell nanorods with a desired combination of length and thickness. As a final note, because the shell is in equilibrium with the reaction precursors, under conditions that promote isotropic growth particles tend to become rounder. As a result, during the second step, the length may remain constant or even decrease even as the volume is increasing. This fact should be taken into account when designing the growth of the shell in order to obtain the target dimensions.

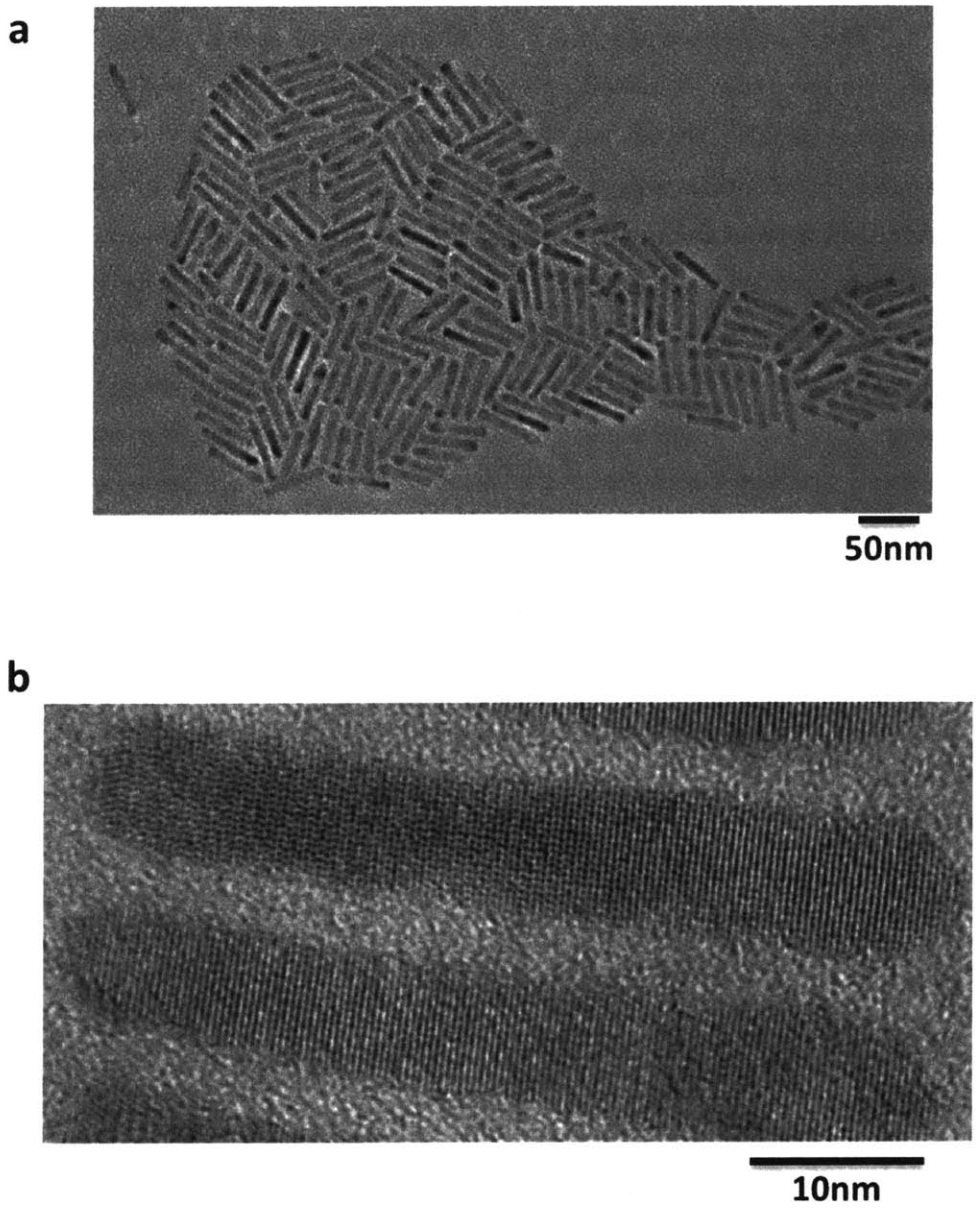

Figure 2-6: TEM micrograph of the nanorods after the slow-shell growth: a) a micrograph of sample S1 d) High Resolution TEM micrograph of sample S2

2.2.2 Optical Characterization

The fluorescence spectra of these samples are shown in Fig. 2-7a. As the shell volume was increased, the spectra continuously redshifted and the lineshapes slightly broadened as expected from the known tendency of the electron to delocalize into the shell across the quasi type-II barrier typical of CdSe/CdS heterostructures[8, 29]. An interesting qualitative difference between the spectra is revealed when re-plotting the data on a logarithmic scale (Fig 2-7b). In addition to the band-edge luminescence, one can distinguish an additional red-shifted band in some of the spectra. Such a feature is ubiquitous to CdSe or CdS based nanoparticles and while its origin has not been definitively identified, it is generally attributed to defect states either at the surface of the nanoparticle or at the core/shell interface and is for this reason usually denoted as the *trap band* in these materials.[30] What is interesting is that while this feature is strongly pronounced in the initial CdSe cores and still clearly apparent in the initial nanorods, this band is highly suppressed in the samples subjected to the second slow shell growth. Indeed the feature is essentially undetectable in the two

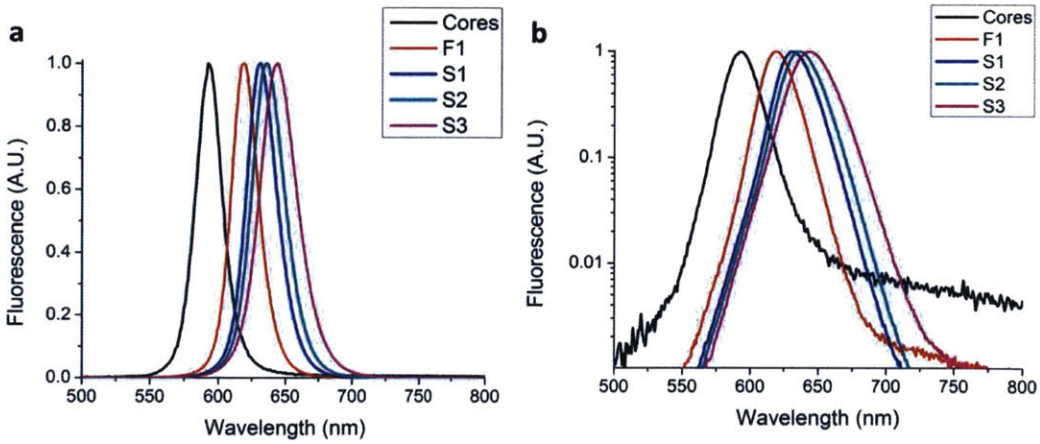

Figure 2-7: a) Fluorescence spectra of the CdSe cores and the nanorods on a linear scale and b) on a logarithmic scale

thinner nanorod samples (S1 and S2) and only re-emerged in the thickest sample (S3), but even then remained much weaker than in the initial nanorods.

The observed reduction in the defect band can be linked to the large degree of uniformity and crystallinity of the shell and the improved passivation of the surface made possible by the slow growth step. Such a behavior is fully consistent with the improved optical performance obtained in our previous work on spherical CdSe/CdS quantum dots[4, 10]. Importantly both in the case of the nanorods as well as the quantum dots the suppression of the defect band is not simply a function of the CdS shell thicknesss but always requires the slow growth step. This behavior can be clearly seen in the case of the CdSe/CdS QDs where the fluorescence spectra for a series of aliquots are shown in Fig. S6a/b, all grown using a high temperature slow-injection growth as described in Ref. 5. No defect band is apparent in any of the spectra, even for the lowest shell thickness. In addition, samples of CdSe/CdS nanorods grown using the fast injection growth from a smaller initial core do exhibit such a defect band (Fig. S6c/d), even if the

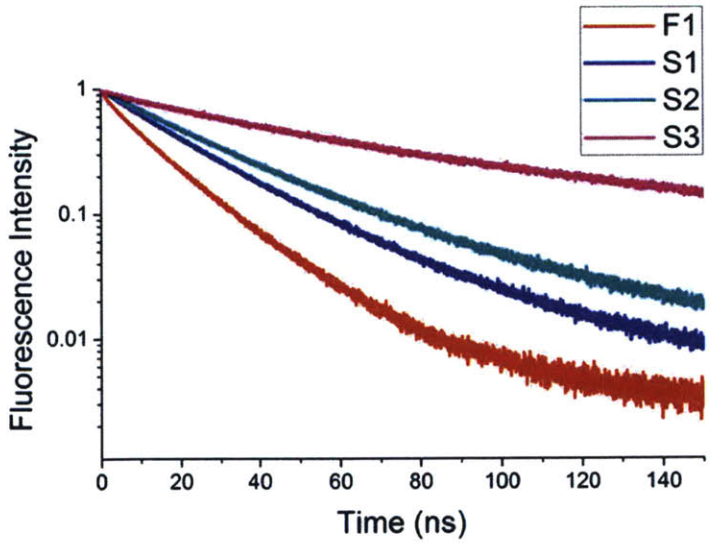

Figure 2-8: Time resolved photoluminescence traces of the nanorod samples

shell is thicker than when starting from a larger core as in our present study[21]. These observations highlight the fact that it is the use of a slow high temperature growth step that is the key factor enabling the suppression of the defect band and the more general improvement in the optical properties.

The fluorescence quantum yield of the four nanorod samples were then measured using an integrating sphere (see Table 1). The excitation wavelength was selected to be 405nm in order to ensure that the majority of the absorption occurred directly into the shell. The initial quantum yield of the nanorods after the first growth was only moderate at 59%, which already represented a reduction from the higher values (70%+) measured for nanorods made from the same batch of cores but having a shorter shell. Upon growing a thin shell using the slow growth method (sample S1), the quantum yield increased to 95%. A similar sample having a thicker shell (S2) was measured to have a quantum yield of 98%. This significant increase in the quantum yield even as the shell volume was increased, suggests a strong suppression of the non-radiative decay channels present in the initial nanorods. It was only when growing the shell further that the quantum yield decreased, a value of 85% being measured for the thickest-shelled nanorods in this series. This final decrease in the quantum yield may largely be due to the gradual lengthening of the radiative lifetime as the shell volume was increased (see Fig. 2-8), which again made the remaining non-radiative decay channels competitive with radiative recombination.

The evolution of the normalized absorption spectra from the CdSe cores to the nanorod series is shown in Fig. 2-9. At high energies (above 500nm), where most of the absorption is mediated by the CdS shell, the spectra remain relatively constant, barring the gradual disappearance of the sharp features as the CdS shell gradually transitions from the quasi-one dimensional confinement to its bulk-like limit. However, as in the case of spherical CdSe/CdS quantum dots, the biggest change observed in the spectra consists in the relative reduction of the first excitonic features (see the inset of Fig. 2-9) compared to the CdS band as

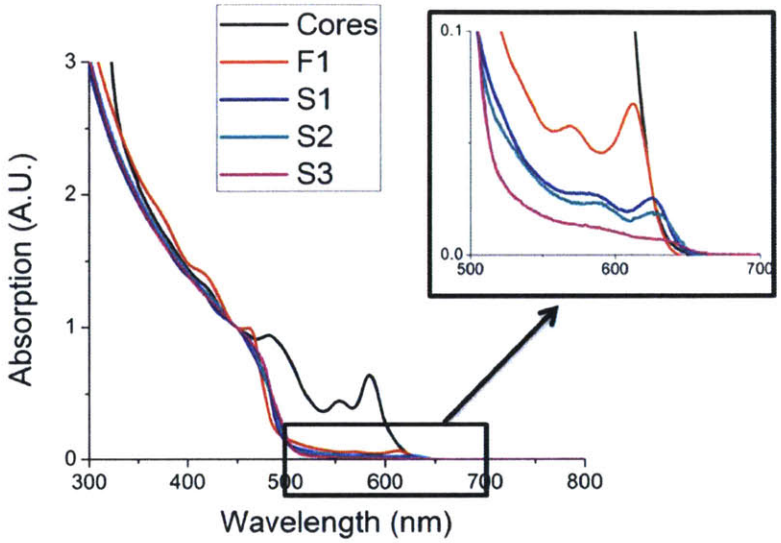

Figure 2-9: Absorption spectra of nanorods (inset magnification of first excitonic feature

the volume of the shell increases and consequently the volumetric ratio of CdSe to CdS decreases.[10] Because virtually all of the spectral overlap between the emission and absorption spectra of the nanorods occurs through this first excitonic feature, its relative reduction directly leads to a decrease in the effective reabsorption of these materials. Indeed, for the sample with the largest shell volume (S3), the absorption at the fluorescence maximum is reduced by two orders of magnitude compared to its value in the CdS band. Such a low reabsorption is comparable to values previously reported for giant-shelled CdSe/CdS quantum dots and represents one of the lowest levels of reabsorption measured in inorganic or organic materials.

2.2.3 Evaluation of the Shell-to-Core Energy Transfer Efficiency

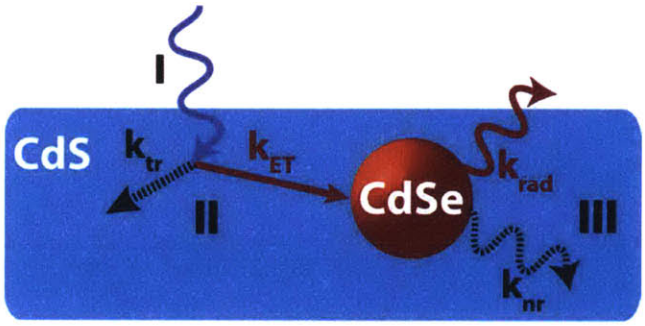

Figure 2-10: Electronic processes in CdSe/CdS nanorods, including I) absorption, II) shell-to-core energy transfer, III) fluorescence and the trapping pathways before and after thermalization

One key property exhibited by the nanorods grown using the current method is that in contrast to other large volume CdSe/CdS particles, they exhibit effectively complete energy transfer from the shell to the core. Such a result could be anticipated from the fact that a unity quantum yield was measured even when exciting at 405nm, where most of the absorption occurred directly into the shell. A more systematic demonstration of this property follows from the analysis of the excitation-emission spectrum of the nanorods, shown in Fig. 2-11a, which shows the variation of the fluorescence spectrum of the nanorods as a function of the excitation wavelength. Upon normalizing the spectrum to the peak of the fluorescence at each excitation wavelength (Fig 2-11b), it is apparent that the spectrum remains completely unchanged, suggesting that the exciton is always able to equilibrate on a time scale much faster than the fluorescence lifetime. Upon taking a cross-section of the 2D plot prior to normalization (or equivalently directly measuring an excitation spectrum), the resulting spectrum tracks the absorbance spectrum completely, as shown in Fig. 2-12. This property means that the quantum yield of the particles is insensitive to the excitation wavelength.

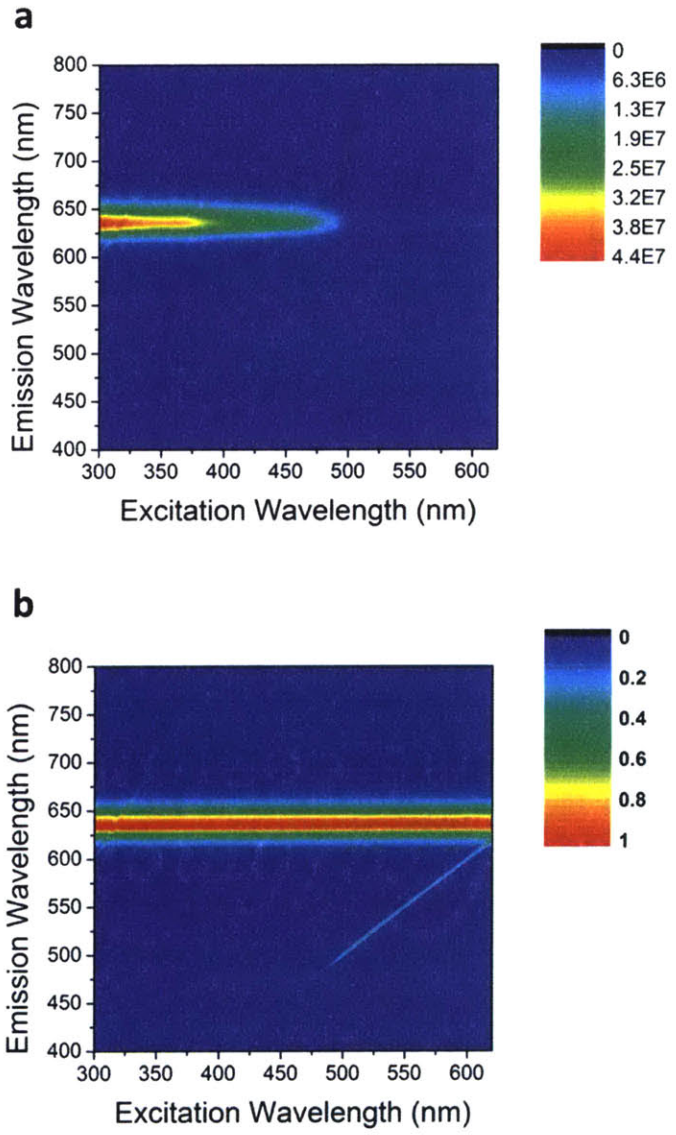

Figure 2-11: a) Excitation-emission spectrum of CdSe/CdS nanorods (S2). b) Normalized excitation-emission spectrum of S2

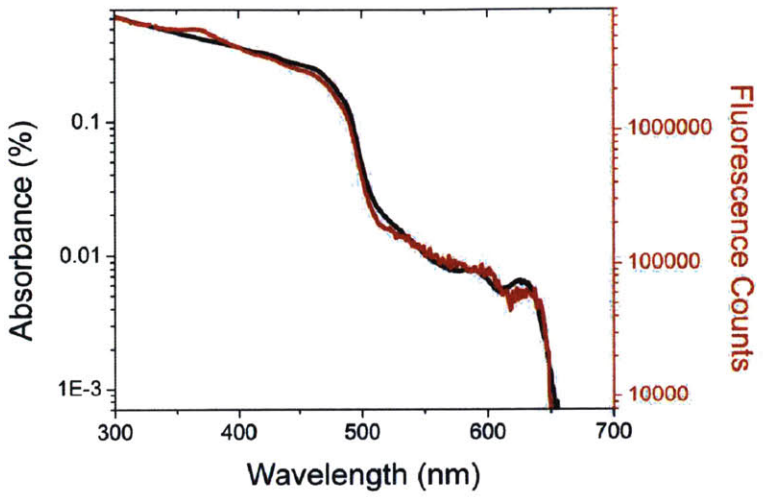

Figure 2-12: Excitation spectrum and absorbance of S2

The fact that the energy transfer in these nanorods is significantly more efficient than in conventional nanorods of similar dimensions indicates that the slow growth step results in a suppression of the surface traps that can otherwise prevent the exciton from localizing to the core.[31] This general behavior can be understood within the general scheme shown in Fig. 2-10. If the nanorod is excited well above its effective bandgap, the exciton that will be generated will mostly be delocalized in the CdS shell (I). In order for the exciton to eventually recombine radiatively in the core, it must successfully pass through two branching ratios. First, the hot exciton must localize in and around the core (II) upon thermalization (at an effective rate k_{ET}) in competition with the parasitic pathways that can trap the exciton or one of the charge carriers in the shell (at a rate k_{tr}). Finally, the exciton must recombine radiatively (III) at a rate k_{rad} in competition with all the remaining non-radiative decay channels (k_{nr}). Because both the localization rate[32] as well as the radiative rate are known to decrease with the shell volume, the fact that nanorods subjected to the slow growth step can exhibit a unity quantum yield when excited into the shell indicates a strong

suppression of all the non-radiative channels operating both before and after the thermalization of the exciton. It should be pointed out that upon magnifying the spectral range around 500nm, one can observe a very small peak as shown in figure 2-13, presumably due to emission of light from the CdS shell prior to thermalization. The integrated area of this feature is about 10,000 weaker than the integrated band-edge spectrum, which is consistent with the fact that the typical carrier localization timescale (~40ps) is about 1000-10000 times shorter than the typical intrinsic radiative lifetime of CdS nanostructures (~10ns).

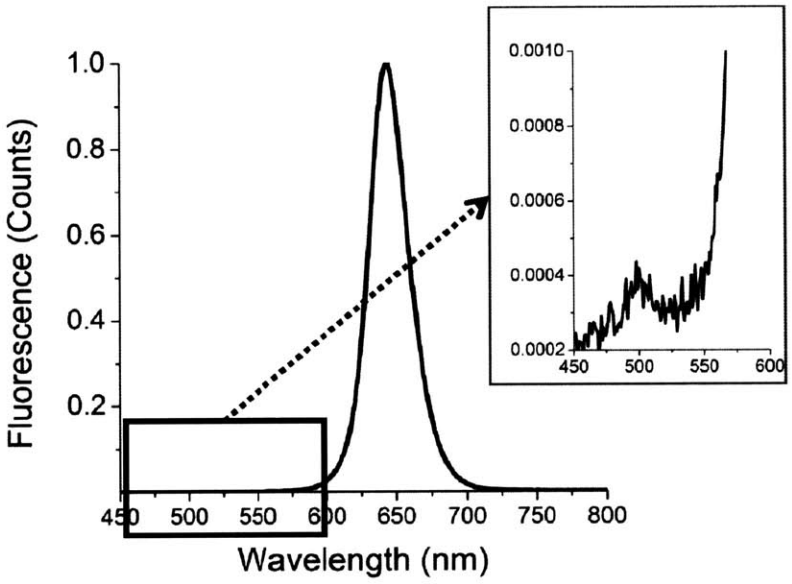

Figure 2-13: Fluorescence Spectrum of S2. Inset shows the weak CdS emission peak at a magnification of 10KX

2.2.4 Evaluation of the Degree of Polarization in the Fluorescence of CdSe/CdS Nanorods

Finally, in order to assess the degree of polarization of the nanorods, we performed polarization-dependent single particle fluorescence spectroscopy. In particular we were interested to see whether the thickest shell nanorods would exhibit the same degree of polarization (P, defined as the difference of the orthogonally polarized components of the fluorescence divided by the total fluorescence intensity) as the conventional, thinner nanorods obtained after the initial first injection. The experimental set-up that was used is shown schematically in Fig. 4a (a detailed description of the experiment is described in the supplementary information). The sample consisted of a dilute solution of nanorods spun cast onto a coverslip, which allowed for a clear separation between individual particles. The nanorods (sample T1, which was synthesized using a similar procedure used for sample S3) had a length of 63nm and a thickness of 10nm, resulting in an aspect ratio (the ratio of the length to the width) of approximately 6. A typical trace showing variation of the fluorescence intensity as a function of the polarizer angle is shown in Fig 4b, from which the degree of polarization can be estimated to be 65%. This value is comparable to values that have been previously reported for nanorods that had a similar aspect ratio, but with a thinner shell (and a proportionately shorter length). Such a result is consistent with the theoretically predicted component of the fluorescence polarization that is attributable to the dielectric environment, as this contribution should only depend on the aspect ratio rather on the ratio of the length and the width of the shell, rather on their absolute dimensions.[33]

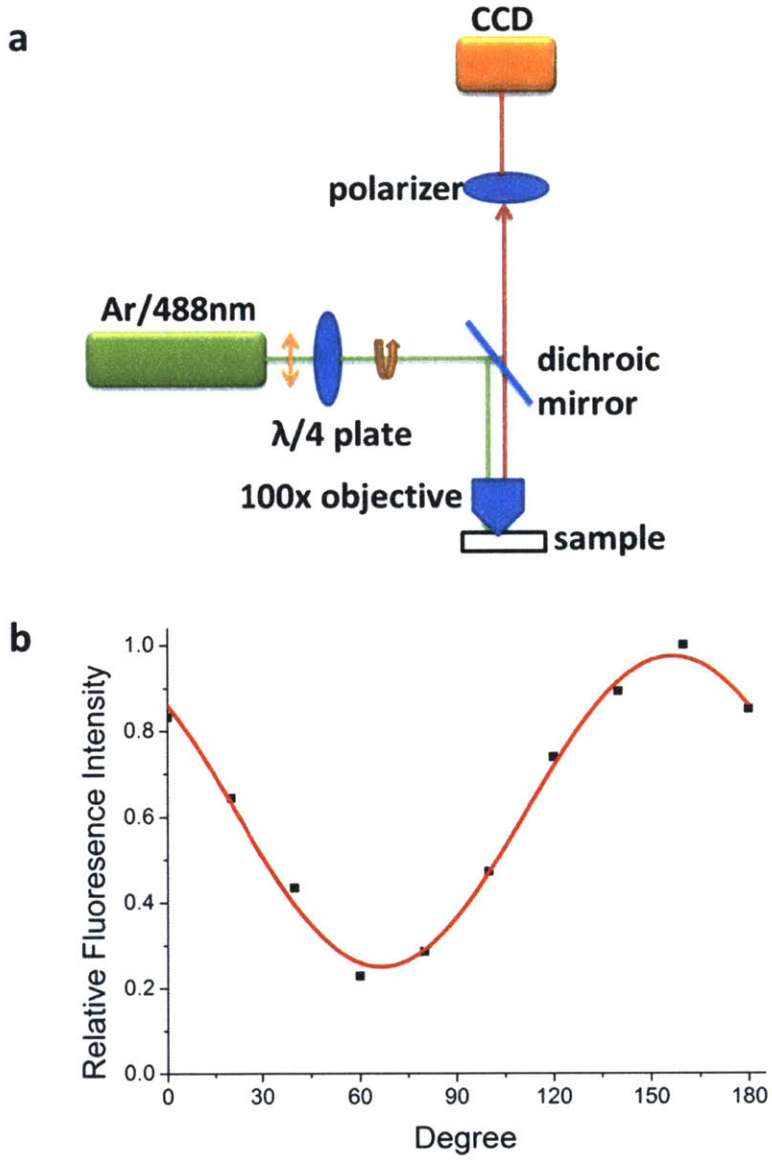

Figure 2-14: Schematic of the set-up used for polarization dependent single nanorod fluorescence spectroscopy b) Fluorescence intensity of sample T1 as a function of the polarizer angle

2.3 Conclusions

In conclusion, we have developed a two-step method to grow an elongated CdS shell on CdSe cores, yielding highly monodisperse nanorods with tunable shell thickness and near unity quantum yields. The nanorods also exhibited highly efficient energy transfer from the shell to the core, making the structures well-suited for broadband light harvesting. The improvement in the optical properties of the system may be attributed to the increased uniformity and crystallinity of the shell made by possible by the long reaction time of the second growth. This result extends the same optimization that we previously reported for spherical giant-shelled CdSe/CdS particles to a quasi-one dimensional geometry where the good optical properties can be combined with linear polarization. We believe that these new materials may be good candidates for a variety of optical applications such as luminescent down-shifting and luminescent solar concentrators.[10, 16]

2.3.1 Materials and Methods

Synthesis: The synthesis of the CdSe cores and the first fast-injection shell growth was carried out by following a previously published synthetic recipe. The second step of the shell growth consisted of a slow high temperature CdS growth, adapted from Ref [4] and is described in detail in the supplementary information.

Optical Imaging: Absorption spectra were recorded using a Cary 5000 spectrophotometer and emission spectra were recorded using a Fluoromax-3 spectrofluorometer. Quantum yield measurements were taken using a Labsphere integrating sphere using a 5mW, 405nm as the source, chopping the beam at 210 Hz and collecting the output using a calibrated silicon detector through a Stanford Research Systems lock-in amplifying system. A filter was used to spectrally separate the fluorescence, and the final quantum yield was corrected the reflectance and leakage of the filter.

Time Resolved Photoluminescence: To measure the PL lifetime, the nanorods were diluted in a hexane solution, placed in a quartz cuvette and excited with a pulsed 532 nm laser (PicoQuant) at a 2.5 Mhz repetition rate. The excitation light was removed using a spectral filter and the emission was collected by a single photon avalanche photodiode (Micro Photon Devices). The photon arrival time was correlated with the excitation pulse by a Picoharp 300 (PicoQuant) time-correlated single photon counting system.

Single Particle Fluorescence: The excitation source was a beam of 488nm light from an argon ion laser, which was rendered circularly polarized using a quarter-wave plate and then focused unto the sample using a 100x oil immersion objective. The emitted light was passed through a polarizer and was finally collected by a CCD camera. The fluorescence was connected with 30s integration windows for each data point as the polarizer was moved stepwise by 20^{o} from 0^{o} to 0^{o}.

2.4 Supplementary Information

2.4.1 Synthesis of CdSe/CdS Quantum Dots

Chemicals: 1-octadecene (ODE, 90%), trioctylphosphine oxide (TOPO 99%), trioctylphosphine (TOP, 97%), oleylamine (OAm, 70%), 1-octanethiol (> 98.5%), sulphur powder (99.999%) were obtained from Sigma Aldrich. Cadmium oxide (CdO, 99.998%), selenium powder (99.999%), oleic acid (OLA, 90%) and octadecylphosphonic acid (ODPA, 97%) were purchased from Alfa Aesar.

Synthesis of Thickest Shell Dots:

To a 250mL round bottom flask was added 100nmol of the CdSe cores (with a maximum of the first excitonic feature in the absorbance spectrum at 572nm) dissolved in hexane, 3mL of ODE, and 3mL of oleylamine. The solution was degassed at r.t. for 1 hr. and then for 5 min at 100°C to remove the hexane and water. The solution was then stirred under N_2 and the temperature was raised to 310°C. At 200°C, a solution of Cd-oleate (8mL of a 0.2M solution of Cd-oleate in ODE) dissolved in ODE and a separate solution of octanethiol (328μL) dissolved in ODE (for a total volume of 20mL for each) were injected at a rate of 2.5mL/hr. After 2 hours 2 mL of oleic acid was injected and after 4 hours from the time of injection and additional 2mL of oleic acid was added. After 8 hrs. the solution was stirred for an additional 15 minutes at 310°C, then the heating mantle was removed. The final product was obtained by precipitation with acetone.

Synthesis of Dots with Different Shell Thicknesses:

The same general protocol as for the thickest-shelled dots was used, with the difference that the amounts of the precursor reagents (Cd-oleate and octanethiol) as well as the injection times were reduced proportionally to yield the desired shell-thickness.

2.4.2 Synthesis of CdSe/CdS Nanorods

Chemicals: 1-octadecene (ODE, 90%), trioctylphosphine oxide (TOPO 99%), trioctylphosphine (TOP, 97%), oleylamine (OAm, 70%), 1-octanethiol (> 98.5%), sulphur powder (99.999%) were obtained from Sigma Aldrich. Cadmium oxide (CdO, 99.998%), selenium powder (99.999%), oleic acid (OLA, 90%) and octadecylphosphonic acid (ODPA, 97%) were purchased from Alfa Aesar.

1. 1 Initial Nanorod Growth (F1)

The initial seeded nanorods were prepared by following the procedure reported by Carbone et al [1], using CdSe cores with a maximum of the first excitonic feature in the absorbance spectrum at 585nm. Briefly, 3.0g trioctylphosphine oxide, 290mg octadecylphosphonic acid, 90mg hexylphosphonic acid, and 90mg of CdO were added to a 50mL RBF and degassed as 150oC for one hour. The solution was then heated up to 300 oC under N2 in order to crack the CdO. In a separate vial, 100nmol of the CdSe cores were concentrated, 120mg of S was added, and the solids were dissolved in 2mL of trioctylphosphine at ~80oC. The main reaction solution was then heated to 350 oC and 1.5mL trioctylphosphine was added. Finally, once the reaction reached the final temperature, the cores/S solution was rapidly injected and the reaction was allowed to proceed for 10min. after which the heating mantle was removed. The nanorods were then precipitated using a mixture of methanol and butanol and were redispersed in hexane.

1.2 Second Slow Growth

F1

To a 250mL round bottom flask was added 40nmol of the initial CdSe/CdS cores nanorods dissolved in hexane, 3mL of ODE, 3mL of oleylamine, and 3mL of oleic acid. The solution was degassed at r.t. for 1 hr. and then for 20 min at 80oC to remove the hexane and water. The solution was then stirred under N2 and the

temperature was raised to 310oC. At 200oC, a solution of Cd-oleate (1mL of a 0.2M solution of Cd-oleate in ODE) dissolved in ODE and a separate solution of octanethiol (42μL) dissolved in ODE (for a total volume of 6mL for each) were injected at a rate of 3mL/hr. The final solution was then cooled down and the nanorods were collected by precipitation using acetone followed by re-dispersion in hexane.

F2

The procedure for F1 was repeated with the difference that the amount of the shell precursors used was 2mL of a 0.2M solution of Cd-oleate in ODE and 42μL of octanethiol.

1.3 Additional Shell Growth

To a 250mL round bottom flask was added 20nmol of sample F1 dissolved in hexane, 3mL of ODE, 3mL of oleylamine, and 3mL of oleic acid. The solution was degassed at r.t. for 1 hr. and then for 20 min at 80°C to remove the hexane and water. The solution was then stirred under N_2 and the temperature was raised to 310°C. At 200°C, a solution of Cd-oleate (1mL of a 0.2M solution of Cd-oleate in ODE) dissolved in ODE and a separate solution of octanethiol (42μL) dissolved in ODE (for a total volume of 6mL for each) were injected at a rate of 3mL/hr. The final solution was then cooled down and the nanorods were collected by precipitation using acetone followed by re-dispersion in hexane.

2. TEM Micrographs:

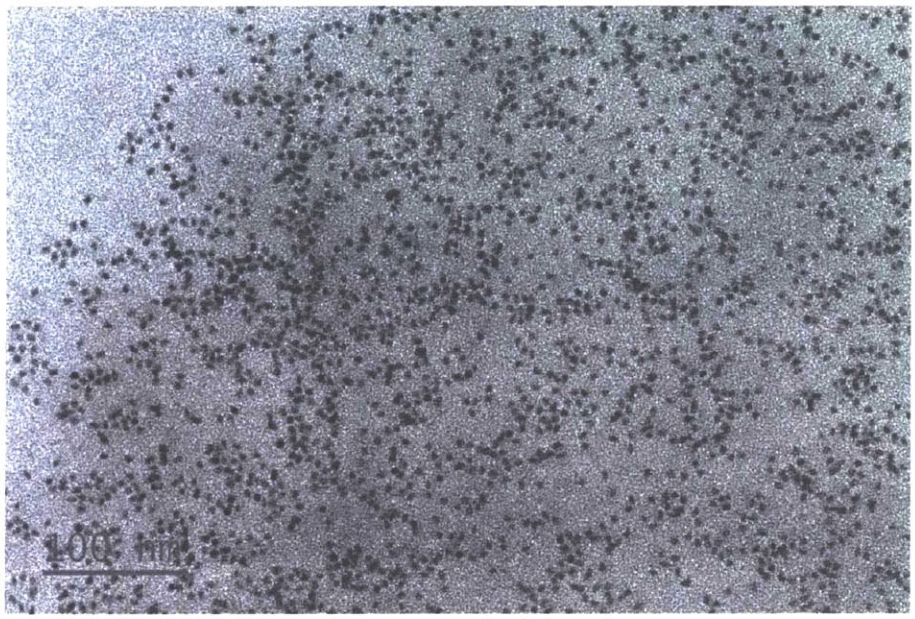

Figure S1: The TEM micrograph of the CdSe cores

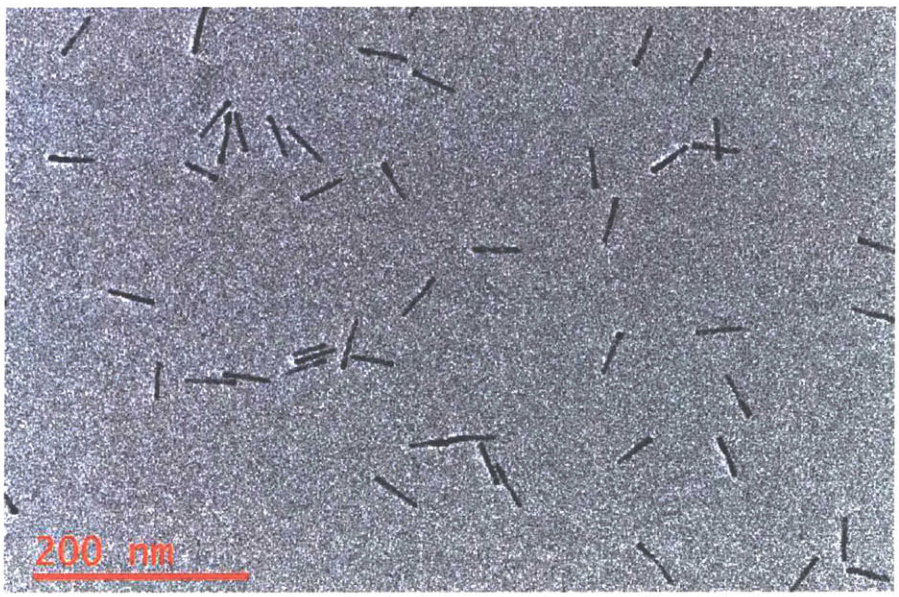

Figure S2: The TEM micrograph of the initial nanorod sample (F1)

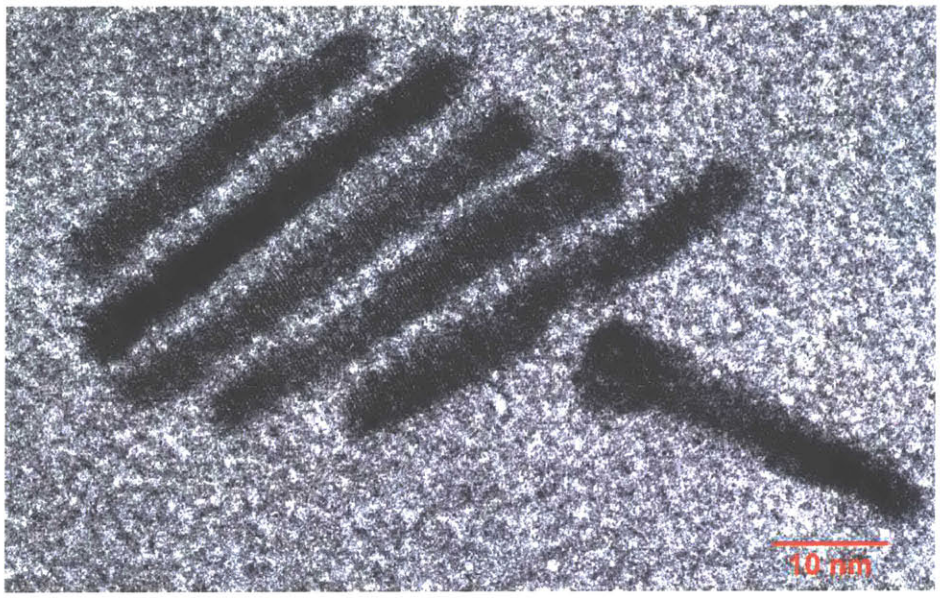

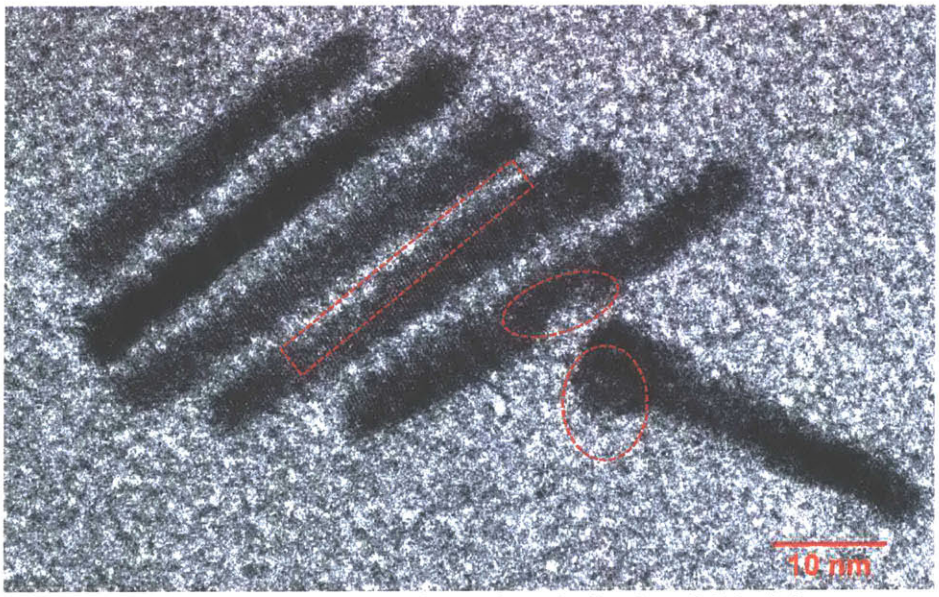

Figure S3: Higher magnification TEM of sample F1 indicating visible defects (dashed red outlines)

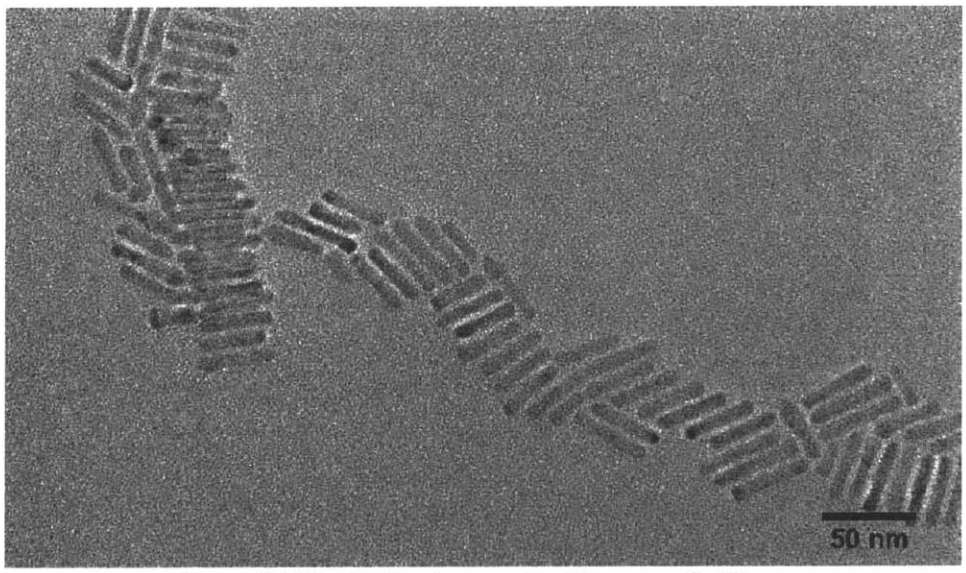

Figure S4: The TEM micrograph of the sample S1

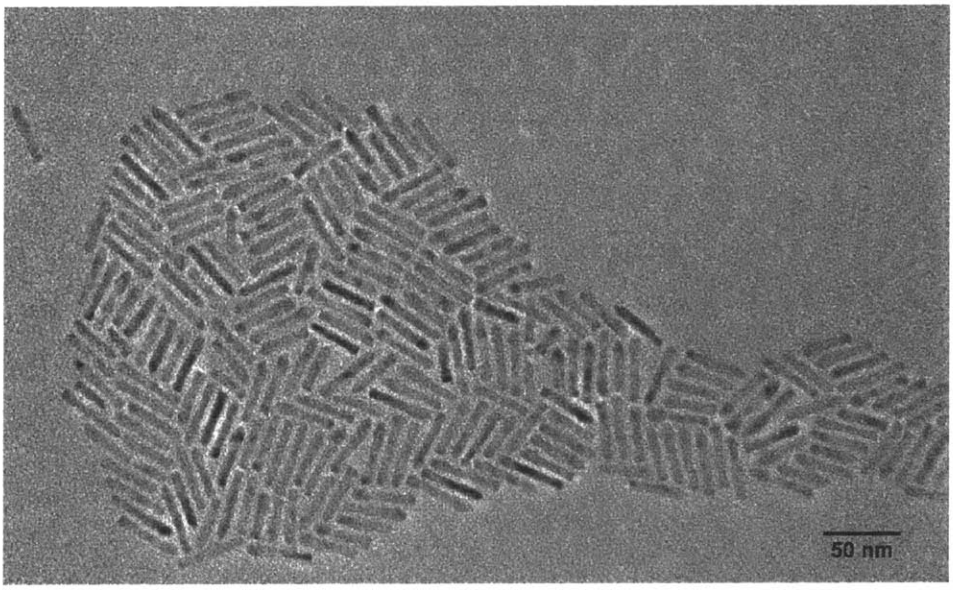

Figure S5: The TEM micrograph of the sample S2

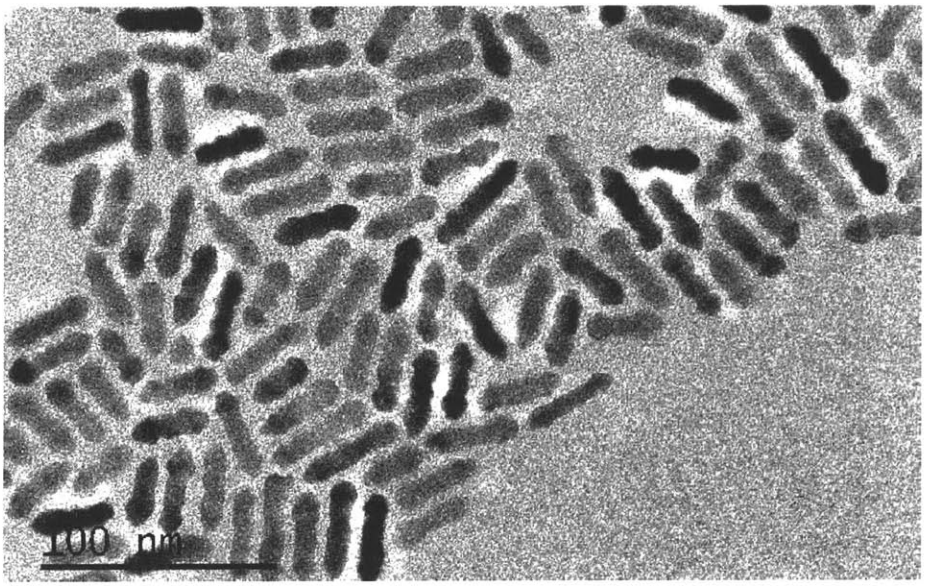

Figure S6: The TEM micrograph of the sample S3

3. Fluorescence spectra of CdSe/CdS quantum dot aliquots and small-core seeded CdSe/CdS nanorods

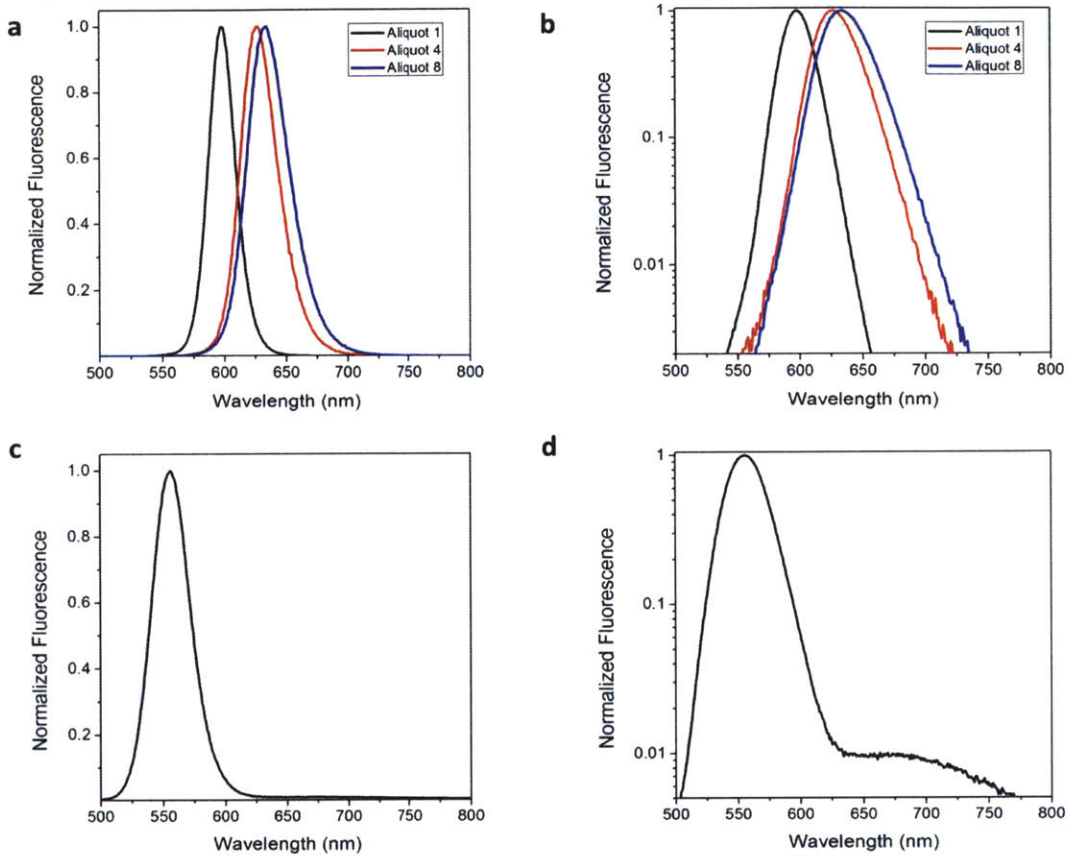

Figure S7: Fluorescence spectra of a series of CdSe/CdS quantum dots† on a) a linear and b) logarithmic (b) scale for different aliquots; Fluorescence spectra of CdSe/CdS nanorods‡ with a small (2.5nm) CdSe core on c) a linear and d) logarithmic scale

† The dots were created from a core with a first excitonic feature in the absorption spectrum at 543nm. Aliquots were taken each after uniform intervals of shell growth; aliquot 8 corresponded to a total shell thickness of ~14 monolayers. ‡ The nanorods had a total shell thickness of 30nm and were grown using similar conditions to the "fast growth" step used elsewhere in this publication

4. Additional Spectra

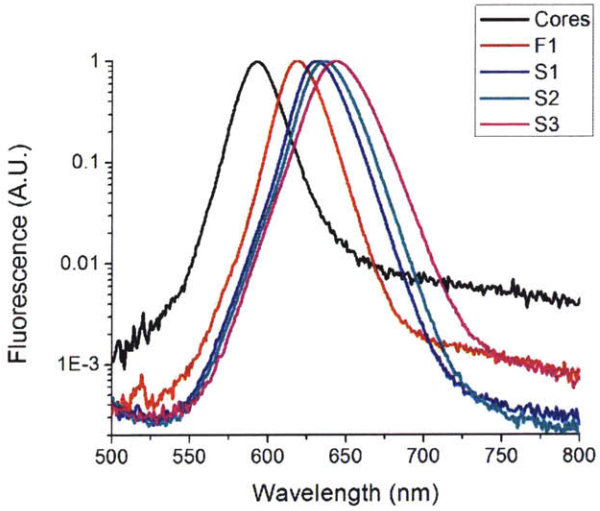

Figure S8: A reproduction of Fig. 2b with the y-axis lowered to include all the data

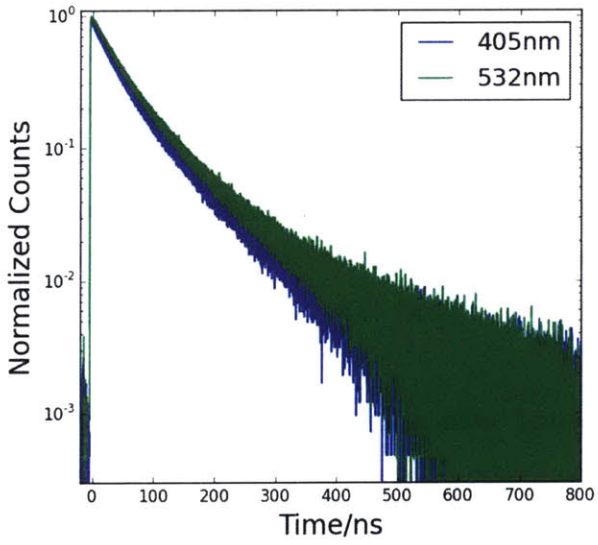

Figure S9: Comparison the PL decay of sample S3 with excitation at 405nm and 532nm

Ch. 2 References

1. Murray, C. B.; Norris, D. J.; Bawendi, M. G. Synthesis and Characterization of Nearly Monodisperse Cde (E = Sulfur, Selenium, Tellurium) Semiconductor Nanocrystallites. *J. Am. Chem. Soc.* **1993,** *115*, 8706-8715.

2. Efros, A. L.; Rosen, M.; Kuno, M.; Nirmal, M.; Norris, D. J.; Bawendi, M. Band-Edge Exciton in Quantum Dots of Semiconductors with a Degenerate Valence Band: Dark and Bright Exciton States. *Physical Review B* **1996,** *54*, 4843-4856.

3. Coe-Sullivan, S.; Woo, W.-K.; Steckel, J. S.; Bawendi, M.; Bulović, V. Tuning the Performance of Hybrid Organic/Inorganic Quantum Dot Light-Emitting Devices. *Organic Electronics* **2003,** *4*, 123-130.

4. Chen, O.; Zhao, J.; Chauhan, V. P.; Cui, J.; Wong, C.; Harris, D. K.; Wei, H.; Han, H. S.; Fukumura, D.; Jain, R. K.; Bawendi, M. G. Compact High-Quality Cdse-Cds Core-Shell Nanocrystals with Narrow Emission Linewidths and Suppressed Blinking. *Nat. Mater.* **2013,** *12*, 445-451.

5. Zhuang, Z.; Peng, Q.; Li, Y. Controlled Synthesis of Semiconductor Nanostructures in the Liquid Phase. *Chem. Soc. Rev.* **2011,** *40*, 5492.

6. Carbone, L.; Cozzoli, P. D. Colloidal Heterostructured Nanocrystals: Synthesis and Growth Mechanisms. *Nano Today* **2010,** *5*, 449-493.

7. Cui, J.; Beyler, A. P.; Coropceanu, I.; Cleary, L.; Avila, T. R.; Chen, Y.; Cordero, J. M.; Heathcote, S. L.; Harris, D. K.; Chen, O. Evolution of the Single-Nanocrystal Photoluminescence Linewidth with Size and Shell: Implications for Exciton–Phonon Coupling and the Optimization of Spectral Linewidths. *Nano Lett.* **2015,** *16*, 289-296.

8. Brovelli, S.; Schaller, R. D.; Crooker, S. A.; García-Santamaría, F.; Chen, Y.; Viswanatha, R.; Hollingsworth, J. A.; Htoon, H.; Klimov, V. I. Nano-Engineered Electron–Hole Exchange Interaction Controls Exciton Dynamics in Core–Shell Semiconductor Nanocrystals. *Nat. Commun.* **2011,** *2*, 280.

9. Cui, J.; Beyler, A. P.; Marshall, L. F.; Chen, O.; Harris, D. K.; Wanger, D. D.; Brokmann, X.; Bawendi, M. G. Direct Probe of Spectral Inhomogeneity

Reveals Synthetic Tunability of Single-Nanocrystal Spectral Linewidths. *Nature Chem.* **2013,** *5*, 602-606.

10. Coropceanu, I.; Bawendi, M. G. Core/Shell Quantum Dot Based Luminescent Solar Concentrators with Reduced Reabsorption and Enhanced Efficiency. *Nano Lett.* **2014,** *14*, 4097-4101.

11. Beyler, A. P.; Bischof, T. S.; Cui, J.; Coropceanu, I.; Harris, D. K.; Bawendi, M. G. Sample-Averaged Biexciton Quantum Yield Measured by Solution-Phase Photon Correlation. *Nano Lett.* **2014,** *14*, 6792-6798.

12. Qin, H.; Niu, Y.; Meng, R.; Lin, X.; Lai, R.; Fang, W.; Peng, X. Single-Dot Spectroscopy of Zinc-Blende Cdse/Cds Core/Shell Nanocrystals: Nonblinking and Correlation with Ensemble Measurements. *J. Am. Chem. Soc.* **2014,** *136*, 179-187.

13. Nasilowski, M.; Spinicelli, P.; Patriarche, G.; Dubertret, B. Gradient Cdse/Cds Quantum Dots with Room Temperature Biexciton Unity Quantum Yield. *Nano Lett.* **2015,** *15*, 3953-3958.

14. Mashford, B. S.; Stevenson, M.; Popovic, Z.; Hamilton, C.; Zhou, Z.; Breen, C.; Steckel, J.; Bulovic, V.; Bawendi, M.; Coe-Sullivan, S.; Kazlas, P. T. High-Efficiency Quantum-Dot Light-Emitting Devices with Enhanced Charge Injection. *Nat Photon* **2013,** *7*, 407-412.

15. Han, H.-S.; Niemeyer, E.; Huang, Y.; Kamoun, W. S.; Martin, J. D.; Bhaumik, J.; Chen, Y.; Roberge, S.; Cui, J.; Martin, M. R.; Fukumura, D.; Jain, R. K.; Bawendi, M. G.; Duda, D. G. Quantum Dot/Antibody Conjugates for in Vivo Cytometric Imaging in Mice. *Proceedings of the National Academy of Sciences* **2015,** *112*, 1350-1355.

16. Meinardi, F.; Colombo, A.; Velizhanin, K. A.; Simonutti, R.; Lorenzon, M.; Beverina, L.; Viswanatha, R.; Klimov, V. I.; Brovelli, S. Large-Area Luminescent Solar Concentrators Based on `Stokes-Shift-Engineered' Nanocrystals in a Mass-Polymerized Pmma Matrix. *Nat Photon* **2014,** *8*, 392-399.

17. Vaxenburg, R.; Rodina, A.; Lifshitz, E.; L. Efros, A. Biexciton Auger Recombination in Cdse/Cds Core/Shell Semiconductor Nanocrystals. *Nano Lett.* **2016,** *16*, 2503-2511.

18. Zhao, J.; Chen, O.; Strasfeld, D. B.; Bawendi, M. G. Biexciton Quantum Yield Heterogeneities in Single Cdse (Cds) Core (Shell) Nanocrystals and Its Correlation to Exciton Blinking. *Nano Lett.* **2012,** *12*, 4477-4483.

19. JavauxC; MahlerB; DubertretB; ShabaevA; Rodina, A. V.; EfrosAl, L.; Yakovlev, D. R.; LiuF; BayerM; CampsG; BiadalaL; BuilS; QuelinX; Hermier, J. P. Thermal Activation of Non-Radiative Auger Recombination in Charged Colloidal Nanocrystals. *Nat Nano* **2013,** *8*, 206-212.

20. Carbone, L.; Nobile, C.; De Giorgi, M.; Sala, F. D.; Morello, G.; Pompa, P.; Hytch, M.; Snoeck, E.; Fiore, A.; Franchini, I. R.; Nadasan, M.; Silvestre, A. F.; Chiodo, L.; Kudera, S.; Cingolani, R.; Krahne, R.; Manna, L. Synthesis and Micrometer-Scale Assembly of Colloidal Cdse/Cds Nanorods Prepared by a Seeded Growth Approach. *Nano Lett.* **2007,** *7*, 2942-2950.

21. Talapin, D. V.; Koeppe, R.; Gotzinger, S.; Kornowski, A.; Lupton, J. M.; Rogach, A. L.; Benson, O.; Feldmann, J.; Weller, H. Highly Emissive Colloidal Cdse/Cds Heterostructures of Mixed Dimensionality. *Nano Lett.* **2003,** *3*, 1677-1681.

22. Chauhan, V. P.; Popović, Z.; Chen, O.; Cui, J.; Fukumura, D.; Bawendi, M. G.; Jain, R. K. Fluorescent Nanorods and Nanospheres for Real-Time in Vivo Probing of Nanoparticle Shape-Dependent Tumor Penetration. *Angew. Chem., Int. Ed.* **2011,** *50*, 11417-11420.

23. Sitt, A.; Hadar, I.; Banin, U. Band-Gap Engineering, Optoelectronic Properties and Applications of Colloidal Heterostructured Semiconductor Nanorods. *Nano Today* **2013,** *8*, 494-513.

24. Bronstein, N. D.; Li, L.; Xu, L.; Yao, Y.; Ferry, V. E.; Alivisatos, A. P.; Nuzzo, R. G. Luminescent Solar Concentration with Semiconductor Nanorods and Transfer-Printed Micro-Silicon Solar Cells. *ACS Nano* **2014,** *8*, 44-53.

25. Bradshaw, L. R.; Knowles, K. E.; McDowall, S.; Gamelin, D. R. Nanocrystals for Luminescent Solar Concentrators. *Nano Lett.* **2015,** *15*, 1315-1323.

26. Castelli, A.; Meinardi, F.; Pasini, M.; Galeotti, F.; Pinchetti, V.; Lorenzon, M.; Manna, L.; Moreels, I.; Giovanella, U.; Brovelli, S. High-Efficiency All-Solution-Processed Light-Emitting Diodes Based on Anisotropic Colloidal Heterostructures with Polar Polymer Injecting Layers. *Nano Lett.* **2015,** *15*, 5455-5464.

27. Di Stasio, F.; Grim, J. Q.; Lesnyak, V.; Rastogi, P.; Manna, L.; Moreels, I.; Krahne, R. Single-Mode Lasing from Colloidal Water-Soluble Cdse/Cds Quantum Dot-in-Rods. *Small* **2015,** *11*, 1328-1334.

28. Pisanello, F.; Leménager, G.; Martiradonna, L.; Carbone, L.; Vezzoli, S.; Desfonds, P.; Cozzoli, P. D.; Hermier, J.-P.; Giacobino, E.; Cingolani, R.; De Vittorio, M.; Bramati, A. Non-Blinking Single-Photon Generation with Anisotropic Colloidal Nanocrystals: Towards Room-Temperature, Efficient, Colloidal Quantum Sources. *Adv. Mater.* **2013,** *25*, 1974-1980.

29. Christodoulou, S.; Vaccaro, G.; Pinchetti, V.; De Donato, F.; Grim, J. Q.; Casu, A.; Genovese, A.; Vicidomini, G.; Diaspro, A.; Brovelli, S.; Manna, L.; Moreels, I. Synthesis of Highly Luminescent Wurtzite Cdse/Cds Giant-Shell Nanocrystals Using a Fast Continuous Injection Route. *J. Mater. Chem. C* **2014,** *2*, 3439-3447.

30. Kambhampati, P. On the Kinetics and Thermodynamics of Excitons at the Surface of Semiconductor Nanocrystals: Are There Surface Excitons? *Chem. Phys.* **2015,** *446*, 92-107.

31. Wu, K.; Hill, L. J.; Chen, J.; McBride, J. R.; Pavlopolous, N. G.; Richey, N. E.; Pyun, J.; Lian, T. Universal Length Dependence of Rod-to-Seed Exciton Localization Efficiency in Type I and Quasi-Type Ii Cdse@Cds Nanorods. *ACS Nano* **2015,** *9* 4591–4599.

32. She, C.; Demortière, A.; Shevchenko, E. V.; Pelton, M. Using Shape to Control Photoluminescence from Cdse/Cds Core/Shell Nanorods. *The Journal of Physical Chemistry Letters* **2011,** *2*, 1469-1475.

33. Shabaev, A.; Efros, A. L. 1d Exciton Spectroscopy of Semiconductor Nanorods. *Nano Lett.* **2004,** *4*, 1821-1825.

CHAPTER 3

The Development of New Active Materials for Luminescent Solar Concentrators (LSCs)

3.1 Introduction

Luminescent solar concentrators (LSCs) have received renewed attention in recent years as a platform for solar energy harvesting complementary to conventional photovoltaic technologies.[1-3] The key requisite properties for the active materials in LSCs are low reabsorption (i.e. minimal spectral overlap between the absorption and emission spectra) and a high fluorescence quantum efficiency.[4-6] In this chapter we will discuss the development of CdSe/CdS quantum dots and nanorods that simultaneously fulfill these two requirements as well as the optical characterization of the LSC prototypes fabricated using these materials.

3.2 The Use of Thick-Shelled CdSe/CdS Quantum Dots as the Active Material in Luminescent Solar Concentrators

Inorganic core/shell quantum dots (QDs) are especially well suited to address the problem of reabsorption since they allow for a spectral separation of the absorption and emission by confining the two processes to different parts of the heterostructure.[7] The basic operational principle as illustrated in Fig. 3-1 begins with absorption (I), which for high photon energies will occur into states predominantly located in the shell. Absorption is then followed by rapid energy

relaxation to the band-edge states (II), which are confined within or near the core, where the exciton can finally recombine radiatively (III). This scheme allows for a straightforward reduction of the reabsorption by simply maximizing the volumetric ratio of the shell to the core.

Unfortunately in many systems, such as in the case of CdSe/CdS nanostructures, a pronounced tradeoff exists between the shell thickness and the quantum yield, which has been attributed to a reduction in the spatial overlap of the hole and electron wavefunctions due to the quasi-type II band alignment of the CdSe/CdS system.[8-10] Recent progress in synthetic methods has resulted in near unity efficiencies for thin-shelled CdSe/CdS QDs.[11] Such a high quantum yield indicates a major reduction in the non-radiative decay channels and suggests the possibility of maintaining a high quantum yield even in thick-shelled

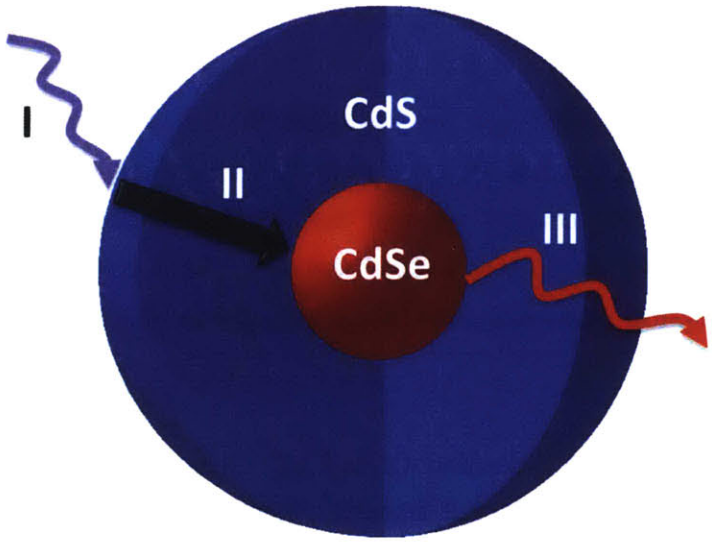

Figure 3-1: Use of CdSe/CdS quantum dots as a host/guest system. The key optical properties start with I) absorption by the shell material (the antenna), II) energy transfer to the core (the guest) and III) radiative recombination from the core

dots. In order to test this prediction, we have developed a synthetic method that

is inspired by Ref. 11 that retains a high quantum yield even as the shell thickness increases.[12] We prepared a series of core-shell QDs from the same CdSe cores but having variable shell thicknesses, with the volume of the shell varying up to a factor of 16 (calculated from the amount of precursors injected), with the thickest dots having a thickness of 5.0nm (approximately 14 monolayers) of CdS as determined from TEM[13]. We characterized this series of QDs and used the thickest ones to construct prototype LSCs. Finally we compared our results to a Monte Carlo simulation to identify the major loss channels.

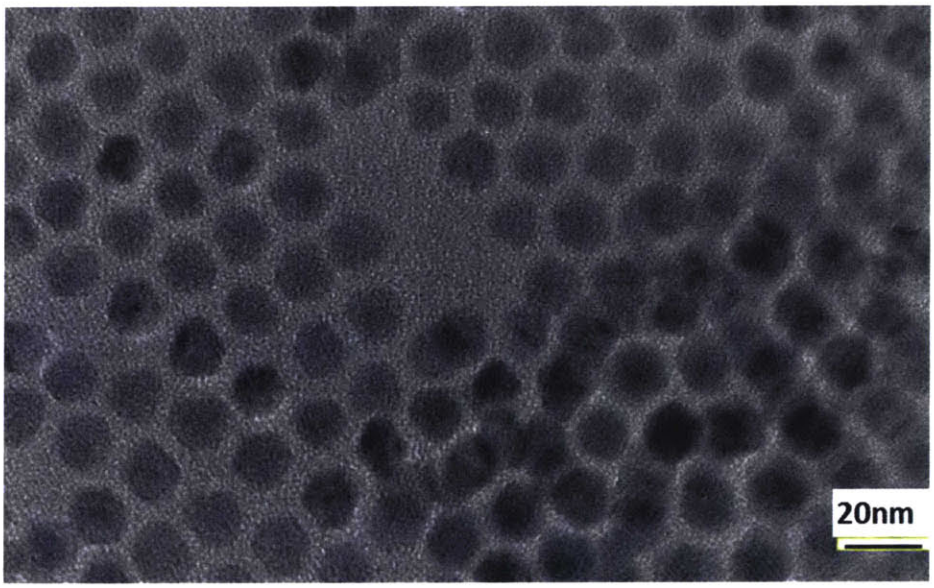

Figure 3-2: TEM micrograph of the CdSe/CdS quantum dots used for the LSCs

3.2.1 The Reduction of Reabsorption Using CdSe/CdS as a Host/Guest System

The absorption spectra of the QDs (normalized at 450nm) as a function of shell thickness are plotted in Fig. 3-3. The spectral region at wavelengths below 500nm is dominated by absorption into the CdS shell and its shape is largely insensitive to the shell thickness. In contrast, a significant change is seen in the relative intensity of the first excitonic feature (shown in the inset of Fig 3-3), corresponding to absorption by the CdSe core. Because this first excitonic peak is responsible for virtually all spectral overlap with the fluorescence spectrum, a relative reduction in this absorption feature directly results in a decrease of the

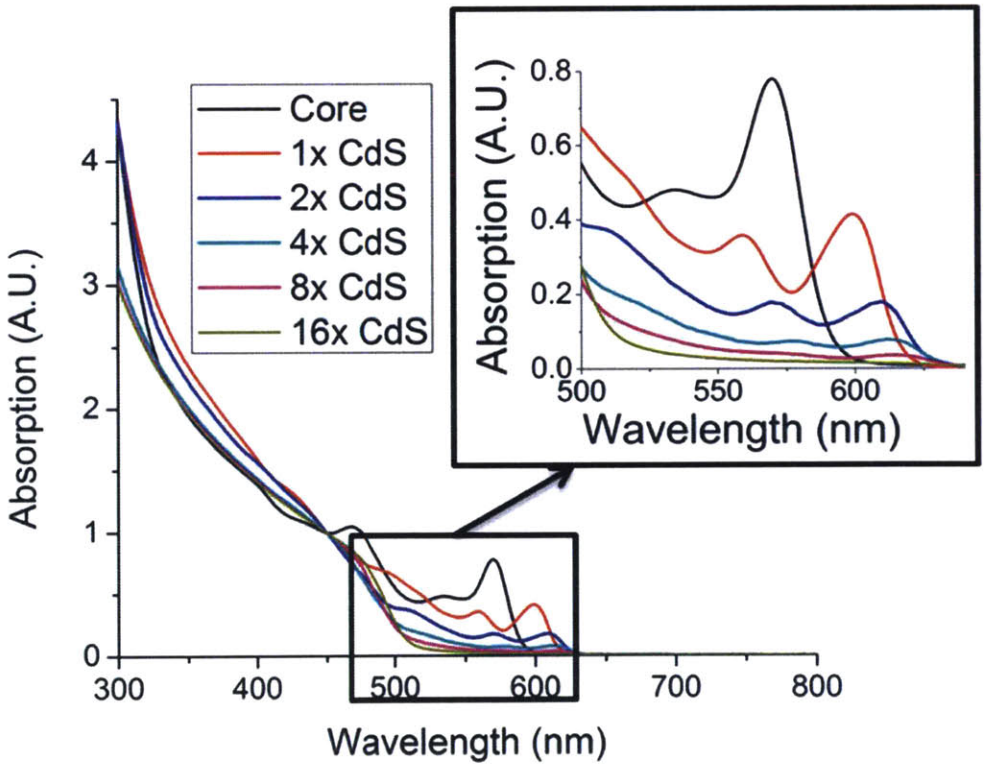

Figure 3-3: Evolution of the absorption spectra as a function of the shell volume (x refers to the volumetric ratio of the shell material relative to the thinnest shell studied)

reabsorption.

We quantify the reabsorption by a parameter S, which we define as the inverse of the area of spectral overlap between the normalized absorption and emission spectra as shown in Fig 3-5[14]. This parameter decreases nearly linearly as a function of shell thickness (see Fig 3-6), resulting in a 45-fold reduction in the reabsorption in the thickest-shelled dots compared to the original CdSe cores. The absorption and fluorescence spectra of the thickest shelled quantum dots are shown in Figure 3-4, on a linear and log scale. The absorption near the emission maximum is nearly two orders of magnitude smaller than that in the region where CdS absorbs (<500nm). Such an effective reduction in reabsorption is comparable to the best organic systems reported to date.[4] Moreover, even the sample with the thickest shell retained a high fluorescence quantum yield, with a value of 86% measured in solution.

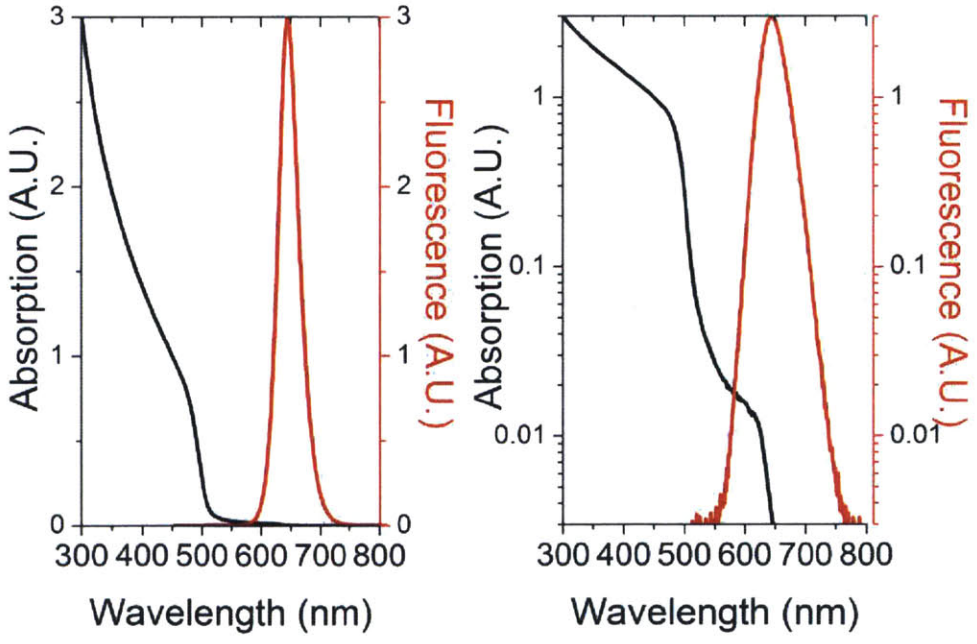

Figure 3-4: Optical spectra of the thick-shelled CdSe/CdS quantum dots on a linear scale (left) and a logarithimic scale (right)

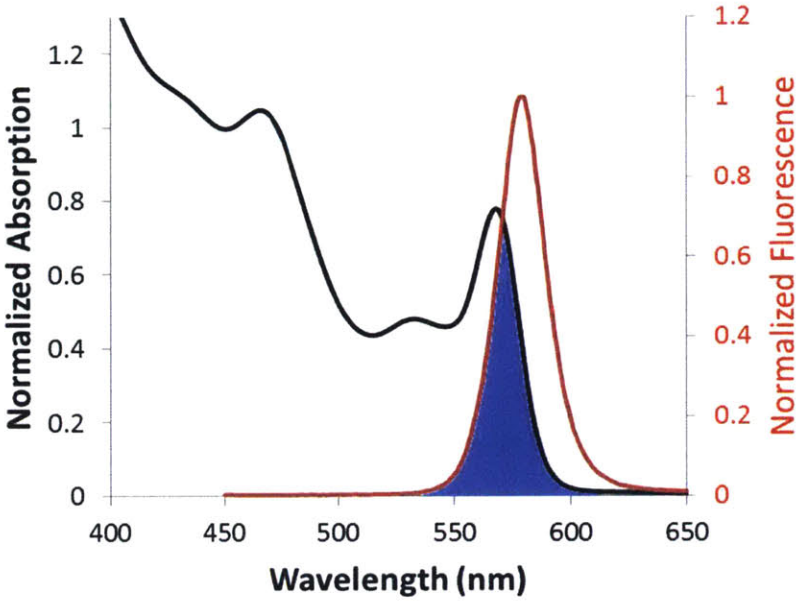

Figure 3-5: Definition of the reabsorption figure of merit S

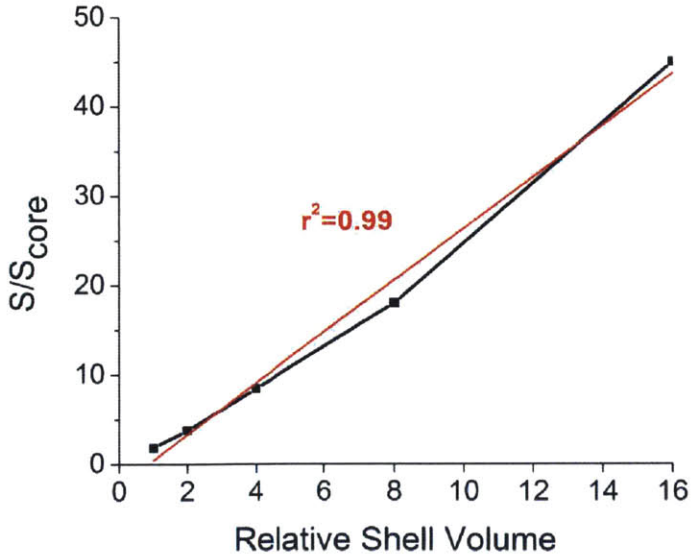

Figure 3-6: Reduction of reabsorption as a function of the shell thickness

3.2.2 Embedding Quantum Dots in an Optically Transparent Polymer Composite

In order to assess the performance of these QDs for LSC applications, prototype devices were prepared by embedding the quantum dots in a polymer matrix by adapting a previously reported procedure.[15] Briefly, quantum dots were dissolved in a mixture of monomeric precursor (lauryl methacrylate) and a crosslinker (ethylene glycol dimethacrylate) at a mass loading of approximately 20%, and the resulting solution was exposed to UV irradiation in the presence of a UV initiator (Diphenyl(2,4,6-trimethylbenzoyl)phosphine oxide) inside a mold consisting of two glass slides separated by a silicone spacer. The schematic of the cuvette used and a picture of an actual composite undergoing crosslinking is shown in Fig. 3-7 below.

The final devices measured 2 cm x 1.5 cm x 0.2 cm, yielding a geometric gain (the surface area of the top face divided by the surface area of the edges) of approximately 3. The resulting composites exhibited high optical quality, most

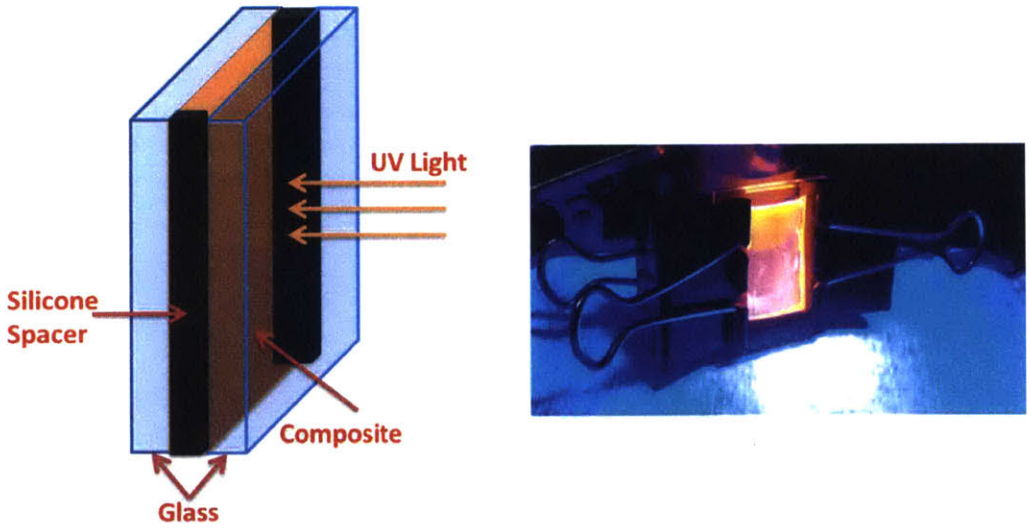

Figure 3-7: General schematic of the cuvette used to fabricate the composites (left) and the cuvette in use (right)

importantly as indicated by the lack of measureable scattering in the transparent window of the quantum dots (ca. 700-800nm) as shown in Figure 3-8. The reflectance in the transparent window was measured to be 8%, consistent with the theoretical Fresnel reflectance coefficient assuming a refractive index of 1.5 for the polymeric matrix.

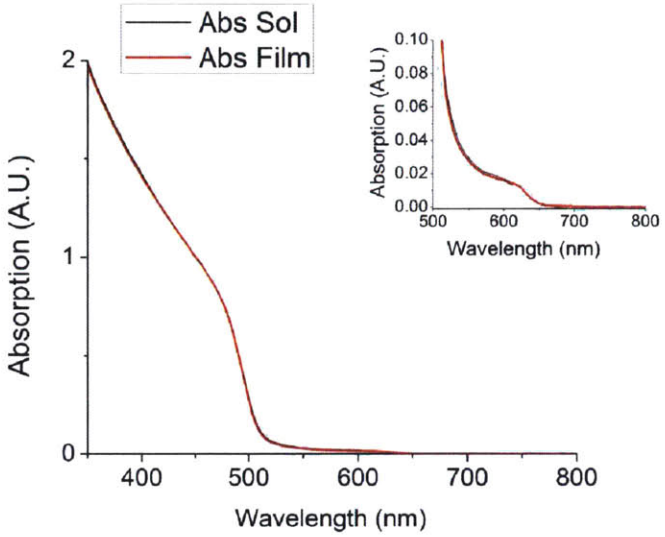

Figure 3-8: Absorption spectrum of the CdSe/CdS dots in solution and in the PLMA matrix; inset: a close-up of the spectral region from 500-800nm

3.2.3 Measuring the Optical Performance of the LSC Prototypes

The LSC performance was then measured using an integrating sphere using a process schematically illustrated in Fig 2d. First, the external quantum efficiency (EQE, here defined as the number of photons emitted divided by the total number of incident photons) was measured as shown in Figure 3-9. Excellent agreement was found between the EQE spectrum and the absorbance of the composite, indicating minimal energy dependence of the fluorescence quantum yield, in turn suggesting effectively complete energy transfer from the shell to the core. Black carbon paint was used to cover the edges of the device such that light could only be emitted from the faces of the device, and the EQE was then measured again as previously. By subtracting this measurement from the EQE of the original device, the optical efficiency was obtained, defined here as the fraction of the EQE due to emission from the edges alone[16]. The optical efficiency was found to be as high as 48% at 400 nm, a value unprecedented for

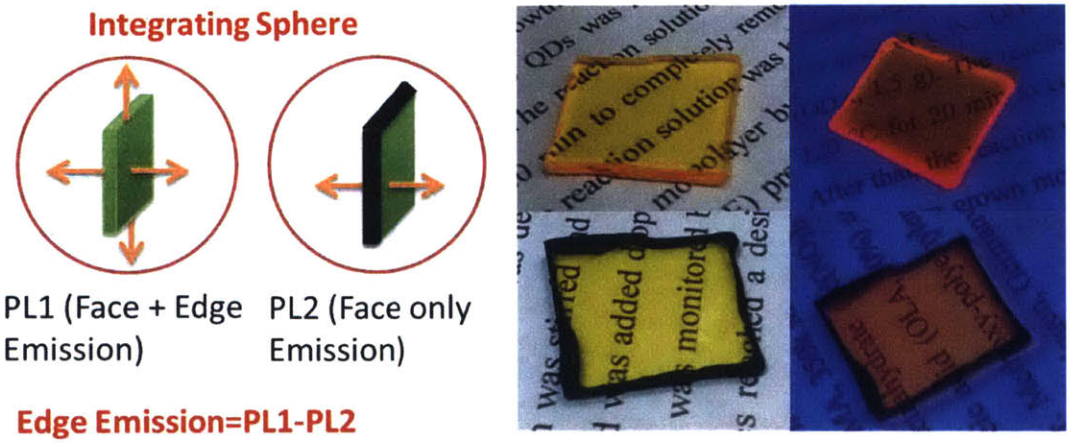

Figure 3-9: The LSC prototype and the set-up for the optical measurements; Left panel: basic scheme for optical efficiency measurements; Right panel: QD/polymer composites in ambient light (left) and under UV illumination (right) with the edges clear (top) and blocked by carbon paint (bottom)

quantum dot based luminescent solar concentrators and similar to the highest

efficiencies reported for low-reabsorption organic systems. At longer wavelengths, the optical efficiency decreases, but as can readily be seen from the excellent overlap of the EQE and the absorbance spectra, this decrease simply reflects the fact that the concentrator absorbs monotonically less light at lower energies. In fact, because of the complete energy transfer from the shell to the core, the entire optical efficiency spectrum can adequately be generated by simply multiplying the optical efficiency at a fixed wavelength by the normalized absorbance spectrum of the LSC. Moreover, this measurement was obtained using an extremely simple homogenous composite unlike previous state of the art devices employing high refractive index substrates and anti-reflection coatings to reduce optical losses.

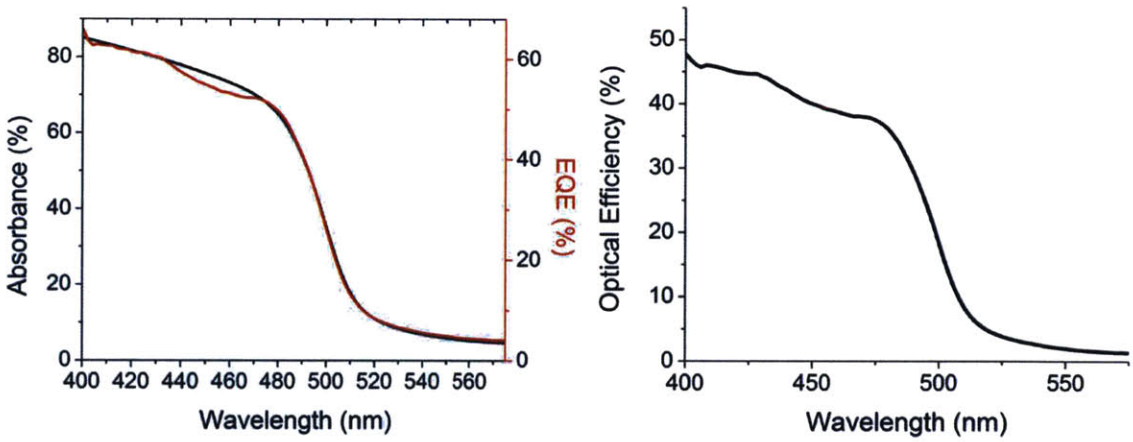

Figure 3-10: EQE spectra of the LSC prototype (left) and optical efficiency of the LSC (right)

3.2.4 The Implementation of a Monte Carlo Simulation for Modeling Photon Transport in Luminescent Solar Concentrators

A Monte Carlo simulation was developed to model the operation of luminescent solar concentrators by adapting and implementing a previously published protocol.[17] The general scheme of the LSC simulation is summarized graphically in Fig. 3-11 below. The first step of the simulation was to release a photon with a specified wavelength onto the top of the LSC and determine if the photon was reflected at the air/polymer interface by calculating the reflectance of the interface assuming a refractive index of 1.5 for the polymer/QD composite. Next it was calculated if the photon was absorbed by simulating the propagation length (based on the optical density of the LSC at the wavelength of the incident photon) and comparing this quantity to the height of the LSC. Next it was

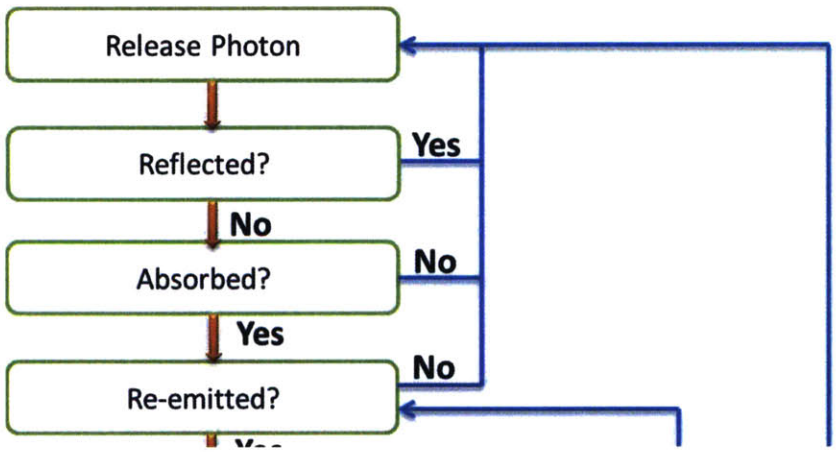

Figure 3-11: Schematic of the Monte Carlo Simulation for Photon Transport in the Luminescent Solar Concentrator

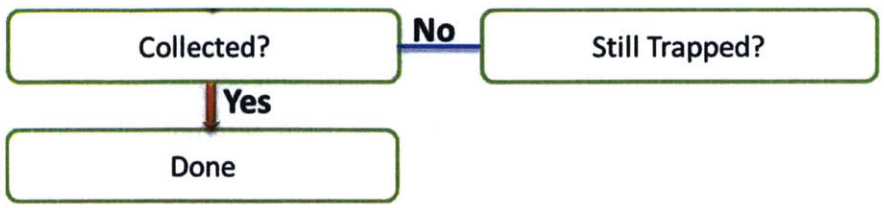

verified if the photon was re-emitted (based on the fluorescence quantum yield of individual quantum dots in the composite, which was calculated as described in the next section) and if so the wavelength was updated by sampling the emission spectrum, a propagation length was calculated, and the photon was given a random (isotropically distributed) direction. This process was repeated while the photon was in the interior of the concentrator and until the photon was reabsorbed (when it moved by a distance equal to the current propagation length), lost, or collected. If a photon was reabsorbed, the simulation resumed from the step immediately following absorption. If the photon reached a face of the LSC, the probability of reflection was calculated from the unpolarized Fresnel reflection coefficients to determine if the photon was reflected back into the concentrator or lost. Finally if a photon reached any of the four lateral edges it was considered collected. The above process was repeated until 100,000 photons were collected.

As inputs the simulation used the experimental optical spectra, the fluorescence quantum yield of the composites (see below), and the Fresnel reflection coefficients calculated for a medium with a refractive index of 1.5 and a cladding of 1.0. The fate of all incident photons was then calculated for an LSC having the same dimensions as the prototypes and using the measured optical spectra. The result is shown in Figure 3-12, for incident photons with a fixed wavelength of 400nm. The optical efficiency predicted (49%) matches the experimental result (48%). The loss channels can be divided into absorption and operational (post-absorption) losses. The former account for incomplete absorption of the light due to reflection and partial transmittance and together amount to ca. 18% of all incident photons (denoted "Reflected" and "Not Absorbed" in Fig. 3d). The operational losses in turn are due to the non-unity fluorescence quantum yield and non-unity trapping efficiency (the fraction of photons re-emitted in the LSC trapped via total internal reflection), denoted "Not Emitted" and "Lost Top" respectively in Fig 3d. The EQE spectrum yields a

fluorescence quantum yield of 82% (see SI), indicating that the high quantum yield observed in solution (86%) is retained upon embedding the quantum dots in the polymer matrix. The trapping efficiency can be estimated by dividing the optical efficiency by the total EQE, giving a value of ca. 73%, consistent with the theoretical value of 75% calculated for an isotropic emitter in a dielectric medium with a refractive index of 1.5.

They key sources of uncertainty stem from the parameters that enter into the model, namely the measured optical spectra, the estimation of the refractive index and the resulting reflection coefficient, and the measurement and calculation of the fluorescence quantum yield. Among these sources of error, the extraction of the fluorescence quantum yield from the EQE is probably responsible for the greatest portion of the uncertainty. While it is difficult to estimate the exact uncertainty of these measurements, the fact that the EQE spectrum was observed not to vary by more than about 3% over multiple runs as well as the similarity of the quantum yield measured in solution and in film using two different methods (giving 86% and 82% respectively) suggests an upper limit of the relative uncertainty of the simulation of less than 5%.

The absorption losses can in principle be diminished by increasing the optical density of the LSC and through the use of anti-reflective coatings. However, it is the operational losses that ultimately set the limit to the performance of LSCs, since these losses occur not only upon the initial absorption of the incident photon, but upon every reabsorption event as well. This effect can be expressed mathematically using an approximate expression for the optical efficiency: $\eta(\lambda) \sim A(\eta_{Pl}\eta_{tr})^{n+1}$, where A is the fraction of photons absorbed, η_{Pl} and η_{tr} are the photoluminescence and trapping efficiencies respectively, and n is the number of reabsorption events.[5] Because of the low reabsorption of our quantum dots, in the LSCs fabricated only approximately 3% of the photons lost had been reabsorbed according to the simulation, indicating that the vast majority of photons propagated freely through the waveguide after being emitted.

While the geometric gain of the prototype devices is small, this low degree of reabsorption makes possible the retention of a high efficiency even at much higher geometric gains, which in turn makes possible the concentration of significantly more light. For example, our modeling suggests that even at a geometric gain of 200, the collection efficiency at 400 nm can be as high as 20%, yielding a 40-fold concentration of the incident light.

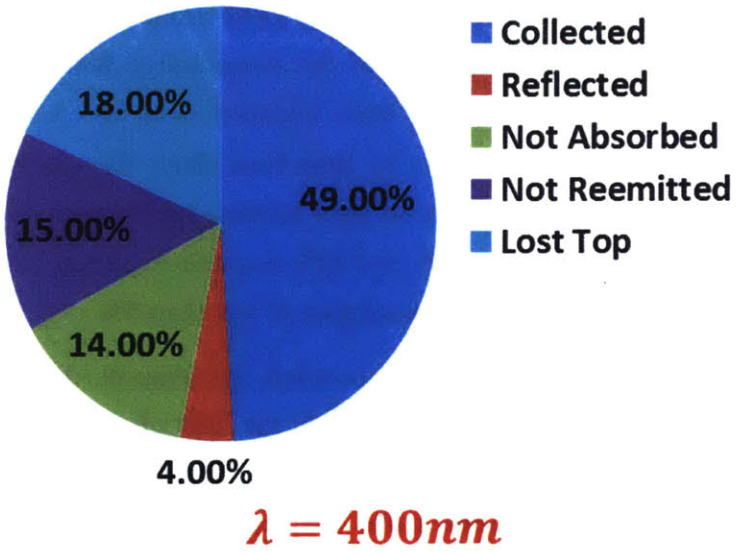

Figure 3-12: Distribution of outcomes for photons incident on the LSC from the Monte Carlo simulation

3.2.5 Determination of Fluorescence Quantum Yield of Quantum Dots in Polymer Composites

The fluorescence quantum yield of the individual quantum dots embedded in the polymer matrix was determined by fitting the external quantum efficiency with the Monte Carlo simulation developed using the quantum yield as the only free parameter, yielding a quantum yield of 82%. The corrections carried out to the EQE to extract the fluorescence quantum yield can be rationalized in terms of specific optical losses. For example, at 400nm, the EQE was measured to be 66%. Correcting for partial reflection (4%) and incomplete absorbance (85%), yields a quantum yield of 81%. There is a further 1% correction due to reabsorption of photons, giving the final value of 82%.

3.2.6 Conclusions

In conclusion, we have optimized CdSe/CdS core-shell quantum dots for LSC applications to exhibit an unprecedented combination of minimal reabsorption and a high fluorescence quantum yield. The optical properties of the materials developed can be retained upon incorporation into polymer composites, providing a practical route for the fabrication of simple concentrators, the optical performance of which is in full agreement with theoretical predictions. While we were finalizing this publication, it came to our attention that another group has pursued a similar approach of using thick shelled CdSe/CdS quantum dots to fabricate LSCs with low reabsorption.[18] The key difference between our result and this work is that while the former used quantum dots synthesized using an older method and had a fluorescence quantum yield a bit over 40%, our devices incorporate a new generation of quantum dots, with a quantum yield that is almost doubled relative to the older method, which in turn allows for a much higher optical efficiency than had previously been attainable. The high optical efficiency of these concentrators, combined with their high degree of transparency in a large part of the visible spectrum makes them well-suited for applications such as energy harvesting window coatings or to serve as the first layer in tandem LSCs. As a standalone solar concentrator, the ultimate limitation of the system is the large band gap of the shell material (CdS), due to its poor match to the solar spectrum. Ultimately the key to significantly advancing the performance of inorganic nanostructures in the context of LSC applications is the transition to lower band-gap materials, which in turn may be optimized using the same scheme described in this paper.

3.2.7 Methods:

The CdSe/CdS quantum dots were synthesized by first preparing the CdSe cores using a previously published protocol[19] and then carrying out a slow high temperature CdS shell growth by modifying the procedure described in Ref. 8 as described in detail in Ch II. Absorption spectra were recorded using a Cary 5000 spectrophotometer and emission spectra were recorded using a Fluoromax-3 spectrofluorometer. Solution phase quantum yields were calculated using the relative fluorescence method by using Rhodamine 101 as the reference dye. TEM micrographs were recorded using a JEOL 2010 TEM. LSC measurements were taken using a Labsphere integrating sphere using a tungsten lamp as the source, chopping the beam at 300 Hz and collecting the output using a calibrated silicon detector through a Stanford Research Systems lock-in amplifying system.

3.3 Reducing Top Escape Losses in Luminescent Solar Concentrators by Aligning CdSe/CdS Nanorods

With the onset of synthetic methods for the production of inorganic nanorods, significant effort has been devoted to the development of methods to align these rods in order to fully exploit the new properties emerging from their anisotropy, such as their linearly polarized luminescence. One of the earliest such approaches was based on the spontaneous self-assembly of these structures, a process that in the case of CdSe/CdS nanorods showed the possibility of creating both horizontally aligned ribbons on a substrate, as well as well-ordered vertically aligned monolayers.[19, 20] Furthermore, by slowing down the evaporation of the solvent to the order of days, the creation of vertically aligned films was even shown to be possible over cm-sized areas.[21]

In order to gain more control over the self-assembly process, we adopted a thermal-processing method previously reported for CdSe nanorods[26] for the alignment of CdSe/CdS nanorods. Briefly, CdSe/CdS nanorods were added to a poor solvent (butyl acetate), the solution was heated to 100°C and was then slowly cooled to room temperature. As a result, highly order micrometer sized platelets consisting of a close packed vertical array of nanorods was obtained as shown in Fig. 11. For CdSe, such platelets have been demonstrated to act as building blocks for the formation of vertically aligned films after drop-casting, in a process occurring in a few minutes.[26] While this approach resulted in the reproducible alignment of various batches of nanorods over micrometer-sized areas, it proved difficult to create films that were sufficiently thick and optically clear to be directly used in luminescent solar concentrators. More recent work in our group is focused on combining this alignment scheme with a polymer scaffold in order to create uniform composites with a high degree of alignment preferentially in a direction normal to the surface of the substrate.

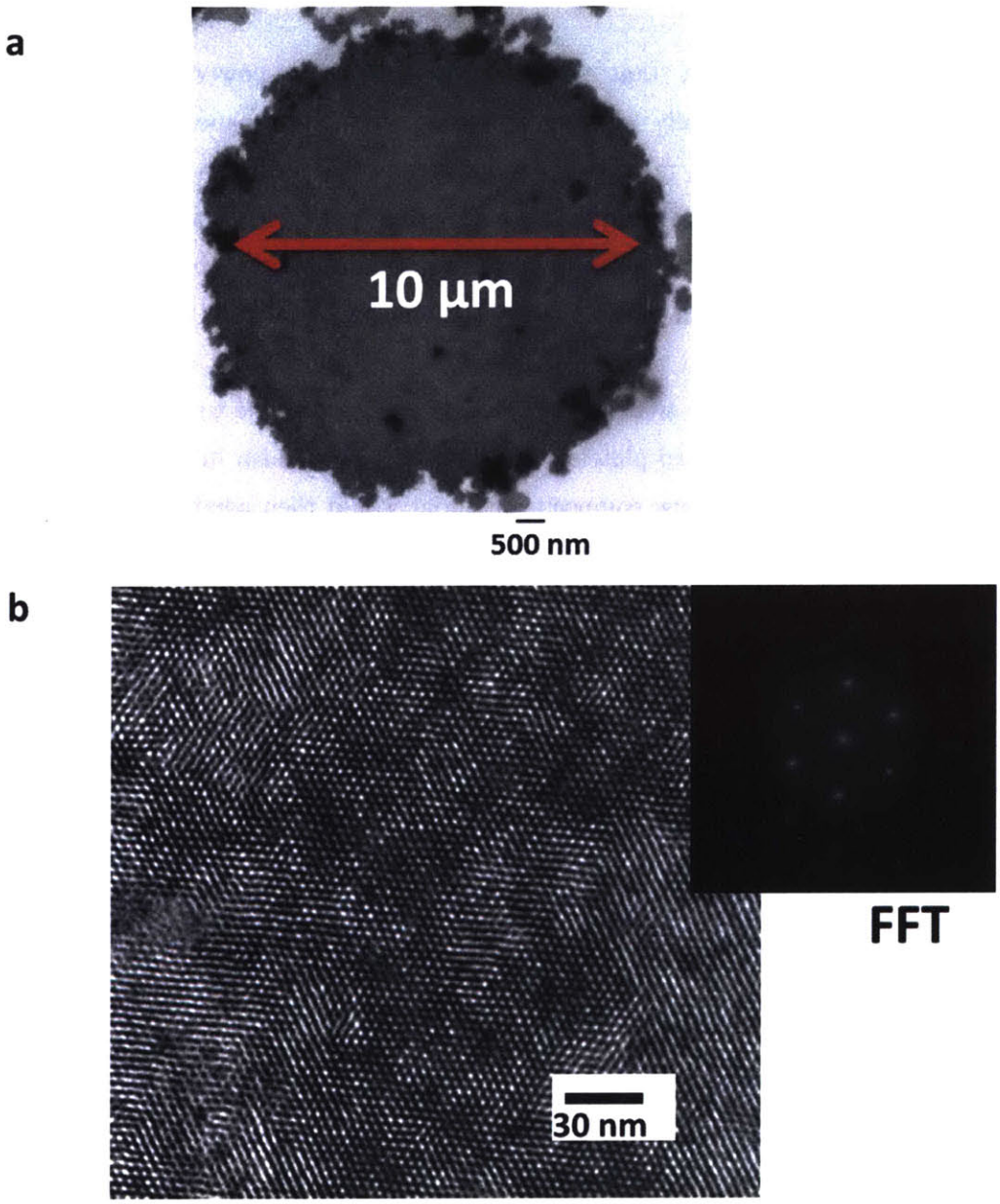

Figure 3-13: The vertically aligned packed CdSe/CdS; a) optical image; b) TEM micrograph with the inset showing the Fast Fourier Transform (FFT)

3.3.1 Conclusions

We have shown that self-assembly can be a powerful tool for the development of vertically aligned arrays of CdSe/CdS nanorods. Through a simple thermal process, micrometer-sized platelets of vertically aligned nanorods can be fabricated. While in principle such platelets can serve as building blocks for the fabrication of thick functional films, this approach appears difficult to realize using a neat film of nanorods. In particular, scattering in such films can be a significant issue, which can preclude the fabrication of efficient solar concentrators. We hope that in the future it will be possible to use self-assembly to first form these aligned platelets and to then embed them in an optically clear polymer matrix. This new composite material would then combine the advances of the prototype LSCs we discussed in section 3-2, with the reduced reabsorption made possible by aligning the nanorods.

Ch. 3 References

1. Debije, M. G.; Verbunt, P. P. C. Thirty Years of Luminescent Solar Concentrator Research: Solar Energy for the Built Environment. *Adv. Energy Mater.* **2012**, *2*, 12-35.

2. Yoon, J.; Li, L.; Semichaevsky, A. V.; Ryu, J. H.; Johnson, H. T.; Nuzzo, R. G.; Rogers, J. A. Flexible Concentrator Photovoltaics Based on Microscale Silicon Solar Cells Embedded in Luminescent Waveguides. *Nat. Commun.* **2011**, *2*, 343.

3. van Sark, W.; Barnham, K. W. J.; Slooff, L. H.; Chatten, A. J.; Buchtemann, A.; Meyer, A.; McCormack, S. J.; Koole, R.; Farrell, D. J.; Bose, R.; Bende, E. E.; Burgers, A. R.; Budel, T.; Quilitz, J.; Kennedy, M.; Meyer, T.; Donega, C. D. M.; Meijerink, A.; Vanmaekelbergh, D. Luminescent Solar Concentrators - a Review of Recent Results. *Opt. Express* **2008**, *16*, 21773-21792.

4. Currie, M. J.; Mapel, J. K.; Heidel, T. D.; Goffri, S.; Baldo, M. A. High-Efficiency Organic Solar Concentrators for Photovoltaics. *Science* **2008**, *321*, 226-228.

5. Mulder, C. L.; Reusswig, P. D.; Velazquez, A. M.; Kim, H.; Rotschild, C.; Baldo, M. A. Dye Alignment in Luminescent Solar Concentrators: I. Vertical Alignment for Improved Waveguide Coupling. *Opt. Express* **2010**, *18*, A79-A90.

6. Sholin, V.; Olson, J. D.; Carter, S. A. Semiconducting Polymers and Quantum Dots in Luminescent Solar Concentrators for Solar Energy Harvesting. *J. Appl. Phys.* **2007**, *101*, 123114.

7. Purcell-Milton, F.; Gun'ko, Y. K. Quantum Dots for Luminescent Solar Concentrators. *J. Mater. Chem.* **2012**, *22*, 16687.

8. Ghosh, Y.; Mangum, B. D.; Casson, J. L.; Williams, D. J.; Htoon, H.; Hollingsworth, J. A. New Insights into the Complexities of Shell Growth and the Strong Influence of Particle Volume in Nonblinking "Giant" Core/Shell Nanocrystal Quantum Dots. *J. Am. Chem. Soc.* **2012,** *134*, 9634-9643.

9. Brovelli, S.; Schaller, R. D.; Crooker, S. A.; García-Santamaría, F.; Chen, Y.; Viswanatha, R.; Hollingsworth, J. A.; Htoon, H.; Klimov, V. I. Nano-Engineered Electron–Hole Exchange Interaction Controls Exciton Dynamics in Core–Shell Semiconductor Nanocrystals. *Nat. Commun.* **2011,** *2*, 280.

10. Bronstein, N. D.; Li, L.; Xu, L.; Yao, Y.; Ferry, V. E.; Alivisatos, A. P.; Nuzzo, R. G. Luminescent Solar Concentration with Semiconductor Nanorods and Transfer-Printed Micro-Silicon Solar Cells. *ACS Nano* **2013,** *8*, 44-53.

11. Chen, O.; Zhao, J.; Chauhan, V. P.; Cui, J.; Wong, C.; Harris, D. K.; Wei, H.; Han, H. S.; Fukumura, D.; Jain, R. K.; Bawendi, M. G. Compact High-Quality Cdse-Cds Core-Shell Nanocrystals with Narrow Emission Linewidths and Suppressed Blinking. *Nat. Mater.* **2013,** *12*, 445-451.

12. During the review process of this publication, we became aware of a different recent synthetic approach that produced thick-shelled CdSe/CdS quantum dots with a high quantum yield: Christodoulou, S.; Vaccaro, G.; Pinchetti, V.; De Donato, F.; Grim, J. Q.; Casu, A.; Genovese, A.; Vicidomini, G.; Diaspro, A.; Brovelli, S.; Manna, L.; Moreels, I. J. Mat. Chem. C 2014, 2, (17), 3439-3447.

13. We estimated the number of monolayers assumimg each layer of CdS had a thickness of 0.35nm.

14. Because the extinction coefficient increase continously on the high energy side, the absorption spectra were normalized by equalizing all spectra to 1 at 450nm.

15. Bomm, J.; Büchtemann, A.; Fiore, A.; Manna, L.; Nelson, J. H.; Hill, D.; van Sark, W. G. J. H. M. Fabrication and Spectroscopic Studies on Highly Luminescent Cdse/Cds Nanorod Polymer Composites. *Beilstein J. Nanotechnol.* **2010,** *1*, 94-100.

16. A 5 point Savitzky-Golay algorith was applied to the EQE spectrum measured with the edges to reduce the noise.

17. Şahin, D.; Ilan, B.; Kelley, D. F. Monte-Carlo Simulations of Light Propagation in Luminescent Solar Concentrators Based on Semiconductor Nanoparticles. *J. Appl. Phys.* **2011,** *110*, 033108.

18. Meinardi, F.; Colombo, A.; Velizhanin, K. A.; Simonutti, R.; Lorenzon, M.; Beverina, L.; Viswanatha, R.; Klimov, V. I.; Brovelli, S. Large-Area Luminescent Solar Concentrators Based on `Stokes-Shift-Engineered' Nanocrystals in a Mass-Polymerized Pmma Matrix. *Nat Photon* **2014,** *8*, 392-399.

19. Carbone, L.; Nobile, C.; De Giorgi, M.; Sala, F. D.; Morello, G.; Pompa, P.; Hytch, M.; Snoeck, E.; Fiore, A.; Franchini, I. R.; Nadasan, M.; Silvestre, A. F.; Chiodo, L.; Kudera, S.; Cingolani, R.; Krahne, R.; Manna, L. Synthesis and Micrometer-Scale Assembly of Colloidal Cdse/Cds Nanorods Prepared by a Seeded Growth Approach. *Nano Lett.* **2007,** *7*, 2942-2950.

20. Pietra, F.; Rabouw, F. T.; Evers, W. H.; Byelov, D. V.; Petukhov, A. V.; de Mello Donegá, C.; Vanmaekelbergh, D. Semiconductor Nanorod Self-Assembly at the Liquid/Air Interface Studied by in Situ Gisaxs and Ex Situ Tem. *Nano Letters* **2012,** 121012095940001.

21. Zanella, M.; Gomes, R.; Povia, M.; Giannini, C.; Zhang, Y.; Riskin, A.; Van Bael, M.; Hens, Z.; Manna, L. Self-Assembled Multilayers of Vertically Aligned Semiconductor Nanorods on Device-Scale Areas. *Advanced Materials* **2011,** *23*, 2205-2209.

22. Singh, A.; English, N. J.; Ryan, K. M. Highly Ordered Nanorod Assemblies Extending over Device Scale Areas and in Controlled Multilayers by Electrophoretic Deposition. *The Journal of Physical Chemistry B* **2013,** *117*, 1608-1615.

23. Acharya, S.; Kundu, S.; Hill, J. P.; Richards, G. J.; Ariga, K. Nanorod-Driven Orientational Control of Liquid Crystal for Polarization-Tailored Electro-Optic Devices. *Advanced Materials* **2009,** *21*, 989-993.

24. Kundu, S.; Hill, J. P.; Richards, G. J.; Ariga, K.; Khan, A. H.; Thupakula, U.; Acharya, S. Ultranarrow Pbs Nanorod-Nematic Liquid Crystal Blend for Enhanced Electro-Optic Properties. *ACS Appl. Mater. Interfaces* **2010,** *2*, 2759-2766.

25. Wu, K. J.; Chu, K. C.; Chao, C. Y.; Chen, Y. F.; Lai, C. W.; Kang, C. C.; Chen, C. Y.; Chou, P. T. Cds Nanorods Imbedded in Liquid Crystal Cells for Smart Optoelectronic Devices. *Nano Letters* **2007,** *7*, 1908-1913.

26. Hung, A. M.; Oh, T.; Cha, J. N. Facile Thermal Treatment Process for Assembling Vertically Aligned Semiconductor Nanorods in Solution. *Nanoscale* **2012,** *4*, 1016.

CHAPTER 4

The Evolution of the Electronic and Optical Properties in CdSe/CdS Heterostructures: The Central Role of Electron Delocalization

Over the past two decades dramatic progress has been made in unravelling the electronic properties of quantum dots and the optical properties they give rise to. The combination of theoretical advances and optical studies at the batch and single particle level have rapidly expanded our understanding of the electronic properties of quantum dots and related nanostructures. Nevertheless, in spite of this vast progress, several fundamental questions have remained largely unanswered. One such question relates to the mechanisms that dominate the dramatic broadening of the lineshape of quantum dots such as CdSe from less than 1meV at cryogenic temperatures (4K) to up to 100meV at room temperature.[1-3]

In order to gain insight into the dominant mechanisms of exciton-phonon coupling in quantum dots, we have studied a series of CdSe/CdS quantum dots with different core sizes and shell thicknesses. The quasi-type II band alignment in this system makes it possible to synthetically tune the effective spatial separation between the hole and the electron in the excited state of the nanocrystal.[1, 4] Through a combination of time resolved fluorescence spectroscopy and single dot fluorescence spectroscopy at a broad range of temperatures (4K –

300K), we have sought to quantify the strength of the exciton-phonon coupling as a function of the physical structure of the nanocrystal. Finally, a unified model is used to describe the evolution of the lineshape as a function of the temperature in terms of these exciton-phonon coupling parameters.

4.1 Electron Delocalization into the Shell in CdSe/CdS Quantum Dots

A key defining feature of the CdSe/CdS system is the fact that the conduction bands of CdSe and CdS lie close in energy, making it possible for the electron to delocalize from CdSe to CdS.[4, 5] Fig. 4-1 illustrates the qualitative picture that arises from this quasi-degeneracy of the conduction bands. Upon thermalization of the exciton, an electron and hole will lie at an energy higher than the valence and conduction band of CdSe respectively. In the case of the hole, the energetic barrier to crossing into CdS is so high that its wavefunction

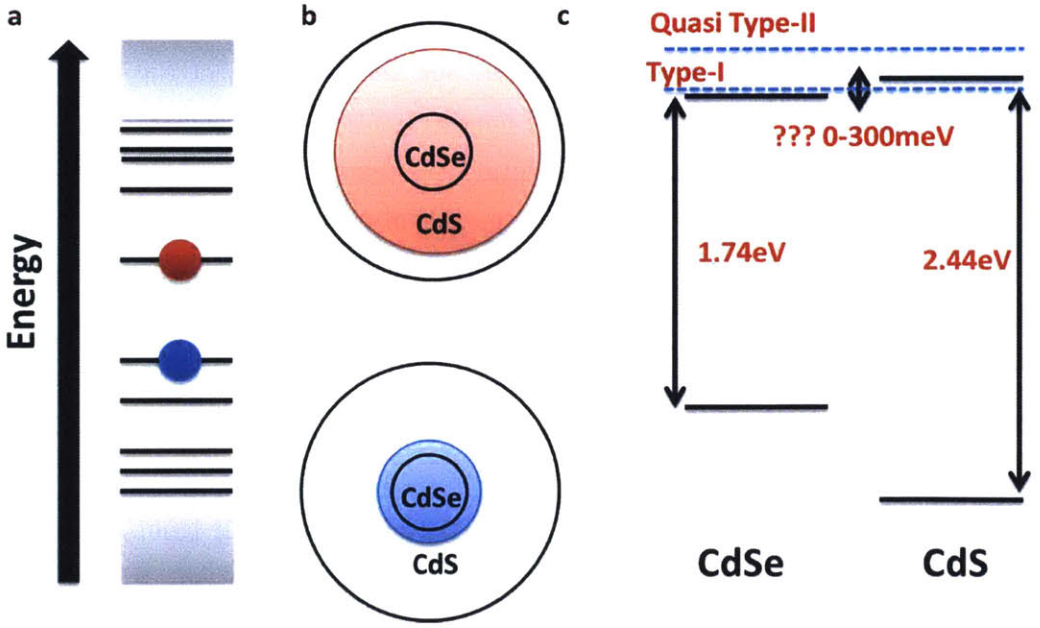

Figure 4-1: The band alignment in CdSe/CdS; a) a band edge electron (red) and a band-edge hole (blue); b) the spatial extent of the electron and hole wavefunctions; c) uncertainty in the band offset of the CdSe and CdS conduction bands

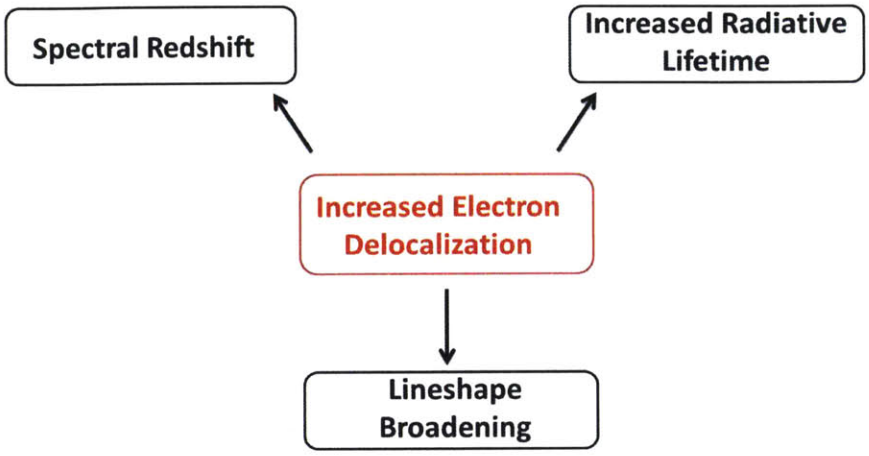

Figure 4-2: The central role of electron delocalization in shaping the electronic and optical properties of CdSe/CdS

will mostly be localized to the core. In contrast, in the case of the electron, the energetic barrier for the particle to delocalize into CdSe is sufficiently small that significant delocalization can be expected. The specific details about this band offset are still under debate in the literature. Estimates for the band offset have ranged from 0-300meV and it has also been suggested that this value can vary as a function of the core size and the temperature.[4, 6] The uncertainty regarding the band offset also makes it more difficult to estimate whether a given CdSe/CdS heterostructure is better described as type I or quasi type II. The question is whether the lowest lying state for the electron lies below (type I) or above (type II) the energy of the conduction band in CdS.[6] Nevertheless, in spite of the debate regarding the detailed nature of the conduction band offset, there is general agreement about the strong tendency of the electron to delocalize into the CdS shell.

The ability of the electron to delocalize into the shell can be monitored by probing the evolution of the optical properties of CdSe/CdS as a function of the shell thickness. Specifically, there are three main effects one generally observes: 1)

a gradual redshift of the PL maximum, 2) a gradually increasing radiative lifetime, and 3) broadening of the photoluminescence lineshape. The first and third effects can clearly be seen figure 4-3 below, showing the evolution of the lineshape of a series of CdSe/CdS dots as a function of the shell volume. The next three subsections will look at each broadening mechanism individually.

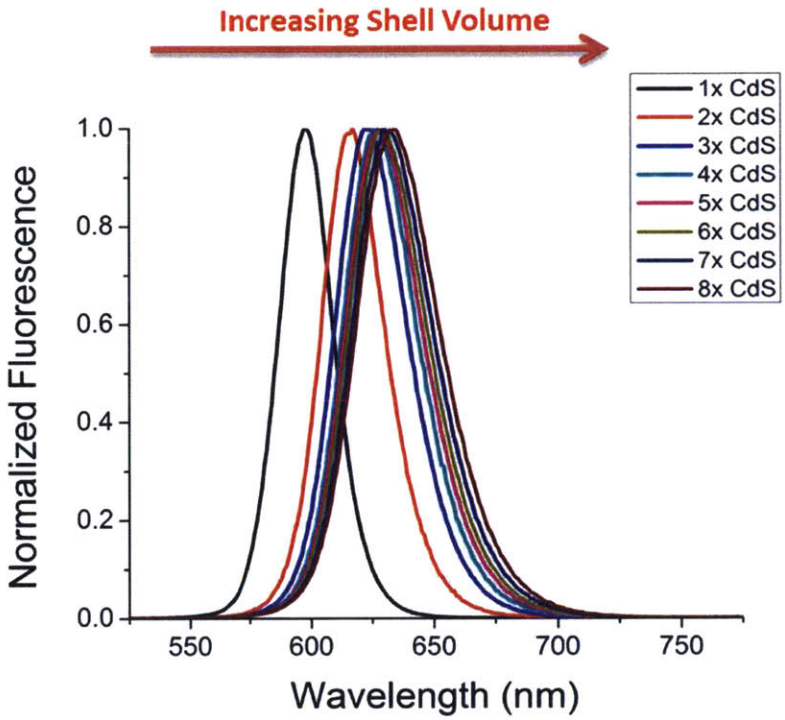

Figure 4-3: The evolution of the fluorescence peak of a series of CdSe/CdS dots with a core with a first excitation feature at 563nm

4.1.1 Change in the Energy of the Fluorescence as a Function of the Shell Thickness in CdSe/CdS Quantum Dots

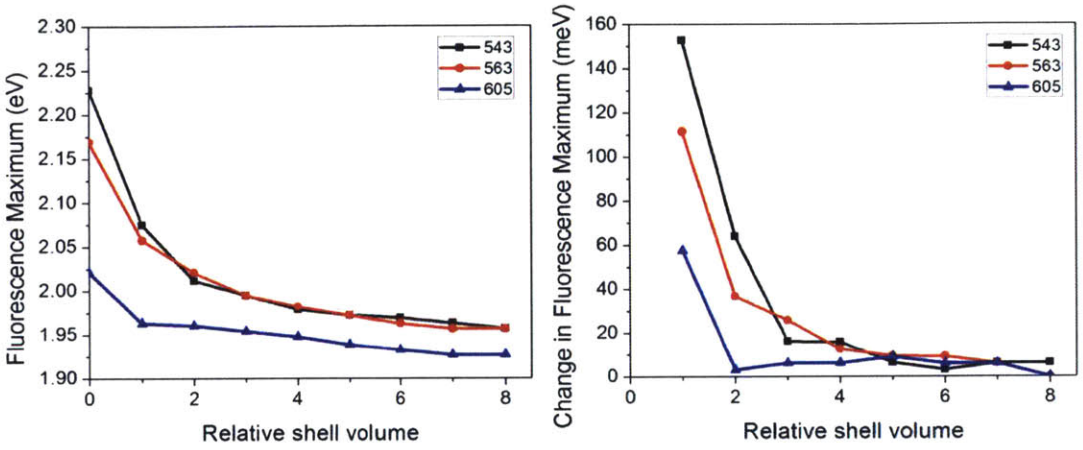

Figure 4-4: The evolution of the fluorescence maximum vs shell thickness (a) and the relative change in the fluorescence maximum for each step of the shell growth (b)

A ubiquitous process in CdSe/CdS dots is the redshift of the fluorescence band upon growth of the CdS shell. Figure 4-4 above shows the gradual decrease in the energy of the fluorescence peak as a function of the shell volume for three series of CdSe/CdS dots with different core sizes. Three effects are apparent in the graphs below: 1) the energy decrease is monotonic with the shell volume, 2) the energy decreases fastest at the beginning of the shell growth but eventually reaches an asymptote and 3) the energy decrease occurs fastest for the smallest cores (see the right side of Fig. 4-4).

We can rationalize this behavior by considering the various contributions that determine the total energy of the exciton. These contributions are listed in the equation below where the confinement energy of the hole and the electron are written separately:

$$E_{exciton} = E_{bandgap} + E_{conf.,hole} + E_{conf.,electron} + E_{coulomb}$$

(4-1)

The first term ($E_{bandgap}$) is simply the bulk bandgap of CdSe and this term can safely be taken to be constant. Next, we have the two confinement terms for the hole and the electron respectively ($E_{conf.,hole}$ and $E_{conf.,electron}$). Because the hole is largely confined to the core, this term should only decrease slightly as the shell increases in thickness. On the other hand, in the case of the electron we can expect that the energy will continuously decrease as the electron can relax in energy by delocalizing into the shell. Finally, the electrostatic attraction between the core and the electron will also decrease as the shell increases and the average separation between the two charge carriers tends to increase.

As a result, the fact that the fluorescence maximum decreases with the shell thickness until it approaches ~1.9eV reflects the loss of the electron confinement energy and the coulombic term. What is left in the end is the bulk bandgap energy of CdSe (1.7eV) and the confinement energy of the hole (~200-300meV). The more rapid relaxation seen for smaller CdSe cores simply reflects the fact that the electron confinement energy is higher in the beginning, creating a greater driving force for the electron to delocalize into the shell. Likewise the fact that the final energy of the thick-shelled dots is lowest for the smallest cores reflects the fact that these particles have the lowest hole confinement energy.

4.1.2 Change in the Radiative Lifetime of CdSe/CdS Quantum Dots as a Function of the Shell Thickness

A key property of CdSe/CdS systems of different dimensionalities is a gradual lengthening of the radiative lifetime as a function of the volume of the CdS shell.[4, 7-9] This increase in the lifetime is a direct consequence of the increased separation between the hole and the electron caused by electron delocalization into the shell. Specifically, the radiative rate (the reciprocal of the radiative lifetime) will be proportional to the overlap integral (K) between the wavefunctions of the hole ($R^h(r)$) and the electron($R^e(r)$) as shown in the equation below[10]:

$$K = \left| \int_0^R dr r^2 R^e(r) R^h(r) \right|^2 \tag{4-2}$$

This behavior is illustrated in fig 4-5 below for a series of CdSe/CdS dots with a core having an initial absorption feature at 605nm. What is apparent is that the increase in the lifetime is both monotonic as a function of the shell volume as well as the fact that it does not appear to saturate. Moreover, as one can see from Fig. 4-6, for smaller cores, the increase in the radiative lifetime as a function of the shell volume is even steeper and it again does not seem to saturate. In fact, for even larger shell volumes, the radiative lifetime has been reported to increase by at least an additional order of magnitude, reaching microseconds.[11, 12]

This behavior directly follows from the tendency of the electron to delocalize into the shell. In the absence of any barrier for delocalization, the overlap integral between would simply be proportional to the volumetric fraction of the core (where the hole is confined) to the total volume of the quantum dot (over which the electron can extend). The approximately linear increase of the

radiative lifetime with the shell volume seen in Fig 4-6 is fully consistent with this picture. The qualitative behavior of the evolution in the radiative lifetime will be considered in more detail in section 4.1.4, where we will discuss the change in the spatial distribution of the electron within a simple theoretical framework based on the effective mass approximation.

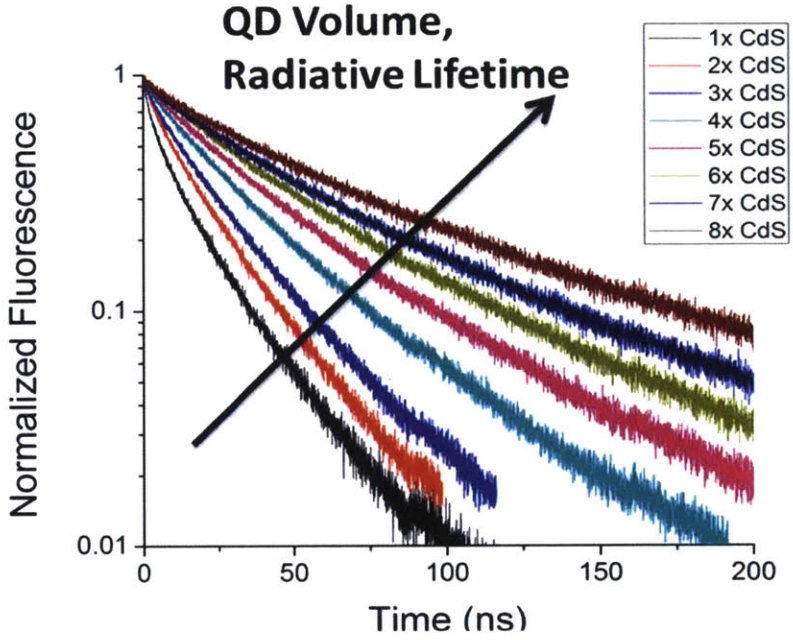

Figure 4-5: Normalized time-resolves photolumienscence of a series of CdSe/CdS dots, using a core with a first absorption feature at 605nm

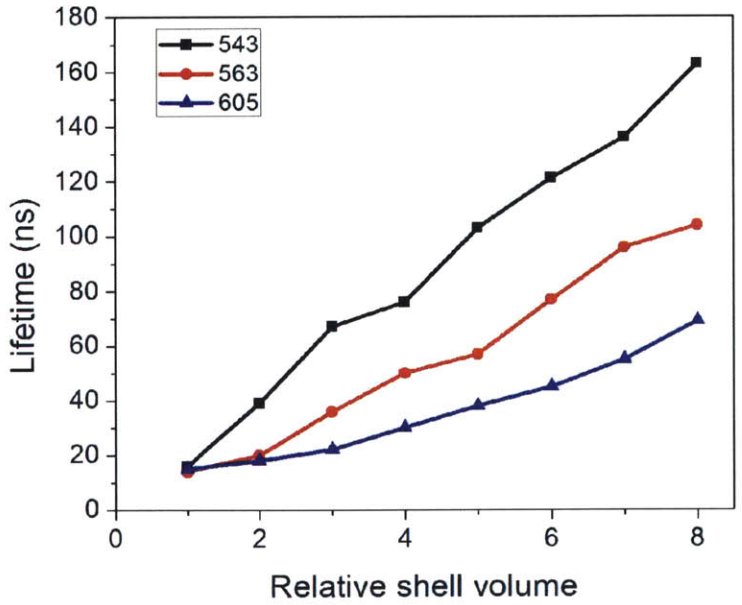

Figure 4-6: Evolution of the PL lifetime in CdSe/CdS QDs vs the shell volume for 3 different core sizes

4.1.3 Change in the Fluorescence Lineshape of CdSe/CdS Quantum Dots as a Function of the Shell Thickness

The last key process observed upon growth of the CdS shell is a gradual broadening of the lineshape. This evolution can clearly be seen in Fig 4-7 for one series of CdSe/CdS dots and is summarized for a series of different core sizes in Fig. 4-8 above. The key behavior observed is that after the growth of the first shell layer, every subsequent growth step results in a monotonic broadening of the lineshape. The key limitation of the data presented above is that it is based on ensemble-level experiments and thus cannot unambiguously rule out whether the broadening is primarily due a change in the single dot lineshape or to an increase in inhomogeneous broadening. In order to more directly look at the evolution of the intrinsic fluorescence lineshape in this system, we complement the ensemble level data with single particle measurements as described in subsequent sections.

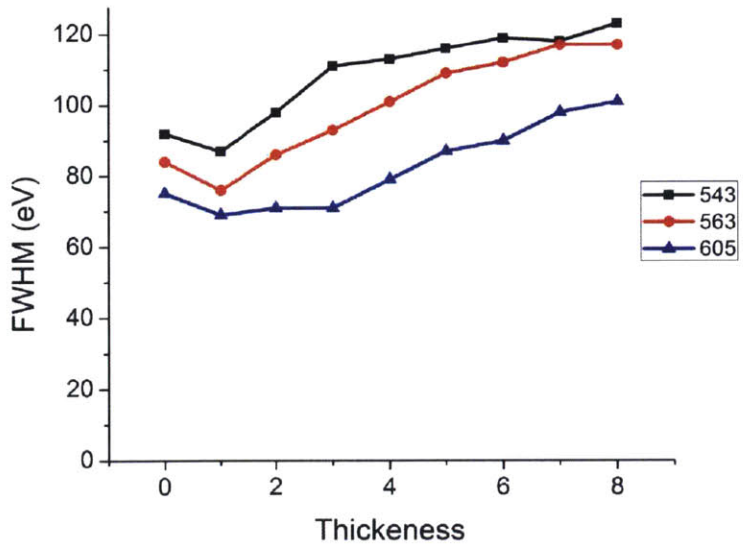

Figure 4-7: Evolution of the FWHM of the fluorescence spectrum of CdSe/CdS QDs vs the shell volume for 3 different core sizes

4.1.4 Modeling of the Electron Delocalization in CdSe/CdS

In order to gain more physical insight into the evolution of the electronic properties of CdSe/CdS dots, we modelled the evolution of the electron wavefunction in CdSe/CdS dots using a simple numerical model. The entire model is designed in the framework of the effective mass approximation. The starting point of the model is particle in an infinite sphere where the electron is placed in a spherical confining potential that has an infinitely high barrier at $r = R_s$, where R_s is the total radius of the particle. Next, we modify the potential by adding an energy offset ΔE to the interval $R_c \leq r < R_s$, where R_c is the edge of the core, in order to account for the conduction band offset between the core and the shell. Finally, an electrostatic term is added to account for the attraction between the hole and the electron. The hole is treated as a simple point charge located at the center of the quantum dot. The effective mass of the electron is defined separately for the core and electron based on literature data, as are the dielectric constant of the core and shell.

The results of the simulation are shown in Fig. 4-8 below. Panels a and b show the evolution of the radial distribution function (RDF) of the electron as a function of the shell thickness.[13] In panel a, no electrostatic interaction is included and as a result, the distribution of the electron becomes increasingly concentrated in the shell. In contrast, when the electrostatic interaction is turned on, one can see that while the electron rapidly delocalizes in the beginning, for larger shell thicknesses the RDF stops changing significantly. This result is not surprising when considering the Wannier picture for excitons in bulk semiconductors. In the latter case, even when the electron is not confined by an external potential, at low temperatures it will be bound to the hole electrostatically such that its RDF will peak at the exciton Bohr radius.

Nevertheless, while the results of the simulation as described so far for a thick shell are consistent with the bulk limit, they cannot fully be reconciled with the experimental data for thick-shelled quantum dots. Specifically, as previously

mentioned, the radiative lifetime is known to increase continuously with the shell thickness, even after it becomes much larger than the exciton Bohr radius. The solution to this apparent contradiction is that so far we have only considered the ground state of the exciton. When solving for the higher level states, (e.g. the 2s state as shown panel c in Fig. 4-8), we see that the RDF for these states extends much further into the shell. We can once again describe this situation in terms analogous to the bulk case. One can treat the bulk semiconductor as an infinitely large "box," such that there is a continuous band of states past the ionization limit. At finite temperatures the electron in a bulk exciton can be kicked into one of these free states through a thermally activated process, effective ionizing the exciton. It is for this reason that excitons in systems like CdSe or PbS are not observed at room temperature. In contrast in a quantum dot even when the electron is excited into the higher-level electronic states, it never becomes fully free since its spatial extent is still limited by the physical size of the dot. As a result, one can think of the electron as effectively being in equilibrium between the ground state and higher level states where it is almost free. Because in this picture the electron can once again sample the entire volume of the nanocrystal, we can expect that its average separation from the hole will again increase monotonically with the volume of the shell, in qualitative agreement with the experimental data.

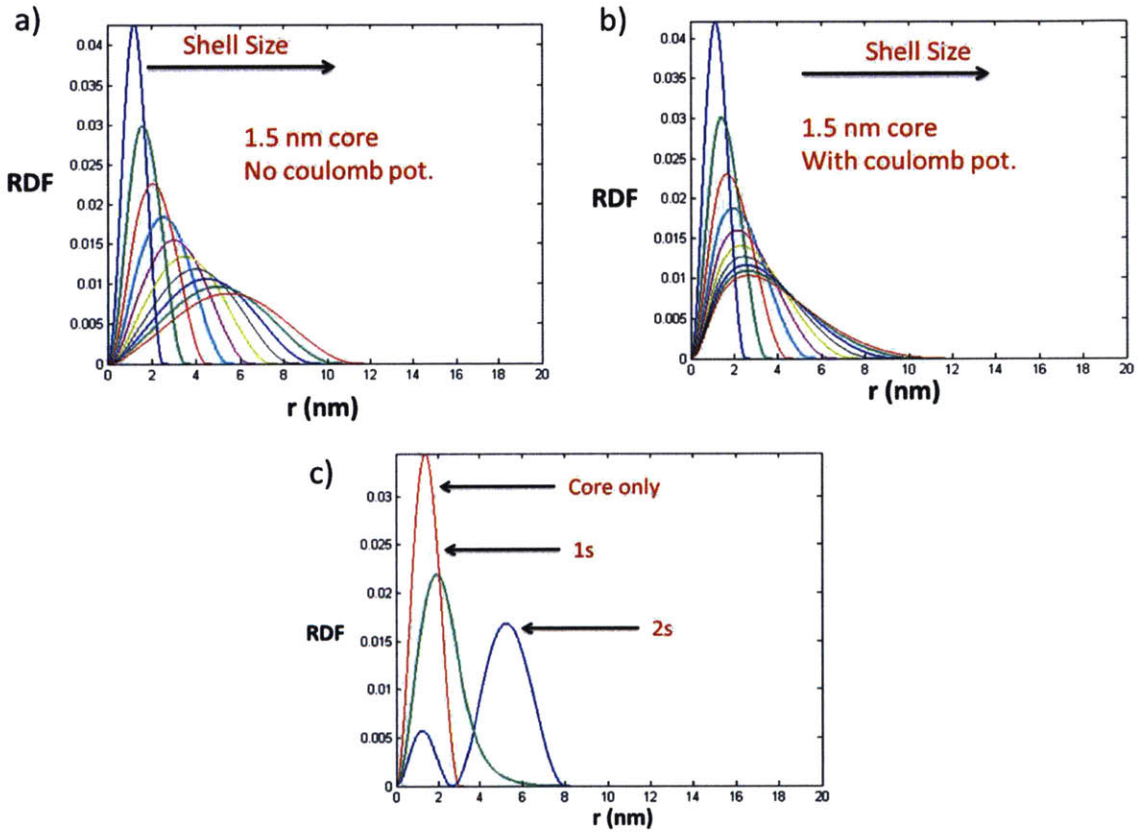

Figure 4-8: The evolution of the radial distribution function (RDF) for the electron in CdSe/CdS as a function of the shell thickness for a) no Coulomb potential and b) in the presence of a Coulomb potential and c) the ground and first excited state

4.2 Unraveling the Photoluminescence Lineshape of CdSe/CdS

4.2.1 General Considerations

Although the lineshape of quantum dots such as CdSe/CdS may at first sight appear to be simple and featureless at room temperature, the full physical picture is much more complex. The lineshape reflects the interplay of 1) the electronic transitions that contribute to the photoluminescence, 2) the phonons that couple to these transitions, and 3) the effect of the quantum dot environment on these states. In order to understand the mechanisms that dominate the broad lineshapes of CdSe/CdS and related systems at room temperature, we need to consider the contribution from each of these sources individually.

Even at low temperatures it is apparent that the steady-state central photoluminescence peak (the zero optical phonon line or ZPL) is much broader than the natural linewidth estimated from the radiative lifetime. Part of the broadening is due to internal processes, such as dephasing induced by spin-flips or acoustic phonon assisted processes.[14, 15] Nevertheless, in many colloidal nanostructures, a more important broadening mechanism is energy fluctuation of ZPL.[16, 17] This process, generally called spectral diffusion, is likely due to the Stark effect mediated by the fluctuating electrostatic environment that surrounds the nanostructure. However, it is important to note that in the case of CdSe/CdS quantum dots, especially for thicker shells, the combined contribution arising from dephasing spectral diffusion leads to broadening by less than 1meV.[17] In other words, while these processes have a large impact of the lineshape observed at low temperatures, these factors can only play a modest role in explaining the broad lineshape observed at room temperature.

The next natural source of broadening to consider is the fine structure of the exciton. In contrast to simple organic chromophores where only one electronic state (usually the lowest lying singlet) is responsible for the photoluminescence,

in quantum dots one often finds that multiple electronic states lie close enough in energy to contribute to the lineshape. In the case of CdSe-based quantum dots, the detailed structure of the band-edge states has been thoroughly studied using a combination of theoretical and experimental studies.[6, 18-20] Before considering the fine structure, the lowest lying state of an exciton in a spherical CdSe quantum dot is 8-fold degenerate. This degeneracy is broken by considering 1) the crystal-field splitting between the light and heavy hole (~20meV in CdSe) and 2) the exchange energy. As a result of these two contributions, the band-edge state splits into five distinct groups as shown in Fig. 4-9 below. Because the exchange energy scales as $\sim r^{-3}$, where r is the radius of the particle, this contribution is pronounced for small QD sizes ($r < 2nm$), but becomes negligible for larger particles.[19] In the latter case, the only key contribution that remains is the crystal field splitting, which explains why all states separate into two branches separated by ~20meV.

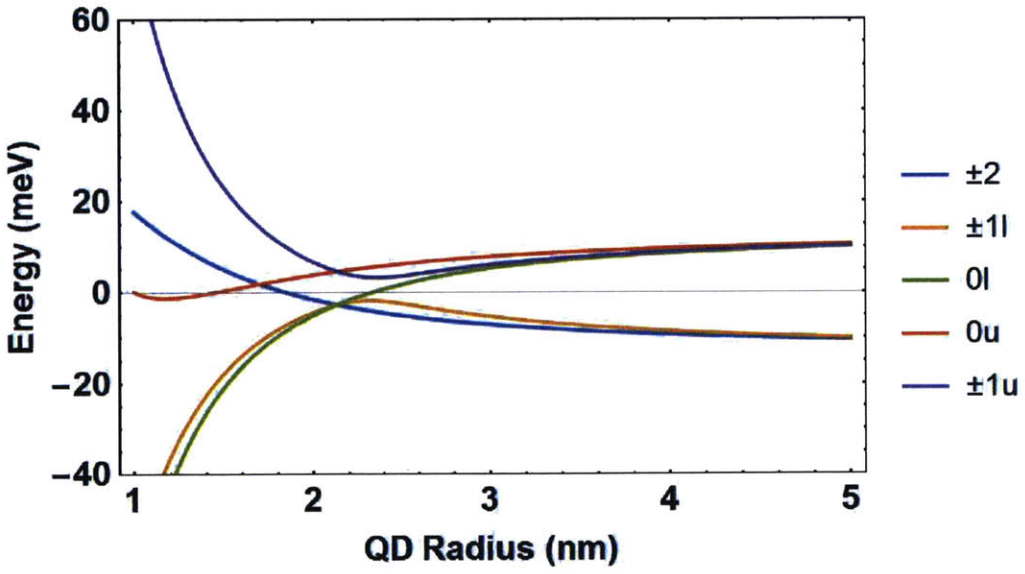

Figure 4-9: The eight band-edge fine structure states in spherical wurtzite CdSe quantum dots vs. QD radius

4.2.2 Exciton-Phonon Coupling in CdSe/CdS

The last, and dominant, mechanism affecting the lineshape of CdSe/CdS quantum dots is exciton-phonon coupling. The simplest model within which one can consider exciton phonon coupling is the independent boson model, where a manifold of electronic states (n) is coupled to a bath of vibrational states (α), with a linear, diagonal coupling strength Γ_α. The Hamiltonian governing this interaction is given in eq. 4-3 below:

$$\hat{H} = \sum_n E_n |n><n| + \sum_\alpha \hbar\omega_\alpha (b_\alpha^\dagger b_\alpha + \frac{1}{2}) + \sum_{n,\alpha} \Gamma_\alpha (b_\alpha^\dagger + b_\alpha)|n><n| \tag{4-3}$$

The coupling to each phonon mode produces a lineshape that has an analytical solution, which at 0K resembles a picket fence structure with discrete satellites at energies given by $m\hbar\omega_\alpha$, where n is an integer and $\hbar\omega_\alpha$is the energy of the respective mode. Each satellite will be weighted by a Poisson pre-factor to give the lineshape function $I_\alpha(E)$ defined by:

$$I_\alpha(E) = 2\pi e^{-g} \sum_{m=0}^{\infty} \frac{{g_\alpha}^m}{m!} \delta(E - E_0 + \frac{{\Gamma_\alpha}^2}{\hbar\omega_\alpha} - m\hbar\omega_\alpha) \tag{4-4}$$

where g_α is a dimensionless exciton-phonon coupling term called the Huang-Rhys factor as defined below:

$$g_\alpha = \frac{{\Gamma_\alpha}^2}{\hbar\omega_\alpha} \tag{4-5}$$

and E_0 is the energy of the electronic transition in the absence of exciton-phonon coupling. The typical lineshape for a two-level electronic system coupled to a single phonon mode at 0K is shown in Fig 4-10 below. If the electronic transition is coupled to multiple vibrational modes, total lineshape is given by the convolution of the lineshape obtained for each mode individually ($I_{gn}(E)$) as shown in eq. 4-6.[21]

$$I(E) = I_{g1}(E) \otimes I_{g1}(E) \otimes I_{g2}(E) \ldots \otimes I_{gn}(E) \tag{4-6}$$

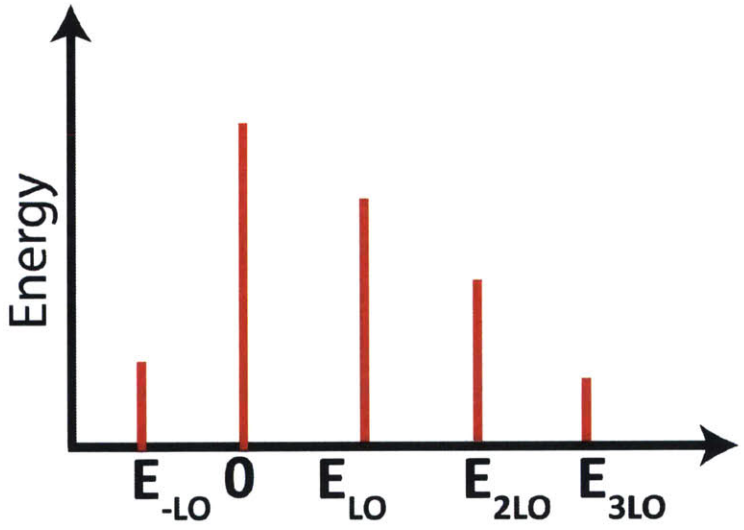

Figure 4-10: The phonon progression of a two-level system coupled to one phonon mode with Energy E_{LO}

4.2.3 Simulating the Spectrum of CdSe/CdS Quantum Dots: General Features

For core/shell quantum dots such as CdSe/CdS, the simplest model that can capture the essence of the underlying physics is one that considers 1) coupling to the LO phonons of the core and/or the shell and 2) the low-energy vibrational modes, including the acoustic phonon branches and ligand vibrations. A crude approximation can be made by representing all of coupling to the low energy modes by one effective mode which carries all the spectral density. For our particular system, we include three modes: 1) the LO phonon mode of CdSe at an energy of 26meV, 2) the LO phonon of CdS at 39meV, and 3) an effective bath mode at 1.5meV. The model also includes two distinct electronic states separated by 20meV representing the two lowest lying fine structure states, each of which is assumed to couple identically to the available phonon modes.

Using Huang-Rhys factors of 0.06 for the optical phonon modes and 0.6 for the bath mode, we can reproduce the qualitative features that are generally observed at low temperature (4K), which include, a narrow zero-phonon line with an acoustic phonon shoulder, and discrete satellites for the LO phonon modes. However, using the same Hamiltonian and simply raising the temperature cannot reproduce the observed spectra. Instead of seeing a broad (FWHM>50meV) and featureless lineshape, we see a narrow ZPL (with a FWHM ~20meV) and a well-defined shoulder. The failure to reproduce both the low and room temperature results is not an artifact of the spectral density chosen, but is a direct limitation of the linear coupling scheme considered.

This discrepancy can be addressed by going beyond the independent boson Hamiltonian. Further refinement of the model can include the consideration of 1) second order exciton-phonon coupling terms, 2) non-adiabatic couplings (i.e. phonon assisted electronic transitions) and 3) a temperature dependence of the Huang-Rhys factor, as shown in eq. 3.[22, 23]

$$\sum_n E_n|n><n| + \sum_\alpha \hbar\omega_\alpha(b_\alpha^\dagger b_\alpha + \frac{1}{2}) + \sum_{n,m,\alpha} \Gamma_{nm\alpha}(b_\alpha^\dagger + b_\alpha)|n><m| + \sum_{n,\alpha} \Lambda_{n\alpha}(b_\alpha^\dagger + b_\alpha)(b_\alpha^\dagger + b_\alpha)|n><n| \quad (4\text{-}7)$$

From the room temperature spectrum alone, one can't distinguish between these possible mechanisms. However, most of the terms described above result in an additional contribution to the Lorentzian component of the linewidth that is linearly proportional to the temperature.[22, 23] Empirically we can introduce such a term into our lineshape function in order to better fit the experimental data, as shown in Fig. 4-11. This additional term makes it possible to correctly obtain all the key spectral features both at high and low temperatures. This model now allows us to estimate the effect on the linewidth associated with changing any of its parameters. For example, increasing the coupling to LO phonons from 0.06 to 0.2 results in an increase of the FHWM by ≈20meV. The magnitude of such a change in the coupling strength would be consistent with a change in the nature of the charge carriers, from the case of high mutual screening for neutral, core only QDs to increased separation in quasi type II systems such as CdSe/CdS. In fact, the more the charges are allowed to separate, the more the coupling strength should resemble that found in the bulk, which for CdSe corresponds to a Huang-Rhys factor of ≈1.[24]

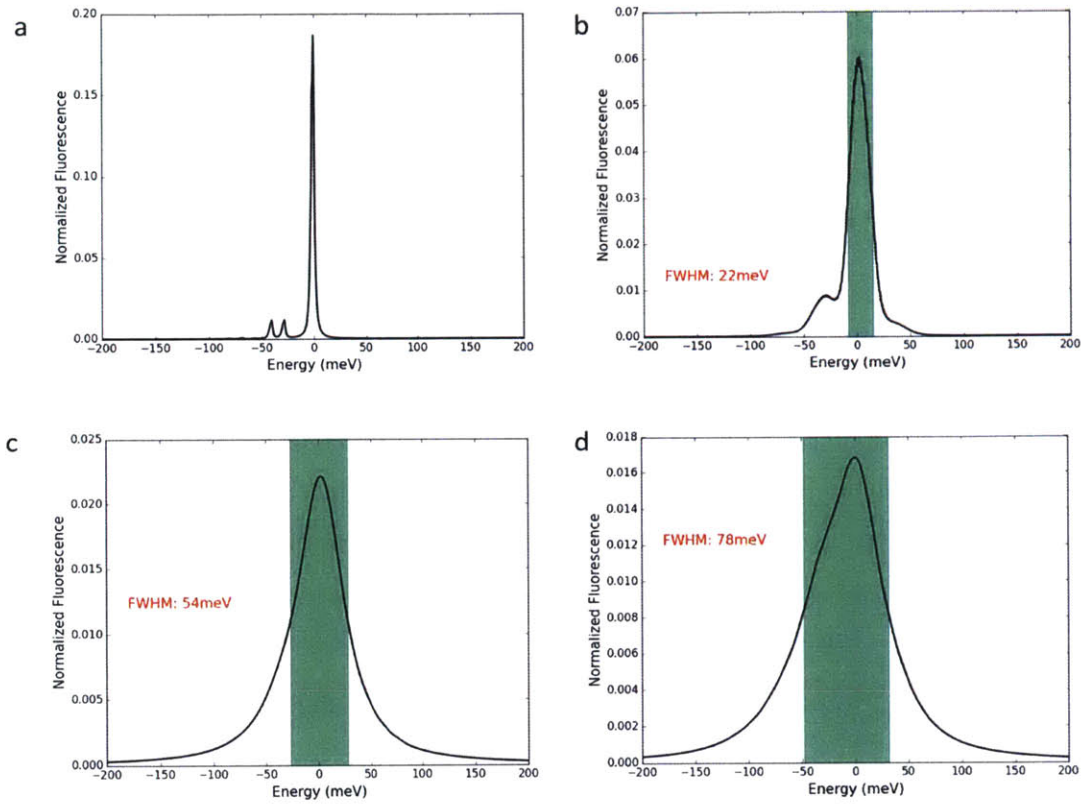

Figure 4-11: Simulations of the fluorescence lineshape at: a) 4K with no linear temperature dependence, g1=g2=0.06, g3=0.6; b) 300 K with no linear temperature dependence, g1=g2=0.06, g3=0.6; c) 300 K with a linear temperature dependence, g1=g2=0.06, g3=0.6; d) 300 K

4.2.4 Experimental Measurement of the Temperature Dependent Fluorescence Spectra of Single CdSe/CdS/ZnS Quantum Dots

The most direct way to study the evolution of the single dot lineshape as a function of the temperature is by measuring the fluorescence spectrum of a series of individual quantum dots at different temperatures. While this experiment is straightforward in theory, in practice several key challenges must be overcome. One key problem is that it is often impossible to interrogate a single quantum dot for a prolonged period of time (i.e. over the course of hours) due to gradual photobleaching. Fortunately, the thick-shelled CdSe/CdS dots (with 15 monolayers of CdS) prepared according to the method described in Ch. 2 are particularly well-suited for this study as they show little degradation even over the course of days of measurements. To improve the stability even more we added an additional thin layer (~1-2monolayers) of ZnS. A second problem is the difficulty of keeping one dot in the focal volume while changing the temperature by hundreds of ~300K. A cryostat with an integrated piezoelectric stage (Montana Instruments) was used in combination with a program offering continuous feedback to keep a given dot centered on the camera.

The results of the temperature studies for a typical dot are shown in Fig. 4-12 below. The top panel shows the two key features observed upon raising the temperature: 1) a gradual redshift of the PL peak and 2) a monotonic broadening of the lineshape. In order to more clearly see the broadening the fluorescence spectrum is shown in Fig 4-12 where each plot is re-centered at the center of the peak. In addition to the broadening, one can also see the change in structure to the vibrational band, from discrete satellites at low temperatures, to a broad pedestal at intermediate temperatures, and finally to a broad featureless lineshape close to room temperature. This series of spectra was then combined with the theoretical model described in the previous section to quantify the exciton-phonon coupling we observed.

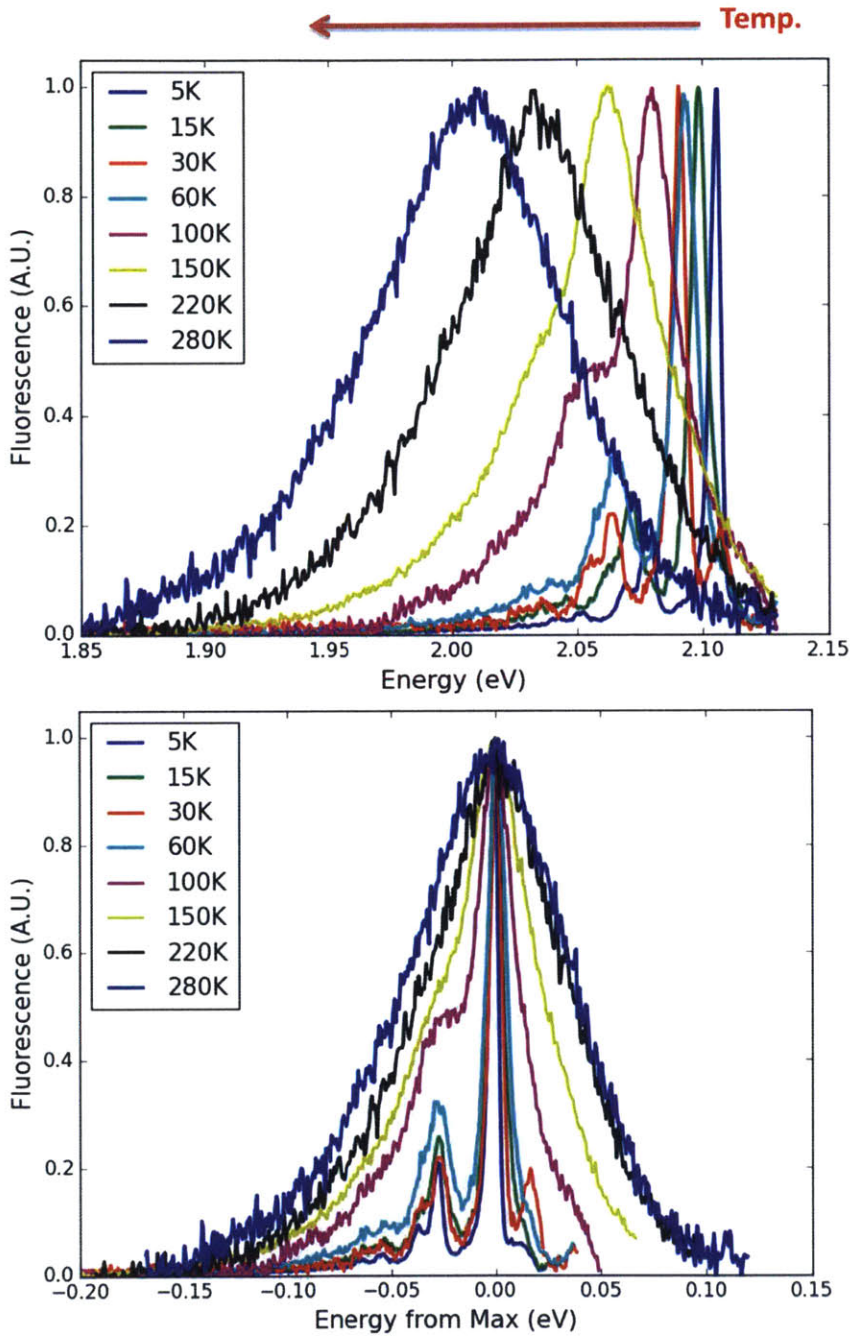

Figure 4-12: The Emission Spectra of Sample IC-I-95 plotted in absolute energy (top) and difference from peak energy (bottom)

4.2.5 Fitting the Experimental Temperature Dependent Data to the Lineshape Model

The data presented in the previous section was fit using the minimalistic model described in Section X. Again, three phonon modes were considered: the CdSe LO phonon, the CdS LO phonon, and an effective acoustic phonon mode. In addition, an additional term was introduced for the zero-phonon line, which increased linearly with the temperature. In order to fit the data we used the following steps: 1) the energy and Huang-Rhys factor for the CdSe and CdS LO phonon satellites and the acoustic phonon satellite was determined from the lowest energy spectrum (at 5K) and 2) the breadth of the ZPL and its temperature dependent broadening were fit to best describe the broadening form 5K to 280K. Just to emphasize, the same set of parameters obtained using this method was then used to simulate all 8 spectra as shown in the figure below.

The result of this analysis is shown in Fig. 4-13 and Fig. 4-14. As can clearly be seen from this series of spectra, a very good degree of agreement was seen between the experimental data and the simulation for the entire temperature range. This result indicates that the independent boson model augmented by a broadening term that is linear in the temperature is sufficient to capture all the main qualitative features of the fluorescence spectra of CdSe/CdS quantum dots across the broad temperature range studied here. The following coupling parameters were finally obtained: for the CdSe LO phonon mode: E=27meV, g=0.2; for the CdS LO phonon mode: E=36meV, g=0.07, and for the effective acoustic mode: E=1.5meV, g=0.3. The ZPL is treated as a Lorentizan function with a FWHM of $1.7 + \frac{8.5T}{1000}\ (meV)$. The 0K temperature limit of the ZPL reflects all factors that limit the narrowest ZPL we can measure, including spectral diffusion, additional dephasing processes, and the limited resolution of the spectrometer.

To put these numbers into context, for CdSe cores and thin-shelled CdSe/CdS samples, the Huang-Rhys factor observed for the CdSe mode is

usually on the order of 0.05.[3] For the thick-shelled dots studied in our experiment, the higher Huang-Rhys factor for the CdSe mode and the additional spectral density of the CdS mode were enough to introduce an additional broadening at room temperature on the order of ~20meV, consistent with the broadening observed both at the ensemble level (see section 4-7) as well as previous average single-particle measurements obtained using solution – photon correlated Fourier spectroscopy.[1, 25] In future work we plan to also measure the temperature dependent spectra for thin-shelled CdSe/CdS dots in order to make an even more direct comparison between the evolution of the lineshape in both limits of electron delocalization.

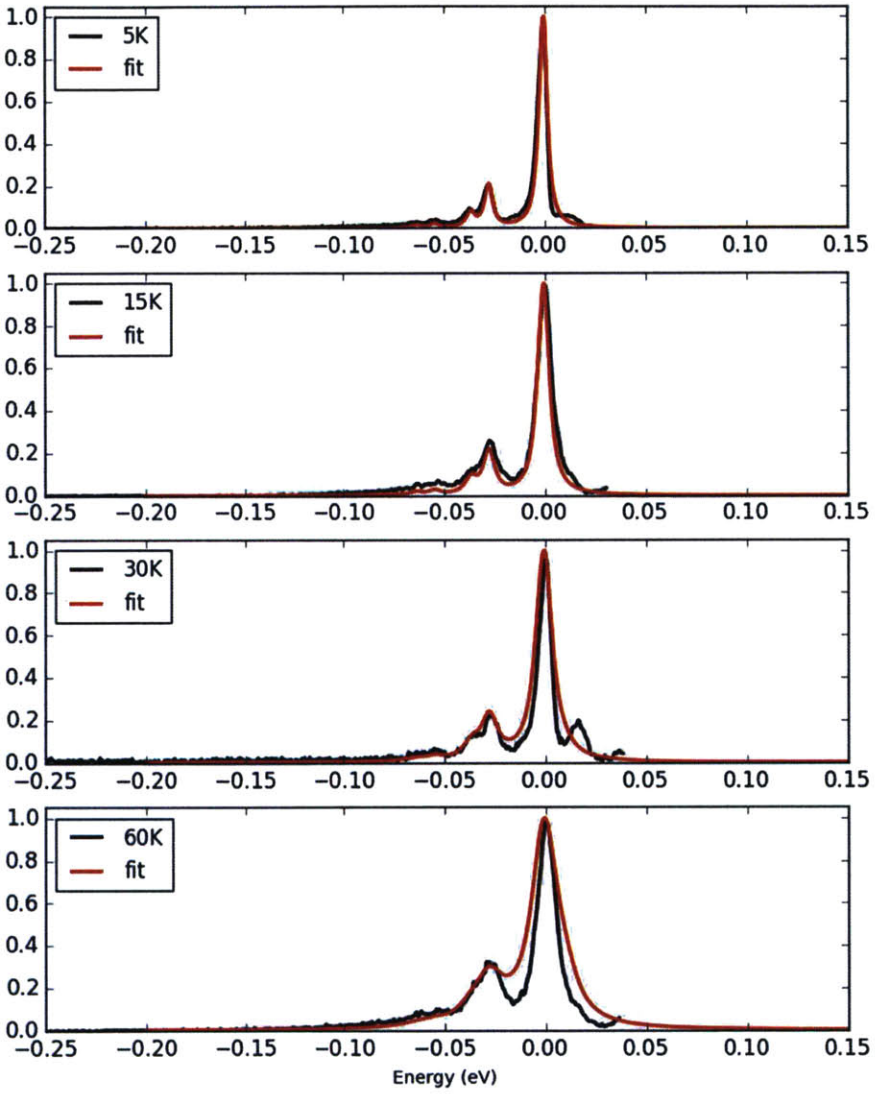

Figure 4-13: The evolution of the photoluminescence lineshape from 5K to 60K

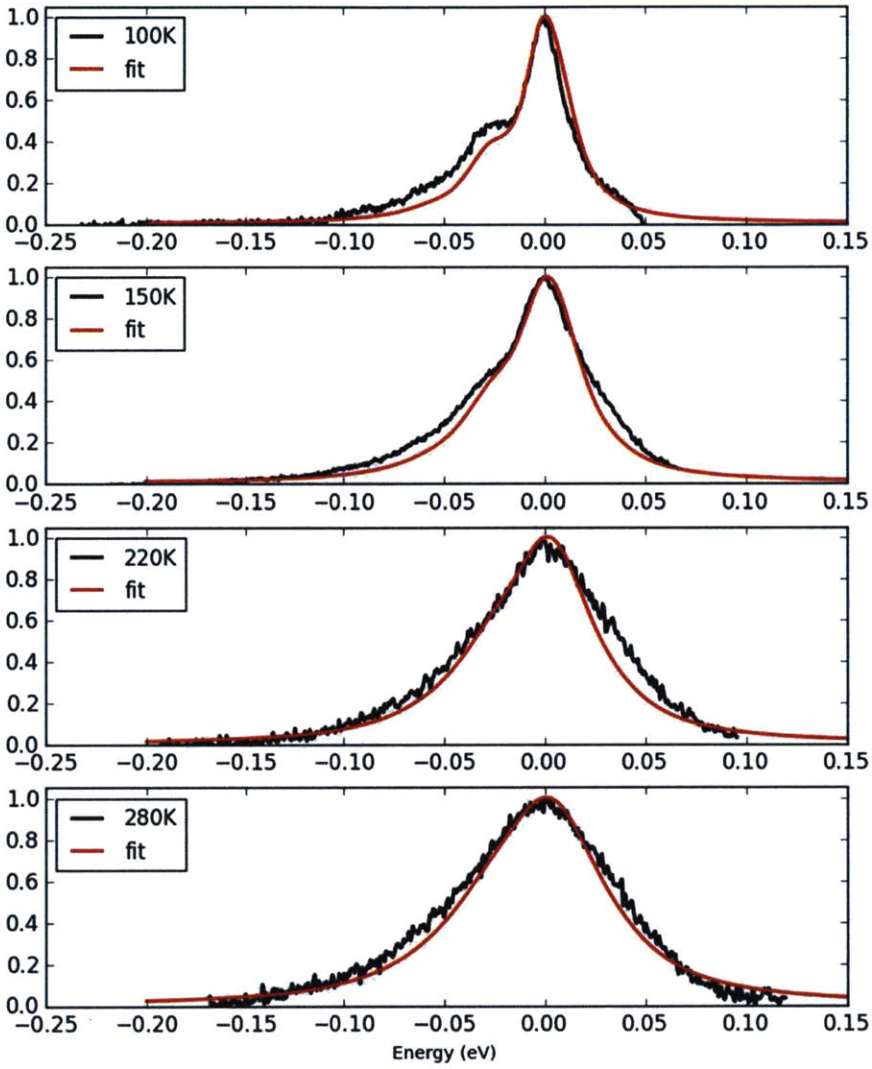

Figure 4-14: The evolution of the photoluminescence lineshape from 100K to 280K

4.3 Conclusions

In conclusion, we have studied the evolution of the optical and electronic properties of CdSe/CdS quantum dots using a combination of optical studies and theoretical simulations. As expected, electron delocalization into the CdS shell dominates the main changes observed, including a redshift of the emission band, the lengthening of the radiative lifetime, and the broadening of fluorescence lineshape. In addition, we measured the temperature dependent lifetime of a series of thick-shelled CdSe/CdS dots at the single particle level for a temperature range from 5K to 280K. The fluorescence spectra were then fit to a unified model for exciton-phonon coupling, which gave excellent agreement across a broad temperature range. In this second set of studies, electron delocalization once again emerged as a dominant process by increasing the strength of exciton-phonon coupling in thick-shelled dots compared to thin shelled dots. This increased coupling strength could then be related to the increased breadth of the fluorescence lineshape of thick-shelled CdSe/CdS dots observed both at the ensemble and single particle level.

References Ch. 4

1. Cui, J.; Beyler, A. P.; Coropceanu, I.; Cleary, L.; Avila, T. R.; Chen, Y.; Cordero, J. M.; Heathcote, S. L.; Harris, D. K.; Chen, O. Evolution of the Single-Nanocrystal Photoluminescence Linewidth with Size and Shell: Implications for Exciton–Phonon Coupling and the Optimization of Spectral Linewidths. *Nano Lett.* **2015**, *16*, 289-296.

2. Biadala, L.; Frederich, H.; Coolen, L.; Buil, S.; Quélin, X.; Javaux, C.; Nasilowski, M.; Dubertret, B.; Hermier, J. P. Photon-Correlation Fourier Spectroscopy of the Trion Fluorescence in Thick-Shell Cdse/Cds Nanocrystals. *Physical Review B* **2015**, *91*, 085416.

3. Fernée, M. J.; Littleton, B. N.; Cooper, S.; Rubinsztein-Dunlop, H.; Gómez, D. E.; Mulvaney, P. Acoustic Phonon Contributions to the Emission Spectrum of Single Cdse Nanocrystals. *The Journal of Physical Chemistry C* **2008**, *112*, 1878-1884.

4. Brovelli, S.; Schaller, R. D.; Crooker, S. A.; García-Santamaría, F.; Chen, Y.; Viswanatha, R.; Hollingsworth, J. A.; Htoon, H.; Klimov, V. I. Nano-Engineered Electron–Hole Exchange Interaction Controls Exciton Dynamics in Core–Shell Semiconductor Nanocrystals. *Nat. Commun.* **2011**, *2*, 280.

5. JavauxC; MahlerB; DubertretB; ShabaevA; Rodina, A. V.; EfrosAl, L.; Yakovlev, D. R.; LiuF; BayerM; CampsG; BiadalaL; BuilS; QuelinX; Hermier, J. P. Thermal Activation of Non-Radiative Auger Recombination in Charged Colloidal Nanocrystals. *Nat Nano* **2013**, *8*, 206-212.

6. Shabaev, A.; Rodina, A. V.; Efros, A. L. Fine Structure of the Band-Edge Excitons and Trions in Cdse/Cds Core/Shell Nanocrystals. *Physical Review B* **2012**, *86*.

7. Talapin, D. V.; Koeppe, R.; Gotzinger, S.; Kornowski, A.; Lupton, J. M.; Rogach, A. L.; Benson, O.; Feldmann, J.; Weller, H. Highly Emissive Colloidal Cdse/Cds Heterostructures of Mixed Dimensionality. *Nano Lett.* **2003**, *3*, 1677-1681.

8. Talapin, D. V.; Nelson, J. H.; Shevchenko, E. V.; Aloni, S.; Sadtler, B.; Alivisatos, A. P. Seeded Growth of Highly Luminescent Cdse/Cds

Nanoheterostructures with Rod and Tetrapod Morphologies. *Nano Lett.* **2007,** *7*, 2951-2959.

9. Coropceanu, I.; Rossinelli, A.; Caram, J. R.; Freyria, F. S.; Bawendi, M. G. Slow-Injection Growth of Seeded Cdse/Cds Nanorods with Unity Fluorescence Quantum Yield and Complete Shell to Core Energy Transfer. *ACS Nano* **2016,** *10*, 3295-3301.

10. Piryatinski, A.; Ivanov, S. A.; Tretiak, S.; Klimov, V. I. Effect of Quantum and Dielectric Confinement on the Exciton−Exciton Interaction Energy in Type Ii Core/Shell Semiconductor Nanocrystals. *Nano Lett.* **2007,** *7*, 108-115.

11. Nasilowski, M.; Spinicelli, P.; Patriarche, G.; Dubertret, B. Gradient Cdse/Cds Quantum Dots with Room Temperature Biexciton Unity Quantum Yield. *Nano Lett.* **2015,** *15*, 3953-3958.

12. Christodoulou, S.; Vaccaro, G.; Pinchetti, V.; De Donato, F.; Grim, J. Q.; Casu, A.; Genovese, A.; Vicidomini, G.; Diaspro, A.; Brovelli, S.; Manna, L.; Moreels, I. Synthesis of Highly Luminescent Wurtzite Cdse/Cds Giant-Shell Nanocrystals Using a Fast Continuous Injection Route. *J. Mater. Chem. C* **2014,** *2*, 3439-3447.

13. The shell thicknesses used were: 0.01 nm, 1 nm, 2 nm, 3 nm, 4 nm, 5 nm, 6 nm, 7 nm, 10nm

14. Salvador, M. R.; Graham, M. W.; Scholes, G. D. Exciton-Phonon Coupling and Disorder in the Excited States of Cdse Colloidal Quantum Dots. *The Journal of Chemical Physics* **2006,** *125*, 184709.

15. Goupalov, S. V.; Suris, R. A.; Lavallard, P.; Citrin, D. S. Exciton Dephasing and Absorption Line Shape in Semiconductor Quantum Dots. *IEEE J. Sel. Top. Quantum Electron.* 2002, *8*, 1009-1014.

16. Empedocles, S. A. Quantum-Confined Stark Effect in Single Cdse Nanocrystallite Quantum Dots. *Science* **1997,** *278*, 2114-2117.

17. Beyler, A. P.; Marshall, L. F.; Cui, J.; Brokmann, X.; Bawendi, M. G. Direct Observation of Rapid Discrete Spectral Dynamics in Single Colloidal Cdse-Cds Core-Shell Quantum Dots. *Phys. Rev. Lett.* **2013,** *111*, 177401.

18. Efros, A. Luminescence Polarization of Cdse Microcrystals. *Physical Review B* 1992, *46*, 7448-7458.

19. Efros, A. L.; Rosen, M.; Kuno, M.; Nirmal, M.; Norris, D. J.; Bawendi, M. Band-Edge Exciton in Quantum Dots of Semiconductors with a Degenerate Valence Band: Dark and Bright Exciton States. *Physical Review B* **1996,** *54*, 4843-4856.

20. Norris, D. J.; Efros, A. L.; Rosen, M.; Bawendi, M. G. Size Dependence of Exciton Fine Structure in Cdse Quantum Dots. *Physical Review B* **1996,** *53*, 16347-16354.

21. Bawn, C. E. H.; Froehlich, H.; Hirsch, P. B.; Mott, N. F. *Theory of Defects in Solids*. Clarendon Press: Oxford, 1975.

22. Devreese, J. T. Fröhlich Polarons from 0d to 3d: Concepts and Recent Developments. *J. Phys.: Condens. Matter* **2007,** *19*, 255201.

23. Hsu, D.; Skinner, J. L. On the Thermal Broadening of Zero-Phonon Impurity Lines in Absorption and Fluorescence Spectra. *The Journal of Chemical Physics* 1984, *81*, 1604.

24. Nomura, S.; Kobayashi, T. Exciton–Lo-Phonon Couplings in Spherical Semiconductor Microcrystallites. *Physical Review B* **1992,** *45*, 1305-1316.

25. Cui, J.; Beyler, A. P.; Marshall, L. F.; Chen, O.; Harris, D. K.; Wanger, D. D.; Brokmann, X.; Bawendi, M. G. Direct Probe of Spectral Inhomogeneity Reveals Synthetic Tunability of Single-Nanocrystal Spectral Linewidths. *Nature Chem.* **2013,** *5*, 602-606.

Appendix A

The Determination of the Quantum Yield Using an Integrating Sphere

In integrating sphere was used to measure the quantum yield of the samples described in the previous chapters in this thesis. In this appendix, the basic operation of the integrating sphere set-up used as well as its practical limitations are described. The determination of the quantum yield of the near-infrared emitting dye IR-26 is used as an example. In general the same set-up was used for all quantum yield measurements, the only major modification being the use of a Si detector for samples emitting in the visible part of the spectrum and the choice of filter for each particular experiment.

The Determination of the Quantum Yield of IR-26

Quantum yield measurements were taken using an integrating sphere (Labsphere RTC-060-SF). The experimental set-up that was used is shown schematically in Figure 1 below. The sample was illuminated using a 785nm diode laser with an excitation power of 25mW that was chopped at 210 Hz. The output was collected using a calibrated germanium detector (Newport: 818-IR) through a Stanford Research Systems lock-in amplifying system. An 850 nm colored glass long-pass filter was used to block the excitation beam. The sample

(consisting of a solution of IR-26 dissolved in dichloroethene (DCE)) was placed in a PTFE capped quartz cuvette with five optical windows and a solvent blank was used to ensure as uniform of an environment inside the integrating sphere as possible. The integrating sphere included two baffles, one which lay immediately beneath the sample holder to prevent direct emission into the detector as well as a baffle on a side, which could be used to ensure that reflected light from the initial beam could only reach the detector after multiple reflection events.

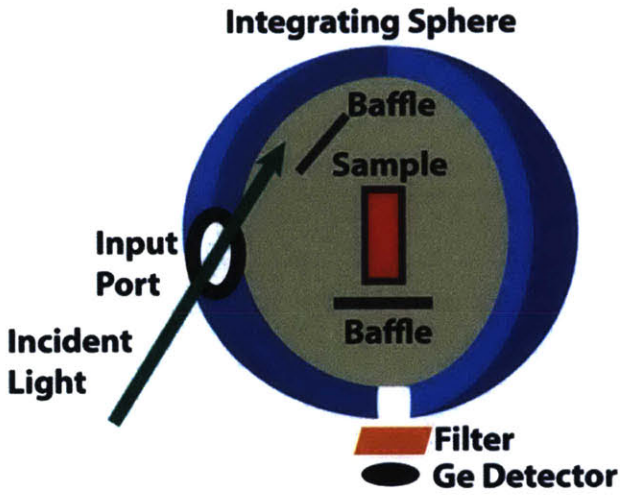

Figure A15: The configuration used to measure the quantum yield

Four measurements were than taken using this system: 1) Reference no filter (RNF), in which a reference cuvette containing neat DCE was placed in the sample compartment; 2) Reference filter (RF), in which an 850 longpass excitation filter was placed before the detector, 3) Sample filter (SF), in which the sample was switched to IR-26 dissolved in DCE with the filter in place and finally 4) Sample no filter SNF (sample no filter), in which the filter was removed. From these four measurements it was possible to extract the quantum yield of the solution by calculating the number of photons absorbed, the number

of photons emitted, and correcting for leakage of the excitation light and the dark counts of the detector using the following equation:

$$QY' = \frac{\frac{SF - LF}{EQE(S)}}{\frac{LNF - SNF - (SF - LF)}{EQE(L)}} \qquad (4\text{-}8)$$

In the equation above, RNF, RF, SNF, SF refer to the current measured on the detector four the four measurements and EQE(S) and EQE(L) refer to the EQE of the detector at the wavelength of the sample emission and of the excitation source respectively.

Finally, a correction was applied to account for the transmittance of the filter (at the wavelength of the emission band), which gave:

$$QY = \frac{QY'}{Filter\ Transmitance} \qquad (4\text{-}9)$$

Using this method, we measured the quantum yield of IR-26 at three different concentrations (quantified by the optical density of the sample). Each measurement was carried out in triplicate to ensure the reproducibility of the experiment. The quantum yields measured were respectively as shown in table 1 below:

Peak Optical Density	Quantum Yield (%)
0.90	0.042 ± 0.008
0.50	0.064 ± 0.002
0.35	0.054 ± 0.005
0.35 (24 hours later)	0.049 ± 0.003

The quantum yield we obtain for low optical densities is thus 0.05%, a value that is consistent with the values earlier reported by Beard and coworkers[1], and which is also close to the value of 0.07% more recently measured by Hatami and coworkers (before correcting for the absorption of the solvent)[2]. We therefore strongly believe that the new value of 0.05% is the true value rather than the value of 0.5%, which had earlier been used in the literature[3].

Appendix I References

1. Semonin, O. E.; Johnson, J. C.; Luther, J. M.; Midgett, A. G.; Nozik, A. J.; Beard, M. C. *J. Phys. Chem. Lett.* **2010,** 1, (16), 2445-2450.
2. Hatami, S.; Wuerth, C.; Kaiser, M.; Leubner, S.; Gabriel, S.; Bahrig, L.; Lesnyak, V.; Pauli, J.; Gaponik, N.; Eychmueller, A.; Resch-Genger, U. *Nanoscale* **2015,** 7, (1), 133-143.
3. Kopainsky, B.; Qiu, P.; Kaiser, W.; Sens, B.; Drexhage, K. H. *Appl. Phys.B* **1982**, 29, 15-18.